



Characterisation of photon sensors for the CBM-RICH and its use for the reconstruction of neutral mesons via conversion

Dissertation

zur Erlangung des akademischen Grades eines
Doktors der Naturwissenschaften (Dr. rer. nat.)

der Fakultät Mathematik und Naturwissenschaften
Fachgruppe Physik
der Bergischen Universität Wuppertal



vorgelegt von

Dipl. Phys. Sascha Reinecke

(geboren in Wuppertal)

August 2016

Von der Fachgruppe Physik der Bergischen Universität Wuppertal als Dissertation angenommen.
Tag der mündlichen Prüfung: 04. Oktober 2016

1. Gutachter:

Prof. Dr. Karl-Heinz Kampert
Bergische Universität Wuppertal

2. Gutachter

Prof. Dr. Claudia Höhne
Justus-Liebig-Universität Gießen



Contents

List of Figures	v
List of Tables	ix
1. Introduction	1
1.1. Thesis outline	3
2. The CBM Experiment	5
2.1. Physics motivation of CBM	5
2.2. Dileptons in Heavy-ion collisions	8
2.3. The CBM detector	10
2.3.1. The superconducting dipole magnet	11
2.3.2. The Micro Vertex Detector (MVD)	12
2.3.3. The Silicon Tracking Station (STS)	12
2.3.4. The Transition Radiation Detector (TRD)	12
2.3.5. The Time-of-Flight (TOF) detector	12
2.3.6. The Electromagnetic Calorimeter (ECAL)	13
2.3.7. The Projectile Spectator Detector (PSD)	13
2.4. The Ring Imaging Cherenkov detector (RICH) of CBM	13
3. Photon Sensors for the CBM-RICH	17
3.1. Requirements for photon sensors	17
3.2. Sensor-candidates for the CBM-RICH	21
3.3. Laboratory measurements on quantum efficiency of specific sensor samples	23

4. Overview of the 2012 prototype beamtest at CERN	25
4.1. The CBM-RICH prototype	25
4.1.1. General system components	27
4.1.2. Prototype photon camera system	28
4.1.3. The camera read-out system	31
4.2. Beamtest Overview	33
5. Analysis of the CBM beamtest 2012	37
5.1. Single-photon spectra	37
5.1.1. Single-photon spectra without corrections	38
5.1.2. Corrected single-photon spectra	43
5.1.3. Summary: Results from the single-photon spectra	45
5.2. Correction of the geometrical coverage	46
5.3. Correction of temperature and pressure	49
5.4. Crosstalk Estimation	54
5.4.1. Data based method for crosstalk estimation	56
5.5. Photon detection efficiency	64
5.6. Summary: Overall performance comparison	69
6. Pre-studies for conversion analysis of dileptons	73
6.1. The Conversion Method	74
6.2. The CbmRoot framework	75
6.3. Detector tomography	76
6.4. Upper estimate of the number of reconstructible π^0/η based on conversion	79
6.5. Combined study with MC-true and reconstructed data	83
6.5.1. Conversion in detector	88
6.6. Estimation of cuts for the full reconstruction	90
7. Results on conversion analysis of dileptons	99
7.1. Studies only based on completely reconstructed data	99
7.2. Background forming with the Event Mixing Technique	104
7.3. Limiting factors of the reconstruction efficiency	111
7.4. Reconstructing events with less than 4 electrons	114
7.4.1. Additional momentum-cut	117
7.5. Absolute efficiency of this method	118
7.6. Summary: reconstruction of π^0 via conversion	119
8. Summary and Outlook	121
A. Beamtime 2012 - Run Overview	125
B. Beamtime 2012 - Crosstalk Results	129
B.1. Exemplary distributions for Hamamatsu H8500	129
B.2. Exemplary distributions for Photonis XP85012	130
B.3. Exemplary distributions for Hamamatsu R11265	131

References	133
References for chapter 2	133
References for chapter 3	134
References for chapter 4	135
References for chapter 5	136
References for chapter 6	136
References for chapter 7	137
 Acknowledgement	 139
 Declaration of Authorship	 141



List of Figures

1.1.	Overview of all the existing GSI structures (on the left half, including the UNILAC and SIS18 accelerators in blue) and the new structure of FAIR (in red).	2
2.1.	Phase diagram of strongly interacting matter (from [4]).	6
2.2.	Multiplicity times branching ration for several rare probes and interaction rate of several experiments.	8
2.3.	Schematic view of the expected sources of dilepton production as function of the invariant mass in relativistic heavy-ion collisions (from [9]).	10
2.4.	Sketch of the latest design of the CBM detector for the SIS100 setup.	11
2.5.	Schematic layout of one camera module for the CBM-RICH camera.	14
2.6.	Latest RICH detector design solution (from [23]).	15
3.1.	Transmission curves of different photomultiplier window materials. (from [24]). . .	19
3.2.	Radiation environment for the RICH photon detector plane.	19
3.3.	Effects of a shielding box around the sensor camera of the CBM-RICH.	20
3.4.	Measured quantum efficiencies of several sensors.	24
4.1.	Technical drawings of the CBM-RICH prototype box.	26
4.2.	Installed mirror frame holder inside the CBM-RICH prototype with the light pulser system on top of the frame.	27
4.3.	CBM-RICH prototype camera during the beamtest 2012. The numbers indicate the position used in the analysis (compare Table 4.1).	29
4.4.	Circuit diagram of attenuator board used for attenuating the signals from the sensors.	32
4.5.	Complete setup during the beamtest 2012.	33
4.6.	Indicated Cherenkov ring positions on the camera during the beamtest 2012.	34
5.1.	Single-photon sum spectra of all 23 sensors used during the beamtest.	39

5.2. Resulting fit distributions of the single-photon spectra of three single pixel for each sensor.	41
5.3. Calculated gain values of all pixel for all sensors (in factors of 10^6).	42
5.4. Normalized and corrected single-photon sum-spectra of all 23 tested sensors and spectra with additional cut.	44
5.5. Distributions of ring centers from the circle fit. Basis is the beamtest data (threshold scan 2), runs #176 - #181. Shown are ring positions A, B, D, E, G, and I.	48
5.6. Resulting coverage distributions of the different arrangements (left: H8500, mid: R11265, right: XP85012). Each distributions has been fitted with a Gaussian.	48
5.7. Crosscheck of the simulations with all points lying on a sensor.	49
5.8. Geometrical coverage as function of the simulated ring center (left: H8500, mid: R11265, right: XP85012). The different behaviour of the arrangements can clearly be recognized.	50
5.9. Mean ring radius fir position A for 33 different runs.	51
5.10. Mean electron ring hit multiplicities for Position A for 33 different runs.	53
5.11. Exemplary distance distribution.	55
5.12. Simulation of the behaviour of the old method of crosstalk calculation for different absolute illumination values and fixed input crosstalk values.	57
5.13. Distributions of χ^2 for the distance distribution and for the illumination distribution.	59
5.14. Calculated crosstalk amount of all used sensors during the beamtest 2012 gained from run #207.	61
5.15. Different crosstalk results for the tested sensors.	62
5.16. Projected χ^2 -values of the χ^2 -sum distribution for uncertainty estimation of the method.	63
5.17. Results for the number of detected hits per electron Cherenkov ring from the high-voltage scan.	66
5.18. Results for the number of detected hits per electron Cherenkov ring from the threshold scan.	68
5.19. Behaviour of the data for the Photonis XP85012 MCPs in terms of number of hits per ring for different applied ADC cuts.	68
6.1. Detector tomography of the CBM detector for the SIS100 setup.	77
6.2. Detector tomography of the CBM detector for the SIS100 setup, in the region of the RICH detector.	78
6.3. Amount of photon conversion depending on the z-axis.	79
6.4. Number of generated π^0 , η and direct photons per event for 5 million events.	80
6.5. Number of π^0 in the MC-true trackbank divided by their production within the primary vertex and within secondary vertices.	81
6.6. Invariant mass of the 4 leptons originating from the same π^0 , identified and momenta via MC-true data.	82
6.7. Number of detected rings in the RICH detector.	83
6.8. Invariant mass of four electrons/positron from the same π^0 , identified with MC-true data.	84
6.9. Invariant mass of four electrons/positron from the same π^0 , identified with MC-true data.	85

6.10. Phase space coverage of simulated and reconstructed π^0	86
6.11. Efficiency studies for the cuts derived in Section 6.6 for three different methods of electron identification.	87
6.12. Number of π^0 from which 0, 1, 2, 3, and all 4 electrons are identified based on the ANN and a cut-value of -0.8	88
6.13. Invariant mass of 4 leptons from the same π^0 calculated with MC-true and reconstructed momenta.	89
6.14. Origins of leptons along the z-axis used for reconstruction of π^0 with the combined method.	90
6.15. Output from the ANN for electrons and all other particles.	91
6.16. Influence of the ANN-cut value for electron identification on the number of reconstructed π^0	92
6.17. Distribution of χ^2 -values of the momentum fit in dependence of the transversal momentum p_t	93
6.18. Number of true and false combinations of e^+ and e^- to a photon (identified via MC-true).	94
6.19. Opening angle distributions of electron-positron pairs.	95
6.20. Distribution of opening angle ϑ in dependence of the transversal momentum p_t	96
6.21. Number of true and false combinations of e^+ and e^- to a photon (identified via MC-true).	97
6.22. Invariant mass distributions of electron-positron pairs.	97
7.1. Reconstructed invariant mass spectra for four different cases of applied cuts.	101
7.2. Invariant mass spectrum for the combination of four leptons using only reconstructed data.	102
7.3. Invariant mass spectrum for the combination of four leptons using only reconstructed data with additional MC-true cuts for separation.	103
7.4. Reconstructed invariant mass spectrum from the combination of 4 e^\pm and the scaled background from EMT, and subtraction of both.	105
7.5. Projection of all entries from the background-subtracted invariant mass spectrum.	107
7.6. Background from EMT and background-subtracted invariant mass spectrum with a Gaussian fit of the π^0 peak.	108
7.7. Invariant mass spectra for different p_t -ranges.	109
7.8. Background-subtracted invariant mass spectra for different p_t -ranges.	110
7.9. Background-subtracted spectrum for $0.5 \text{ GeV}/c < p_t < 1.0 \text{ GeV}/c$ and $1.0 \text{ GeV}/c < p_t < 1.5 \text{ GeV}/c$	110
7.10. Distributions of the momentum p versus the transversal momentum p_t of electrons.	111
7.11. Estimation of number of reconstructible π^0 for a testsample of $5 \cdot 10^5$ events with a reduced magnetic field of 30 % nominal value.	112
7.12. Phase-space coverage for a magnetic field of 30 % of the nominal value and 70 %.	113
7.13. Invariant mass spectra for π^0 reconstructed with the combined method and with a reduced magnetic field of 30 % nominal value.	113
7.14. Reconstructed invariant mass spectrum divided by the EMT background.	114

7.15. Reconstructed invariant mass spectrum and scaled background from EMT for the case of 3 leptons being detected in the RICH detector, plus the background-subtracted spectrum.	115
7.16. Invariant mass spectrum for the combination of three identified leptons and one unidentified lepton using only reconstructed data.	116
7.17. Distribution of emission angles θ of a electron versus its momentum p	117
7.18. Reconstructed invariant mass spectrum and scaled background from EMT for the case of 3 electrons being detected in the RICH detector and an additional momentum-cut on the forth (unidentified) electron, plus the background-subtracted spectrum.	118
7.19. Coverage of the phase-space in terms of transversal momentum p_t and rapidity y	119
B.1. PMT #1: χ^2 -distributions for the distance distribution (left) and for the illumination distribution (right). Resulting minima are indicated with black lines.	129
B.2. PMT #1: distribution from data (blue) and best fitting simulation (red) for the illumination distribution (left) and for the distance distribution (right).	130
B.3. PMT #13: χ^2 -distributions for the distance distribution (left) and for the illumination distribution (right). Resulting minima are indicated with black lines.	130
B.4. PMT #13: distribution from data (blue) and best fitting simulation (red) for the illumination distribution (left) and for the distance distribution (right).	130
B.5. PMT #17: χ^2 -distributions for the distance distribution (left) and for the illumination distribution (right). Resulting minima are indicated with black lines.	131
B.6. PMT #17: distribution from data (blue) and best fitting simulation (red) for the illumination distribution (left) and for the distance distribution (right).	131



List of Tables

3.1. Important properties of tested MAPMTs and MCPs.	23
4.1. Positions and serial numbers of the PMTs used during the beamtime. In addition the gain as given by the manufacturer is included.	30
4.2. Capacitances of the attenuator boards in dependence of the PMT.	32
4.3. Overview of the LED runs taken. Shown are the run number, the used LED and the high-voltage setting (explained in the next chapter).	35
5.1. Used high-voltages of the PMTs and MCPs during the beamtest.	40
5.2. Charge calibration of the used read-out electronics. The resulting conversion factors can be used to calculate the gain of each sensor from the single-photon peak position.	43
5.3. Ring centers and widths used for the simulations of the geometrical coverages.	47
5.4. Results from the fits of Figure 5.6 given as mean geometrical coverage and width of the distribution. Due to the high statistics errors of the fit are very small and not relevant here.	49
5.5. Results of the crosstalk estimation for all measured sensors. The corresponding value of the illumination distribution is also given. All results are based on the LED-run #207. The given errors remark just an uncertainty region and no real error of the calculated value.	60
5.6. Used correction values for the HV-scan for the calculation of the number of mean hits per electron Cherenkov ring. Different values for temperature and pressure are a result of a different time the runs were taken.	67
6.1. Geometry versions of the sub-detectors used for the simulation of $5 \cdot 10^6$ UrQMD events. This setup resembles the SIS100 electron setup from summer 2015.	76
6.2. Overview of all cuts applied to each single lepton (χ^2) and to e^+e^- -pairs (opening angle and invariant mass).	96

7.1. Scaling factors for the background calculated with EMT to the reconstructed invariant mass spectrum.	108
A.1. Positions and serial numbers of the PMTs used during the beamtime.	125
A.2. Positions and serial numbers of the PMTs used during the beamtime.	126
A.3. Overview of the LED runs, i.e. beam was switched off. Given are the different used LEDs and the high-voltage setting of the sensors (compare Table 5.1).	128

Introduction

The existing GSI Helmholtzzentrum für Schwerionenforschung in Darmstadt/Germany is currently being extended by the Facility for Antiproton and Ion Research (FAIR). This future research centre consists of four different scientific pillars covering a wide physical programme¹:

CBM The Compressed Baryonic Matter (CBM) experiment will study the behaviour of strongly interacting matter under highest densities in heavy-ion collisions. Some details about the physics and the detector itself are presented in the next chapters.

PANDA The Proton Anti-Proton Annihilation at Darmstadt (PANDA) experiment will investigate the properties of hadrons in proton-antiproton collisions. To achieve this, a dedicated High Energy Storage Ring (HESR) will be build to store antiprotons produced by a primary proton beam, and to collide them with a fixed target in the detector.

APPA Atomic, Plasma Physics and Applications (APPA) covers several experiments. The fields of study include for example plasma physics at high pressures and low temperatures (as e.g. in the interior of large planets), or the impact of cosmic radiation on inter-planetary flights for astronauts as also for spacecraft components.

NUSTAR The field of Nuclear Structure, Astrophysics and Reactions (NUSTAR) also includes several dedicated experiments. Some of the research fields of these experiments are studying exotic nuclei (e.g. effects of different neutron-to-proton ratios in nuclei), understanding nucleosynthesis in astrophysical objects and in the early universe, the creation of new super-heavy elements, or the medical applicability of the gained knowledge and possibilities.

A schematic overview of the existing GSI facility and the planned FAIR facility can be seen in Figure 1.1.

The history of experimental heavy-ion physics dates back only a few decades, starting in the 1970's and early 80's at the Lawrence Berkeley National Laboratory (LBNL) in Berkeley, USA,

¹ Online links to all experiments can be found here: <http://www.fair-center.eu/for-users/experiments.html>

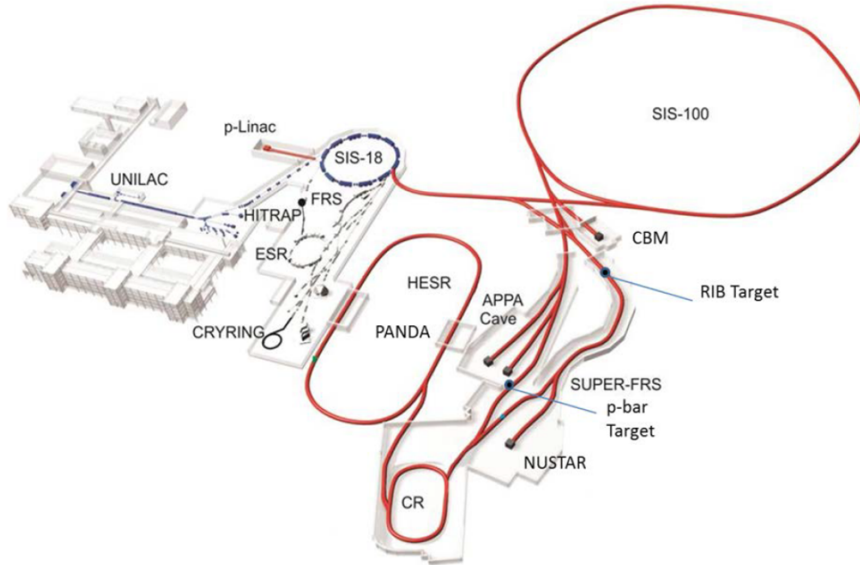


Figure 1.1. – Overview of all the existing GSI structures (on the left half, including the UNILAC and SIS18 accelerators in blue) and the new structure of FAIR (in red).

with the Bevatron (proton accelerator, 6.2 GeV, which was later extended with the HILAC, a linear accelerator for heavy ions to form the Bevalac), and at the Joint Institute for Nuclear Research (JINR) in Dubna, Russia, with the Nuclotron. Later the SIS18 accelerator at GSI Helmholtzzentrum für Schwerionenforschung (GSI) in Darmstadt, Germany, the SPS accelerator at the European Organization for Nuclear Research (CERN) in Geneva, Swiss, and the newly developed AGS also at LBNL allowed for the investigation of nuclear matter at higher energies. With the Large Hadron Collider (LHC) being built at CERN and the Relativistic Heavy Ion Collider (RHIC) at Brookhaven National Laboratory (BNL), Brookhaven, USA, the highest energies (LHC: protons $\sqrt{s_{NN}} = 14$ TeV, lead ions 2.76 TeV per nucleon; RHIC: for protons 200 GeV, for gold ions 200 GeV per nucleon) can be reached, allowing to generate matter under extreme conditions in terms of temperature and density, similar to the early universe.

As could be seen from theoretical considerations, the highest energies of LHC and RHIC do not allow to create a fireball with highest densities during the collision, as the nuclei become transparent, resulting only in a partially energy deposit of the colliding nucleons before leaving the interaction zone ([1]). Highest densities of the fireball can only be reached at lower energies, where the incoming baryons are partially stopped in the interaction zone, thus creating the fireball. CBM is aimed at exploring exactly this energy region, being able to study collisions at highest densities.

Suitable probes to investigate the properties of the created medium are for example dileptons, J/Ψ , or hyperons. A short overview of the most interesting probes is given in the next chapter.

The work presented in this thesis aims at an optimisation of the CBM Ring Imaging Cherenkov Detector (RICH) camera by selecting the best performing sensor type, and also on feasibility studies regarding the possibility of reconstructing π^0 via its decay into $\gamma\gamma$ and a further conversion of both γ , with a detection of the conversion electrons in the CBM-RICH detector.

1.1 Thesis outline

This thesis includes several chapters, starting with an introductory part followed by the gained results discussed in detail.

Chapter 2 gives a short overview of the CBM experiment, including an overall physics motivation of CBM, with a more detailed explanation of dileptons in heavy-ion collisions, and a presentation of the whole CBM detector. As the RICH detector is the sub-detector of CBM, which is most relevant for this thesis and all presented data analyses and simulations, this one will be depicted in more detail.

Chapter 3 presents an introduction into the field of photon sensors, which is one important element of the CBM-RICH detector. The individual requirements for photon sensors in the CBM-RICH detector are discussed (e.g. photon detection efficiency or radiation hardness), and the candidates, which are considered for usage, are presented, together with laboratory measurements on the quantum efficiency of these candidates.

Chapter 4 consists of a detailed description of the CBM-RICH prototype and of the beamtest conducted 2012 at CERN, where the prototype has been tested under realistic conditions, with focus on the photon camera and the data being taken.

Chapter 5 includes the analyses and results from the beamtest data. The focus is put on the number of detected photons per electron Cherenkov ring for several different configurations, with crosstalk influencing the data and thus needs to be corrected for. In addition, the single-photon spectra of the tested sensors are investigated

Chapter 6 serves as an introductory chapter to the field of dilepton simulations and reconstruction of π^0 with the conversion method. Pre-studies are presented using MC-true data for the identification of electrons and positrons stemming from photon conversion, e.g. to generate tomography plots of the CBM detector or to extract some upper estimates of the reconstruction probability. One important aspect in this chapter is the estimation of cuts for the reconstruction as presented in the following chapter.

Chapter 7 discusses all results of the conversion analysis, when only relying on completely reconstructed data, i.e. neglecting any MC-true information for identification and reconstruction of π^0 , using the cuts derived in the previous chapter. These conditions represent the same conditions, which will prevail in the experiment later. Background estimation and subtraction, using the Event Mixing Technique, and the deduced results are presented in detail.

Chapter 8 finally comprises a summary of this thesis and an outlook on future developments, regarding a successor of the tested Hamamatsu H8500 multi-anode photomultiplier (MAPMT), and also possible improvements of the reconstruction of π^0 .

The CBM Experiment

The Compressed Baryonic Experiment (CBM) will be one of the first experiments to be assembled at the FAIR facility in Darmstadt. As a fixed-target experiment it will directly use the primary beam from the SIS100/SIS300 accelerators.

This chapter covers a short motivation for CBM, describing a few different physics aspects of the CBM programme in Section 2.1 and some more details on the topic of dileptons in heavy-ion collisions in Section 2.2. Section 2.3 includes a short description of the CBM detector and its sub-detectors, with more detailed descriptions of the RICH detector in Section 2.4.

An ideal source to get all details of the physical motivation of CBM is the CBM Physics Book ([2]). To get just a rough overview a recently released paper is well suited ([3]).

2.1 Physics motivation of CBM

CBM will study the phase diagram of strongly interacting matter in a region of high net-baryon densities and moderate temperatures. It is complementary to experiments at RHIC and LHC, which aim to investigate the phase diagram at very high temperatures and nearly vanishing net-baryon densities. This phase diagram, in dependence of the temperature T and the (net-)baryon density (ρ_B , or as conjugate variable the baryo-chemical potential μ_B), can be seen in Figure 2.1 with indicated regions, which can be investigated with LHC and RHIC. The regions, which will be investigated with the SIS100/300 accelerators, exhibit larger densities but lower temperatures.

The regions studied by LHC and RHIC resemble conditions during the early phase of the universe, i.e. at nearly vanishing density but extremely high temperatures. Properties of the other regions remain largely unknown experimentally. At low temperature and pressure quarks exist in a confined state, as they are bound into hadrons. By increasing the temperature (and keeping a low density) a cross-over type phase transition from the hadronic matter to the quark-gluon

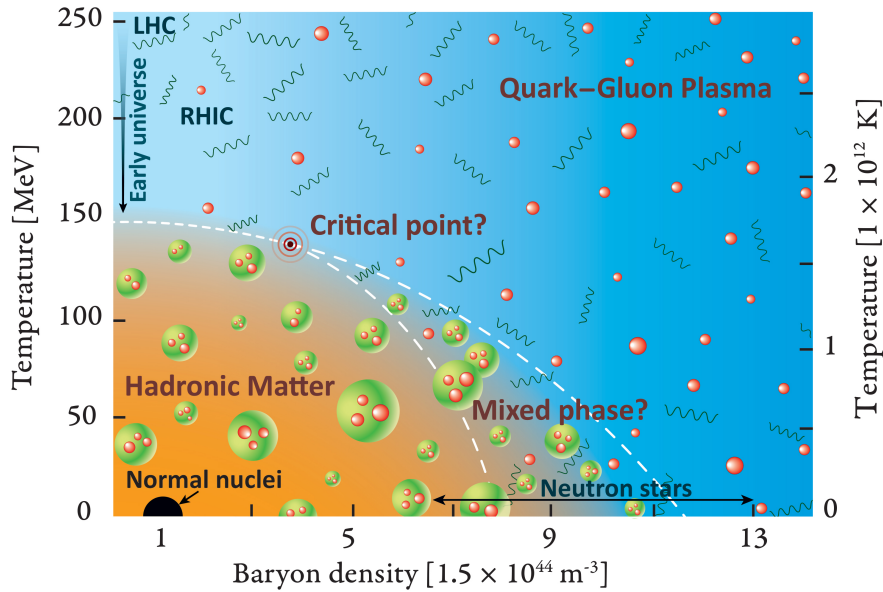


Figure 2.1. – Phase diagram of strongly interacting matter (from [4]).

plasma can be reached at the critical temperature $T_C \approx 160 \text{ MeV}$. This phase transition type is characterised by the indistinguishability of both phases. According to predictions, this transition is of first order at higher densities, thus also a critical point must exist as a separation of both transition types. During the phase transition to a quark-gluon plasma, several phenomena are expected to happen, e.g. deconfinement, i.e. hadrons are melting and thus quarks and gluons can exist freely, or the restoration of chiral symmetry, which is spontaneously broken in the ground state. In addition there are several other phases predicted, when going to higher densities, like a quarkyonic phase or a colour superconducting phase.

From the already gained knowledge in this field of physics and from theoretical considerations several fundamental questions are raised and will be addressed with the CBM experiment (from [3]):

- What is the equation of state of QCD matter at high net-baryon densities, and what are the relevant degrees of freedom at these densities? Is there a phase transition from hadronic to quark-gluon matter, or a region of phase coexistence? Do exotic QCD phases like quarkyonic matter exist?
- To what extent are the properties of hadrons modified in dense baryonic matter? Are we able to find indications of chiral symmetry restoration?
- How far can we extend the chart of nuclei towards the third (strange) dimension by producing single and double strange hypernuclei? Does strange matter exist in the form of heavy multi-strange objects?

To be able to study all these aspects in detail, a lot of different observables will be investigated. The most promising of these are:

Collective Flow: The term ‘collective flow’ refers to the directional distribution of particles and their distribution of energies and momenta. It is mathematically described by the Fourier expansion of the azimuthal distribution of final state hadrons, and proportional

to $(1 + v_1 \cos \phi + v_2 \cos 2\phi + \dots)$, with ϕ the azimuthal angle relative to the reaction plane, and v_1 and v_2 the Fourier coefficients, whereas v_1 is interpreted as directed (in-plane) flow and v_2 as elliptic flow. The flow can be used to gather information on the equation of state, and is also interpreted as a signature for a phase transition to the quark-gluon plasma ([5]).

Low-mass vector mesons: In-medium information of the fireball can be extracted via leptonic decays of vector mesons, as those leptons do not further interact with the surrounding medium and thus carry information of the meson within the medium. Modifications of the hadronic properties (e.g. mass, width or more generally the hadron spectral function) are expected to be indicators of chiral symmetry restoration in the QGP. Interesting candidates here are the ρ , ω , and ϕ mesons, but also the mass region up to the J/Ψ is of particular interest, as no hadronic sources contribute directly to this mass region of the spectrum ([3]).

Charm production: Due to the large mass of charm quarks, production of hadrons containing charm quarks is only possible in hard collisions during the very early stage of the collision. After their creation they can then propagate through the dense medium. Depending on the type of the medium (partonic or hadronic) different consequences are expected. In the case of a partonic medium the formation rate of charmonium (bound $c\bar{c}$ pairs) is reduced due to Debye screening (i.e. produced gluons will screen c and \bar{c} quarks). Thus charm quarks are able to coalesce with light quarks to hadrons with open charm. The ratio of open charm ($D^{\pm/0}$) to hidden charm (J/Ψ)/charmonium is thus considered as an decisive observable for the formation of a quark-gluon plasma.

Multi-strange hyperons: Hyperons are baryons, which contain at least one strange quark, thus multi-strange hyperons contain more than one strange quark, e.g. Ξ or Ω . The production of Ω is expected to be strongly tied to the transition from a partonic phase to a hadronic final state, because the equilibration of Σ (which seems to be a requirement for their production) is not yet fully understood in terms of hadronic two-body relaxation processes in the limited life time of the fireball.

Event-by-event fluctuations: Event-by-event fluctuations of observed quantities (e.g. baryon number, strangeness, or electrical charge, particle yields, ratios, or kinematical properties) are an indicator of a critical behaviour of the fireball or a first order phase transition. Usually fixed target experiments are in disadvantage of adequately measuring these fluctuations in comparison to collider experiments, due to the limited azimuthal acceptance. But the geometry of the CBM detector was adapted to these requirements such, that a nearly full azimuthal coverage is given.

Dileptons: Dileptons are emitted from the fireball during all stages of the collision and do not further interact with the hadronic medium, thus allowing for a good insight in the properties of the collision. A more detailed discussion on dileptons in heavy-ion collisions is presented in Section 2.2, as this is the theoretical motivation for the reconstruction of π^0 with the conversion method, presented in Chapter 6.

Most of the particles, resonances, etc., which will be investigated in CBM are produced at a very low production rate, thus requiring a very high amount of event statistics, which can not be provided by existing heavy-ion experiments. CBM will feature a collision rate of 1 MHz (and up to 10 MHz for some dedicated runs), allowing for the study of these rare probes (compare Figure 2.2 (right) for the interaction rates of several experiments). Figure 2.2 (left) depicts the

multiplicities times the branching ratios of several probes, with the black horizontal line marking already measured probes (above), and not yet measured probes (below). With the high collision rate in CBM it is expected, that also the probes below the black line can be measured.

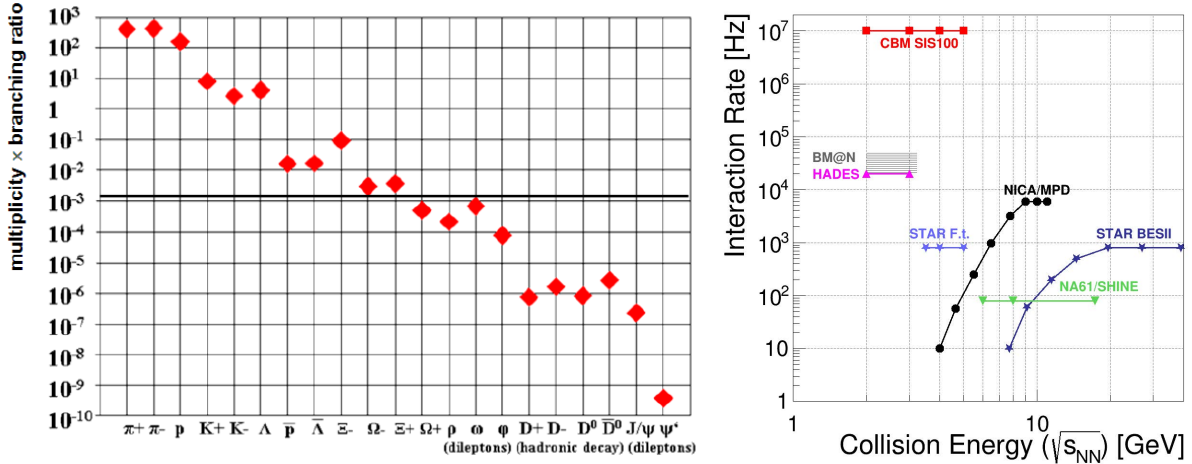


Figure 2.2. – Multiplicity times branching ratio for several rare probes (left, from [6]). The black horizontal line indicates those already measured (above) and those not yet measured (below). The right picture shows the interaction rate for several heavy-ion experiments (from [3]).

2.2 Dileptons in Heavy-ion collisions

As the topic of dileptons within heavy-ion collision is very extensive, only a short overview will be given here. More detailed descriptions and informations can for example be found in the CBM Physics Book ([2]) or in [7], and in references herein.

The primary goal of CBM is the investigation of the QCD phase diagram at high net-baryon densities and moderate temperatures and the characterisation of the phase transition of hadronic matter to the quark-gluon plasma. Ideal probes to study the created fireball in the collision are those featuring small interaction cross sections and thus long mean-free paths in matter. Thus, photons and leptons, which only interact electromagnetically and not strongly, are an ideal probe of the medium. In contrast hadrons, which interact strongly with the surrounding medium in the order of several to tens of millibarns ([8]), are not sufficiently fulfilling this requirement and contain only information about the conditions after freeze-out.

In the quark-gluon plasma a quark and an antiquark can interact to form a virtual photon γ^* . The γ^* itself can then decay into a lepton l^- and an antilepton l^+ (i.e. $q + \bar{q} \rightarrow l^- + l^+$), which can then be detected. The system of the created lepton and antilepton is called a dilepton. Other sources of dilepton production include interactions of hadrons with its antiparticles (e.g. $\pi^+ + \pi^- \rightarrow l^+ + l^-$), decays of hadronic resonances like ρ , ω , ϕ , and J/ψ , Drell-Yan processes, and also photon conversion within the target and within the detector material. Dalitz-decays of π^0 and η make up a large fraction of this and are the motivation for the second part of this thesis.

The important measurement variables of dileptons are the invariant mass m_{inv} equal to the

4-momentum squared

$$m_{\text{inv}}^2 c^2 = \mathbf{p}_{e^+e^-}^2 = (\mathbf{p}_{e^+} + \mathbf{p}_{e^-})^2 \quad (2.1)$$

and the transversal momentum p_t , which are used to investigate the different phases of the collision. Dileptons with a large invariant mass and high p_t are created when the temperature of the system is very high, i.e. in the early stages of the collision. At lower temperatures dileptons with smaller invariant masses and lower p_t are emitted. The reason is that the production rate and the momentum distribution of the dileptons depend on the momentum distribution of the quarks and antiquarks in the plasma, which are determined by the thermodynamic condition of the plasma. Therefore, dileptons give access to the thermodynamic state of the medium at the moment of their production.

Overall, there are two main sources for dileptons: They can be created from the decay of hadrons, thus giving access to the in-medium properties of those hadrons. And they can be created from the annihilation of a quark-antiquark pair, allowing to gather information about the temperature of the created system.

Dileptons are divided into three different mass regions based on their invariant mass ([9]):

1. Low-mass region (LMR): $m_{\text{inv}} < m_\phi \approx 1.024 \text{ GeV}/c^2$. The low-mass region is dominated by the decay of light vector mesons. With the low-mass continuum it is possible to probe the in-medium ρ spectral function. In addition, information of the fireball lifetime can be gathered from the excess yield of lepton pairs in this energy range, as well as information of chiral symmetry restoration ([10]).
2. Intermediate-mass region (IMR): $m_\phi < m_{\text{inv}} < m_{J/\psi} \approx 3.1 \text{ GeV}/c^2$. In the intermediate-mass region, continuum radiation from QGP dominates the dilepton mass spectrum and thus this region is important for getting a pure QGP signature. The slope of the spectrum within this region directly reflects the average temperature of the fireball ([11]).
3. High-mass region (HMR): $m_{J/\psi} < m_{\text{inv}}$. In the high-mass region, the most interesting phenomenon is the primordial emission of heavy quarkonia like J/ψ and Υ suppression. Apart from the resonances the crosssection is dominated by the Drell-Yan process for $q\bar{q}$ annihilation.

A schematic view of the dilepton invariant mass spectrum is shown in Figure 2.3.

In the past, the low-mass region of the invariant mass spectrum was of certain interest, as a discrepancy between the measured data of the DLS experiment and the expected contributions could be seen, prevailing between $0.2 \text{ GeV}/c^2$ and $0.6 \text{ GeV}/c^2$ (called the 'DLS puzzle'). This discrepancy was confirmed by the HADES experiment, and explanations were derived from $p + p$ and $d + p$ collisions ([12]).

During the last years, there is a special interest to the ρ , ω and ϕ meson spectra. It was realized, that the leptons, which contribute to these spectra, contain important information about the global characteristics of the hot/dense medium and the critical phenomena in this medium, such as restoration of chiral symmetry. This information can, in principle, be unfolded by studying experimentally the shift of vector meson masses and their broadening in hadron-ion and ion-ion collisions. Furthermore, vector meson spectra could tell us about the very existence and space-time evolution of mixed and hadronic phases of the reaction. ([13])

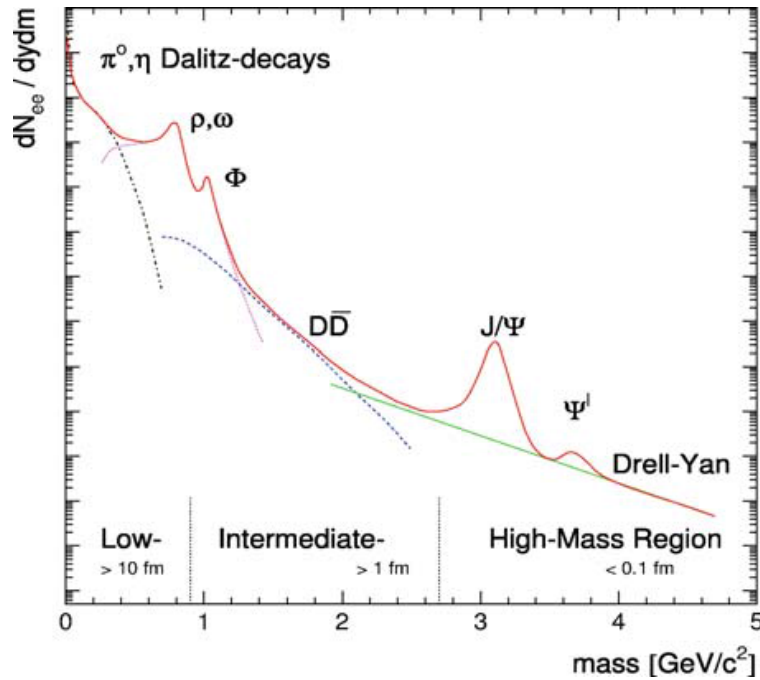


Figure 2.3. – Schematic view of the expected sources of dilepton production as function of the invariant mass in relativistic heavy-ion collisions (from [9]).

The idea to use leptons to gather information of the hadronic matter already came up in the late 70s and 80s ([14, 15, 16]), and its rich physics potential has been clearly demonstrated over the past decade of heavy-ion experiments, especially at the GSI-SIS18 and CERN-SPS accelerators.

2.3 The CBM detector

A schematic drawing of the complete CBM detector setup for the SIS100 electron-hadron setup together with the High Acceptance Dielectron Spectrometer (HADES, [17]) detector, which will be placed in the same cave as CBM but will not be discussed here, is shown in Figure 2.4.

The CBM detector consists of several sub-detectors which will measure various parameters of all particles being produced in the beam-target interaction during a collision. The first detectors downstream of the target are the Micro Vertex Detector (MVD) and the Silicon Tracking Station (STS). Both are placed inside a superconducting dipole magnet and allow for high-resolution tracking and momentum reconstruction for all charged particles. The Ring Imaging Cherenkov detector (RICH) and the Transition Radiation Detector (TRD) are placed further downstream the magnet. Both the RICH and the TRD aim at electron identification and pion separation. The most downstream detectors in the CBM setup are the time-of-flight (TOF) wall and the Projectile Spectator Detector (PSD). The TOF wall serves for the identification of hadrons, whereas the PSD serves for an event plane characterization and determination of the collision centrality. Two additional detectors are shown in their parking position: the Electromagnetic Calorimeter (ECAL) and the Muon Detection System (MuCh). The ECAL will measure direct photons in selected regions of the phase space. The CBM detector will be operated in two different configurations:

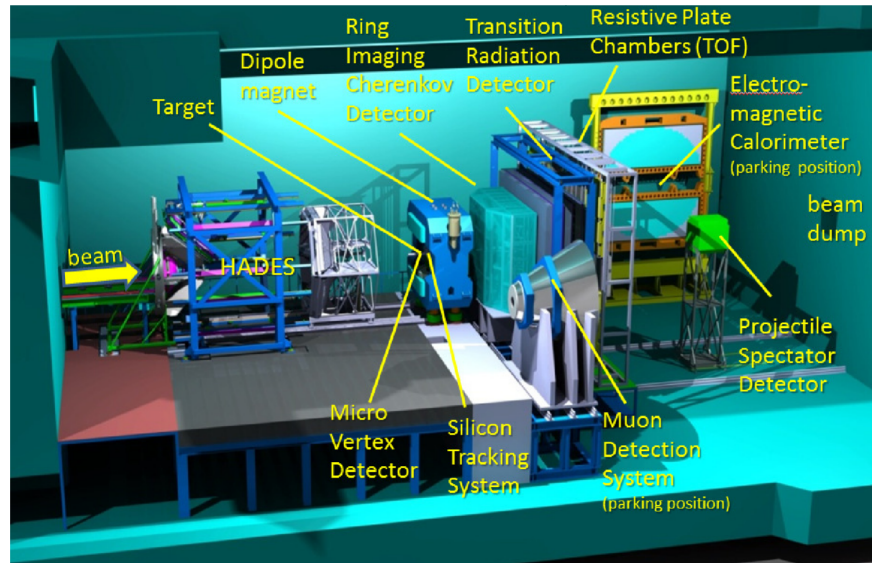


Figure 2.4. – Sketch of the latest design of the CBM detector for the SIS100 setup. All relevant sub-detectors are marked. As it is planned, the HADES detector will be placed in front of the CBM detector. (from [6]).

in the muon setup muon pairs will be measured using the MuCh detector; in the electron setup the RICH will be used to measure dielectrons. Both setups will be interchanged on a roughly yearly basis, and allow therefore for the investigation of the muonic and electron components of dileptons.

The design options for the CBM detector include also studies for the SIS300 accelerator, which is planned to be build a few years after the SIS100. A few differences of the setup for the SIS300 are several more TRD stations and a larger TOF wall as also a larger size of the ECAL. The design of the MVD/STS and the RICH detector for the SIS100 setup are able to cope with the circumstances within the SIS300 setup and therefore don't need any modifications.

The complete CBM detector covers a polar angle acceptance of $2.5^\circ - 25^\circ$ and full azimuthal acceptance.

For nearly all sub-detectors there already exists an approved Technical Design Report (TDR)¹, which include detailed descriptions and studies. Below, a short summary of the important properties of the different sub-detectors, from the most upstream one to the most downstream one, is given.

2.3.1. The superconducting dipole magnet

The superconducting dipole magnet bends all charged particles created in the collision. The curvature radius of the bending is then used to reconstruct the exact particle momenta with high precision. The maximum nominal field value of the magnet is 1 Tm. Field clamps at the downstream side of the magnet limit the stray field into the RICH detector system, which is of importance for the photomultipliers used for the RICH photon detector/camera.

¹ Weblinks to all TDRs can be found here:

<http://www.fair-center.eu/for-users/experiments/cbm/cbm-documents.html>.

2.3.2. The Micro Vertex Detector (MVD)

The MVD is the first detector behind the collision vertex and placed just a few cm downstream the target. It is used for the reconstruction and identification of very short-lived particles like D-mesons (which have an average lifetime of around $c\tau(D^0) \approx 123 \mu\text{m}$ and $c\tau(D^\pm) \approx 314 \mu\text{m}$) via the reconstruction of secondary vertices. For an adequate measurement and reconstruction of those an excellent spatial resolution is needed. In addition, multiple scattering has to be kept at a low level, therefore requiring a very low material budget of the MVD.

The technology, which can cope with these needs and also with the harsh radiation environment, are silicon detectors based on ultra-thin Monolithic Active Pixel Sensors (MAPS).

The current design of the MVD foresees four stations at $z = 5 \text{ cm}, 10 \text{ cm}, 15 \text{ cm},$ and 20 cm with an increasing size. The intended pixel size will be $20 \mu\text{m} \times 20 \mu\text{m}$ resulting in a position resolution of $4 \mu\text{m}$ and allowing to determine the secondary decay vertex of a D-meson with a resolution of $50 \mu\text{m} - 100 \mu\text{m}$ along the beam axis. The total radiation length of the complete detector could be reduced to $300 \mu\text{m} - 500 \mu\text{m}$ silicon equivalent ($< 0.5\%$ radiation length), including all sensors and also support structures. The radiation tolerance of this technology is at present $10^{13} \text{ n}_{\text{eq}}/\text{cm}^2$ (non-ionizing), and 3 Mrad (ionizing).

2.3.3. The Silicon Tracking Station (STS)

The STS is probably the most important detector in CBM. It aims at track reconstruction and momentum determination and also for the identification of decay topologies within its aperture. The current design consists of eight stations placed between $z = 30 \text{ cm}$ and $z = 100 \text{ cm}$ (i.e. completely within the magnet) in distances of 10 cm comprising double-sided silicon micro-strip detectors. Simulations show that a momentum resolution of $\Delta p/p \approx 1\%$ over a large momentum range of $0.1 \text{ GeV}/c - 12 \text{ GeV}/c$ together with a high track reconstruction efficiency of about 95% can be reached. To reduce the material budget within acceptance the front-end electronics will be placed outside the active area of the STS and the sensors will be interconnected to the read-out chip via low-mass cables.

2.3.4. The Transition Radiation Detector (TRD)

The TRD is build for particle tracking with a position resolution of $300 \mu\text{m} - 500 \mu\text{m}$ across and $3 \text{ mm} - 30 \text{ mm}$ along the pad, and also for electron identification for momenta $p \geq 1 \text{ GeV}/c$. It consists of several layers within one (three for SIS300) dedicated stations placed downstream of the RICH detector. The TRD alone aims at a pion suppression in the order of 10 for SIS100 (and a factor of 100 for SIS300) at 90% electron efficiency.

2.3.5. The Time-of-Flight (TOF) detector

The TOF, with an active area of around 120 m^2 , aims at the identification of hadrons. It is based on multi-gap resistive plate chambers (MRPC) with low-resistivity glass and will achieve a time resolution of 60 ps .

2.3.6. The Electromagnetic Calorimeter (ECAL)

The ECAL aims for the detection of photons, which then are used for the reconstruction of neutral mesons (like π^0 or η) decaying into photons. This is a complementary approach to the detection of the conversion-leptons of the photons, which will be studied in Chapter 6. The ECAL is a ‘shashlik’-type detector consisting of 140 layers made from 1 mm lead and 1 mm scintillator stacks, in cell sizes of 3 cm \times 3 cm, 6 cm \times 6 cm, and 12 cm \times 12 cm.

2.3.7. The Projectile Spectator Detector (PSD)

The PSD is the most downstream sub-detector of CBM and will provide an experimental measurement of a heavy-ion collision centrality and orientation of its symmetry plane based on an event-by-event estimate. It is a compensating (i.e. similar response to electromagnetic and hadronic particle interactions) lead-scintillator calorimeter consisting of 44 modules and is read out via wavelength shifting fibers by Multi-Avalanche Photo-Diodes (MAPDs) with an active area of 3 mm² \times 3 mm² and a pixel density of 10⁴ per mm².

2.4 The Ring Imaging Cherenkov detector (RICH) of CBM

A detailed report on the CBM-RICH detector can be found in the Technical Design Report ([18]). Thus, only a few important aspects will be presented here in short, which are relevant for this thesis.

The RICH detector of CBM is the main detector to identify and separate electrons and pions in collisions from lowest momenta up to 8 GeV/c – 10 GeV/c and with a desirable pion suppression of at least a factor of 100. To achieve these goals it consists of a gaseous CO₂ (refractive index $n = 1.00045$) radiator of 1.7 m length, spherical mirrors made of an reflective aluminium-coated glass substrate with a protective MgF₂ coating and a curvature radius of 3 m, and a photon detection camera of multianode photomultipliers (MAPMTs).

The environment, in which the CBM-RICH will be operated, covers several important aspects ([18]), which need to be considered in the development:

- high primary particle interaction rates with the target of up to 10 MHz, thus requiring a clear and fast signal response from the sensors and an adequate fast read-out chain,
- track multiplicities of around 1000 particles per central Au + Au collision,
- high radiation level within the detector,
- large number of secondary electrons produced in the material upstream the RICH, causing high ring densities in the RICH,
- magnetic stray field from the close-by magnet, especially in the regions of the sensor camera,
- possibility to exchange RICH detector and Muon Detection System in order to allow independent measurements of the di-lepton signals at low and high masses,
- beam pipe with low material budget and beam pipe access.

MAPMTs are best suited for the needs of the CBM-RICH as they provide a high granularity, high detection efficiency, a very good noise behaviour and a stable operability. The determination of an exact type of MAPMTs was aim of several prototype beamtests at the PS accelerator at CERN, where several types could be compared under same conditions. A detailed overview of all tested devices with focus on the 2012 beamtest is given in Chapter 3.

The read-out of the sensors will be done with the DiRICH electronics ([19, 20]), which is currently being developed at GSI together with our group at the University of Wuppertal, and which will also be used for the upgrade of the RICH detector of HADES (High Acceptance DiElectron Spectrometer). Thus the HADES-RICH will suit as an in-experiment testbench for the new electronics and according modifications can be done for the CBM-RICH electronics, if necessary.

The modules of the DiRICH electronics are very compact and combine the discrimination of signals, the time stamp measurement, as also the data handling itself on one single board using the new developed Lattice ECP5-85F FPGA. Each DiRICH module can handle 32 channels, i.e. two modules are needed per MAPMT (with a total of 64 channels). To reduce the number of necessary cables for data transfer, additional concentrator boards (data combiner modules) are developed, which will combine the data from 12 DiRICH modules (i.e. 6 MAPMTs) to one single fiber output.

The whole CBM-RICH photon camera will be divided into several small PCB backplanes (camera modules), each carrying 3×2 MAPMTs (which is the reason for the concentrator board covering 12 DiRICH modules). For better operability each backplane will have one power module, providing power for the electronics (low voltage/LV of a few V) and also for the MAPMTs (high voltage/HV of around 1000 V). A schematic drawing, showing one backplane with 12 DiRICH modules, the concentrator board, the power board, and 6 MAPMTs, is shown in Figure 2.5.

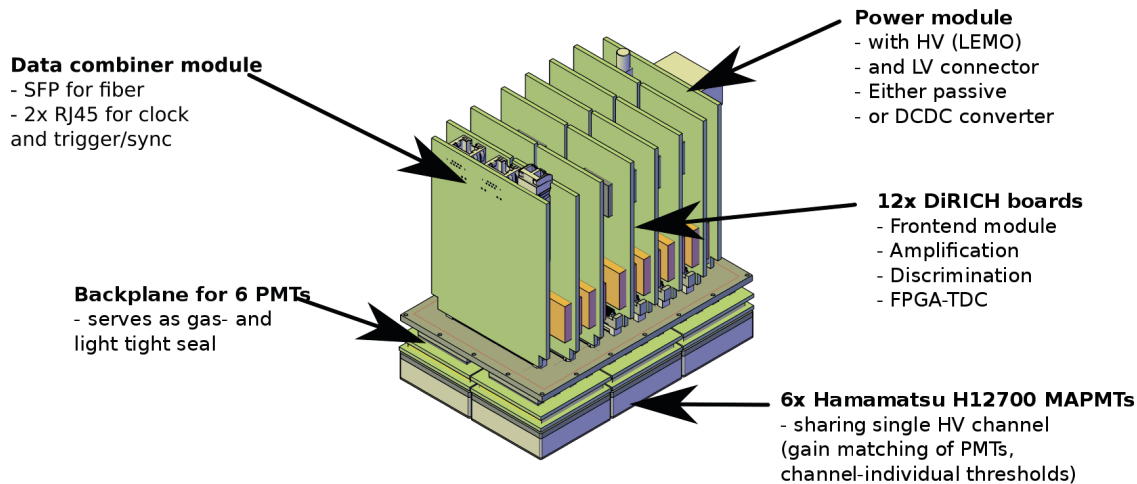


Figure 2.5. – Schematic layout of one camera module for the CBM-RICH camera, designed to carry 6 MAPMTs. It consists of 12 DiRICH modules (2 per sensor), one power module, and one data combiner module, all developed as plug-in devices on the PCB backplane.

The sensor camera will have a size of roughly 2.4 m^2 , divided into two planes above and below the central beamline. It will carry around 900 – 1000 MAPMTs, each having 64 pixel, resulting in a total of around 58 000 – 64 000 channels. The small size of the camera modules allows for specific adjustments of the camera construction in terms of tilting angles of each module and distance of

each module to the mirror plane, as the ideal camera plane has a curved shape. At the moment two different camera layouts are under investigation: a wing-shaped geometry, which consists of two flat planes of sensors arranged like two wings (can be identified in Figure 2.6, see also [21]), and a curved geometry, which is directly derived from the ideal camera plane (see [22]).

The RICH detector, and especially the sensor plane, is placed directly behind and close to the magnet and therefore suffers from its magnetic stray field. The MAPMTs can only be efficiently operated at a magnetic field of a few mT, and thus need a dedicated shielding box, as the stray field reaches higher values in the region of the camera. The exact layout of the shielding box depends on the final layout of the camera, and also on requirements regarding space for electronics and sufficient cooling. Thus only preliminary layouts and simulations of the magnetic field including the shielding box exist, indicating that the low level of magnetic field in the region of the sensors can be achieved.

One of the latest mechanical design solutions of the RICH detector is shown in Figure 2.6. The yellow boxes mark both sensor planes (left picture, shown in beam direction), with the mirror tiles in several colours, and the complete support structure (including the dedicated mirror holding structure) in grey. The geometrical acceptance of the detector is indicated by the transparent grey cone.

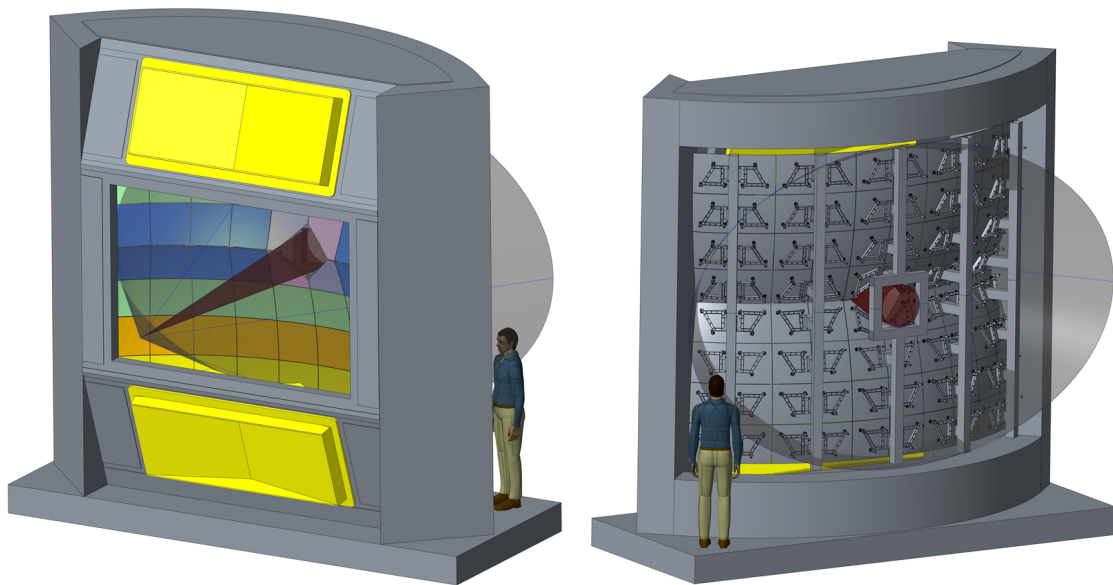


Figure 2.6. – Latest RICH detector design solution (from [23]), shown in beam direction (left) and in opposite direction (right). The sensor planes are shown in yellow, the mirror tiles in several colours, and the complete support structure in grey. The transparent grey cone marks the geometrical acceptance.

Photon Sensors for the CBM-RICH

The CBM-RICH aims at detecting Cherenkov photons at a single-photon level. Due to the different requirements, which will be discussed in Section 3.1, multi-anode photomultiplier tubes (MAPMTs) or microchannel plate photomultiplier tubes (MCP-PMTs, will be abbreviated as MCPs) are considered to be the best choice for the photon detector camera.

As photomultipliers offer very good properties and especially multi-pixel types also became broadly available nowadays at acceptable costs, several other (Cherenkov-) detector groups consider upgrading their photon detectors with photomultipliers aswell, e.g. for the HADES-RICH or the LHCb-RICHes.

From all the available sensors a few candidates matching our requirements were selected for further tests: the Hamamatsu H8500 MAPMT, the Hamamatsu R11265 MAPMT, and the Planacon Photonis XP85012 MCP (and, as a single-photon optimized successor of the H8500, also the Hamamatsu H12700 MAPMT).

Section 3.1 summarizes the special requirements the photon sensors have to fulfill for the CBM-RICH, and motivates the choice of sensor candidates, which were tested. Detailed properties of all considered and tested devices are then given in Section 3.2 and a few results from laboratory measurements of the quantum efficiency of the sensors are shown in Section 3.3.

3.1 Requirements for photon sensors

For the CBM-RICH detector the photon sensors must fulfill several requirements, which stem from the harsh environment inside the beamcave, the position of the detector directly behind the magnet, and the performance goals of the CBM-RICH.

A lot of tests were done in the laboratory and also during several beamtests and the achieved results were implemented in the simulations to deduce information about the behaviour of the full CBM-RICH later, especially with respect to the physics goals of CBM.

A detailed discussion of the requirements can be found in the CBM-RICH Technical Design Report (TDR, [18]). In 2015, also based on the information obtained in this work, a final choice was made, and the H12700 MAPMT was chosen to be used in the CBM-RICH. In the following the requirements leading to this choice are briefly recapitulated (based on the TDR).

Photon Detection Efficiency

One of the most important aspects for the photon sensor candidates is the detection efficiency for incoming Cherenkov photons, which is mainly determined by the quantum efficiency of the photocathode, but also by the collection efficiency and the window material. According to simulations the CBM-RICH will detect between 20 and 30 Cherenkov photons per electron ring (radius $r \approx 45$ mm).

As the Cherenkov spectrum is proportional to $1/\lambda^2$, i.e. most of the photons are generated in the UV-range, the quantum efficiency should match this spectrum as good as possible. With a natural cut-off in the spectrum below 180 nm (at atmospheric pressure) due to the CO₂ radiator, the photocathode must yield high efficiencies in the range up to around 400 nm. The cathode types best matching these needs are based on Bialkali or Multi-Alkali materials (e.g. standard Bialkali, Super-Bialkali). Bialkali cathodes are typically used wherever visible or UV light should be detected. The measured quantum efficiency curves of the tested sensor candidates can be found in Section 3.3 and match these requirements quite well.

Another important aspect influencing the photon detection efficiency is the material of the PMT window. Several types of window materials exist, all of them with different advantages and disadvantages. The most common material is borosilicate, which is not transmissive in the deep UV-range (< 300 nm) and therefore doesn't suit our needs. Other types of window materials are UV-glass, with a good transmission even in the UV-range down to 185 nm, fused or synthetic silica, with a transmission down to 160 nm but with a complicated assembly process due to the thermal expansion coefficient, or sapphire or quartz windows, which provide good transmissive behaviour down to 150 nm. Transmission curves from different window materials can be found in Figure 3.1. For the Hamamatsu photomultipliers considered here, only UV-glass is available, whereas for the MCPs also fused silica or sapphire windows are available.

Radiation Hardness

The PMT camera of the CBM-RICH is located directly behind the CBM dipole-magnet and thus relatively close to the interaction point. The PMTs are exposed to significant amounts of ionizing radiation, neutron flux, and high-energy hadron flux, although they are not placed within the acceptance of CBM and therefore aren't exposed to direct particle flux from the target (especially as the magnet yoke will shield a large fraction).

Realistic FLUKA simulations were done to estimate the amounts of collected doses of CBM running for two months at maximum intensity. The results yield values in the region of the photon sensors up to a maximum of ≈ 100 Gy ionizing dose, or $1 \cdot 10^{11}$ n/cm².

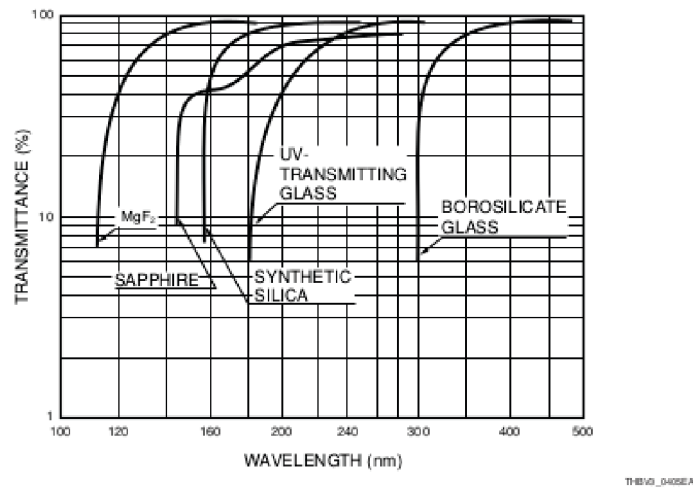


Figure 3.1. – Transmission curves of different photomultiplier window materials. (from [24]).

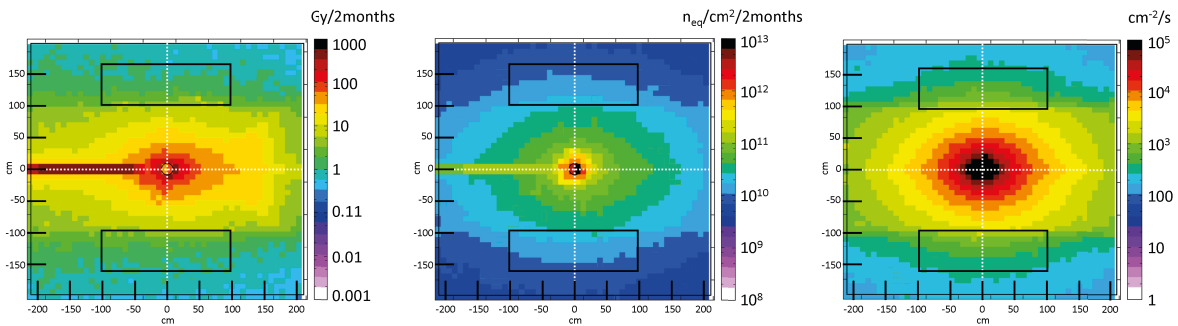


Figure 3.2. – Radiation environment for the RICH photon detector plane: Ionisation dose in Gy per 2 months (left), NIEL in $n_{eq}/cm^2/2\text{months}$ (mid), high-energy hadron fluences in $1/cm^2/s$ (right). Plots correspond to approx. $5 \cdot 10^{15}$ beam particles, i.e. 2 months of CBM running with beam intensities of 10^9 ions/s. The photodetector position is indicated in the figures: Lower and upper edge of the photodetector are at ± 97.5 cm and ± 157.5 cm respectively. Vertical dimensions are ± 1 m. (from [18]).

The distribution of the ionization dose, neutron flux, and high-energy hadron flux from the FLUKA simulations are shown in Figure 3.2. The expected doses in the region of the photon detector are in the range of 1 Gy/2 months – 20 Gy/2 months for the ionizing dose, $8 \cdot 10^9$ $n_{eq}/cm^2/2$ months up to $5 \cdot 10^{10}$ $n_{eq}/cm^2/2$ months for the NIEL, and $2 \cdot 10^2$ $cm^{-2} s^{-1}$ up to $5 \cdot 10^3$ $cm^{-2} s^{-1}$ for the high-energy hadron flux.

According to [24] the most relevant part of a photomultiplier affected by radiation is the glass window, which will tend to colour and loose transmission and thus will cause a loss in detection efficiency. The extend of glass degradation under radiation depends on the glass material, as fused silica is more radiation tolerant compared to UV-extended borosilicate glass ('UV-glass') or even standard lime glass.

Even the lowest doses tested by Hamamatsu (min. of $1.4 \cdot 10^5$ R = $1.4 \cdot 10^3$ Gy and $6.4 \cdot 10^{13}$ n/cm^2 respectively) are 1 – 2 orders of magnitude higher than the doses expected in CBM for two months running at full intensity. From that it can be stated that radiation damage of the photon sensors

should be no limiting factor in CBM. This can be confirmed by measurements done in our group showing the different behaviour of borosilicate glass and UV-glass under neutron radiation and high-energy gamma radiation ([25]).

Magnetic Field Resistance

Magnetic fields stronger than a few mT pose a problem to photomultipliers as they strongly affect detection efficiency, mainly by influencing the electrons in particular between the cathode and the first anode of the photomultiplier. In CBM the photon detector plane of the RICH detector is located directly behind the magnet yoke and is therefore exposed to a comparatively large magnetic stray field. As the field in this region exceeds the limits of photomultipliers, an additional shielding will be necessary. At the moment the plans include a thick iron box around the whole sensor camera and, if applicable and useful, a μ -metal shield grid between all sensors. Simulations show, that such a shielding box is sufficient to reduce the magnetic field in the region of the sensors down to an acceptable value.

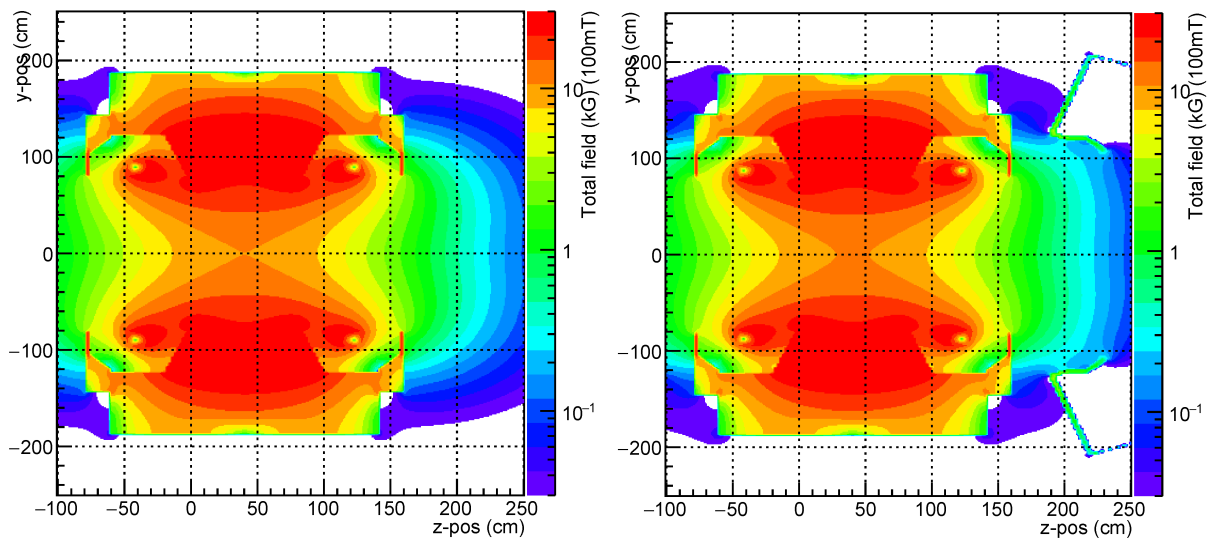


Figure 3.3. – Effects of a shielding box around the sensor camera of the CBM-RICH. The left picture visualizes the magnetic field strength in the region of magnet/MVD/STS and the front parts of the RICH without the shielding box, in the right picture the shielding box is included (clearly visible on the upper right and lower right part). With the shielding box the magnetic field strength in the region of the sensor camera is decreased to an acceptable value. (from [26])

As possible alternative also MCPs were considered, which provide a large magnetic field resistance and were specifically developed for environments within magnetic fields. They are immune to magnetic fields up to field strengths of 1 T – 2 T which would be far above the field strengths expected in the region (≈ 35 mT).

Hit Rate Stability

A maximum rate of around 700 kHz/pixel can be estimated in the regions of highest track density. The relevant property of a photomultiplier is here the maximum average anode signal current. For the considered H8500 and R11265 MAPMTs this value is at 100 μA , and 3 μA for the XP85012 MCPs. One single-photon pulse generates a signal of 10^6 electrons (equivalent to the typical gain) equal to 150 fC. Provided the maximum rate mentioned above, this would yield a maximum anode signal of 0.1 μA per pixel or approx. 5 μA per photomultiplier and is therefore no limiting factor for the Hamamatsu MAPMTs but might become a problem for the Photonis MCPs in the high-density regions.

Dark rate

In photomultipliers the dark rate is caused by thermal emission of electrons from the photocathode or from one of the dynodes. CBM will use free-running electronics and therefore capture all signals above a certain threshold. Each signal, caused either by a real hit or by the dark rate will therefore increase the data rate and processing time of each event.

Photomultiplier tubes provide a very good behaviour in terms of dark rate of up to just 1 Hz mm^{-2} cathode area (for bialkali cathodes). MCPs show a slight worse behaviour than photomultipliers with a dark rate one or two orders of magnitude higher, which is still manageable.

3.2 Sensor-candidates for the CBM-RICH

As described above, photomultipliers or microchannel plates are the only photon detection techniques able to cope with the different requirements of the CBM-RICH. There are only a few manufacturers producing photomultipliers, among them Hamamatsu Photonics and Photonis Planacon, whose sensor types were considered as candidates. In this chapter the details of all considered candidates will be discussed.

Altogether four different basic models were considered as candidates for the CBM-RICH: the Hamamatsu H8500 MAPMT, the Hamamatsu R11265 MAPMT, the Planacon XP85012 MCP, and later also the newly developed Hamamatsu H12700 MAPMT.

Hamamatsu H8500 The first candidate, which was used also as design baseline for the development of the CBM-RICH, is the Hamamatsu H8500 MAPMT. The Hamamatsu H8500, in different configurations (cathode material, dynode stages, window material), was subject of study during the 2011 CBM-RICH beamtest at CERN/PS-T9 and in the subsequent beamtests in 2012 and 2014 also at CERN/PS-T9. The H8500 yielded very good results within all tests, although not primarily recommended for single-photon measurements by the manufacturer.

The Hamamatsu H8500 MAPMT has an overall good efficiency together with a high geometrical coverage (89 %) and a moderate price. Two different versions could be tested: one with a Bialkali cathode and 12 dynode stages and one with a Super-Bialkali cathode and 8 dynode stages (\rightarrow also called H10966). Due to the manufacturing process it is (unfortunately)

not possible to produce this MAPMT with a Super-Bialkali cathode and a 12-stage dynode system. As most of the Cherenkov photons are excited in the UV-range we only tested MAPMTs with an UV-extended borosilicate window.

The outer dimensions of this type are 52 mm × 52 mm with an active area of 49 mm × 49 mm and a total of 8 × 8 pixel of roughly 6 mm × 6 mm each.

Several different configurations were tested, following the naming scheme of Hamamatsu: the H8500C and H10966A types get their HV via a dedicated cable, whereas the H8500D (and H10966B, not tested) have a dedicated pin for the HV. An additional differentiation is marked by the subsequent number. The last digit of this number marks the window material ('3': UV-window, '0': standard borosilicate window), and the first one/two digits mark the cathode material ('10': super-bialkali, '0': bialkali).

Hamamatsu R11265 A new development at that time was the Hamamatsu R11265 MAPMT. It has just a fourth of the size of the H8500 but has an improved dynode system specifically developed for single-photon measurements, hence being the recommended MAPMT type for single-photon measurements by the manufacturer. Due to the smaller size of 26.2 mm × 26.2 mm (and only 4 × 4 pixel) the production process allows for combining a Super-Bialkali cathode with a 12-stage dynode system. It has also an UV-extended borosilicate window. One important aspect is the active area of only 23 mm × 23 mm and the therefore low geometrical coverage of 77 %.

This sensor has been tested in the 2012 beamtest in direct comparison to the H8500 MAPMT and the XP85012 MCP.

Photonis XP85012 The Photonis XP85012 MCP is a very different device compared to the MAPMTs due to the different way of electron amplification, by using microchannel plates instead of a dynode system. The reason to consider this type is the high magnetic field resistivity of up to 2 T (the MAPMTs can cope with around 1 mT) to be able to stand the magnetic stray-field of the CBM magnet in the region of the CBM-RICH camera without any additional shielding (which will be necessary for the MAPMTs).

This type is at the moment only available with a Bialkali cathode but with a quartz or sapphire window, which have a lower wavelength cut-off than borosilicate windows. Its outer dimensions are 59 mm × 59 mm with an active area of 53 mm × 53 mm (and therefore a geometrical coverage of 80 %).

Hamamatsu H12700 The Hamamatsu H12700 is the successor of the H8500 MAPMT with two main improvements. The most important improvement was the dynode system, which consists of 10 stages and was optimized towards single-photon detection. It is very similar to the single-photon optimized dynode system of the R11265. In addition the Bialkali cathode type was further improved, granting a few percent increased maximum quantum efficiency. The H12700 MAPMT is a very new development and became available in 2013/2014. Hence, it could not be tested in the 2012 beamtest.

All important properties of the tested sensors are summarized in Table 3.1, together with the (relative) number of detected Cherenkov photons, which has been derived by folding the quantum efficiency of the sensors with the Cherenkov spectrum.

Table 3.1. – Important properties of tested MAPMTs and MCPs and the calculated (relative) number of detected Cherenkov photons (by folding the photon yields shown in Figure 3.4 with the Cherenkov spectrum).

MAPMT type	thickness of front glass	window	photo-cathode	no. of dynodes	relative no. of det. Ch. photons
H8500D-03	1.5 mm	UV-window	BA	12	71.6
H8500C-100-mod8	1.5 mm	borosilicate	SBA	8	62.6
H10966A-103	1.5 mm	UV-window	SBA	8	89.7
R11265-103-M16	0.8 mm	UV-window	SBA	12	100
XP85012	n/a	UV-grade fused silica	BA	MCP	75.7
H12700	n/a	UV-window	BA	10	n/a

3.3 Laboratory measurements on quantum efficiency of specific sensor samples

To judge and compare the different types of sensors with regard to the above mentioned requirements of the CBM-RICH detector several test methods were developed and improved in the recent years. With these laboratory measurements it is possible to investigate on properties which cannot be determined by in-beam tests, especially as these test setups are mainly designed for one-device tests.

The most important property of photomultiplier tubes is the quantum efficiency of the photocathode, as this has the major influence on the photon detection probabilities. A detailed description of the used measurement setups as also all the results can be found in [27]. In Figure 3.4 the measured quantum efficiencies for the devices tested during the beamtest can be found (left for MAPMTs and right for one MCP in comparison with one H8500 MAPMT), with an additional curve visualising the shape of the Cherenkov spectrum and therefore emphasizing the important wavelength region (\rightarrow which are low wavelengths).

The results show, that the quantum efficiency of the Hamamatsu MAPMTs always peaks at around 350 nm and goes down (in a roughly symmetrical shape) to zero for higher and lower wavelengths. The cut-off of the data at 200 nm is due to the limited possibilities of the testing facility. Using non-UV-glass as window material results in a wavelength cut-off at around 280 nm, which strongly affects the possible number of detected photons due to the shape of the Cherenkov spectrum (see also Table 3.1). The difference of a BA and a SBA cathode is a varying maximum quantum efficiency, with around 28 % for BA and around 38 % for a SBA cathode.

In contrast the measured MCP shows quite a different shape of the quantum efficiency, also peaking at around 350 nm, but gaining in efficiency at very low wavelengths (below approx. 260 nm). The main reason here is the different window material, as the quartz window of the MCPs shows a higher UV-transparency in comparison to the UV-glass windows of the MAPMTs.

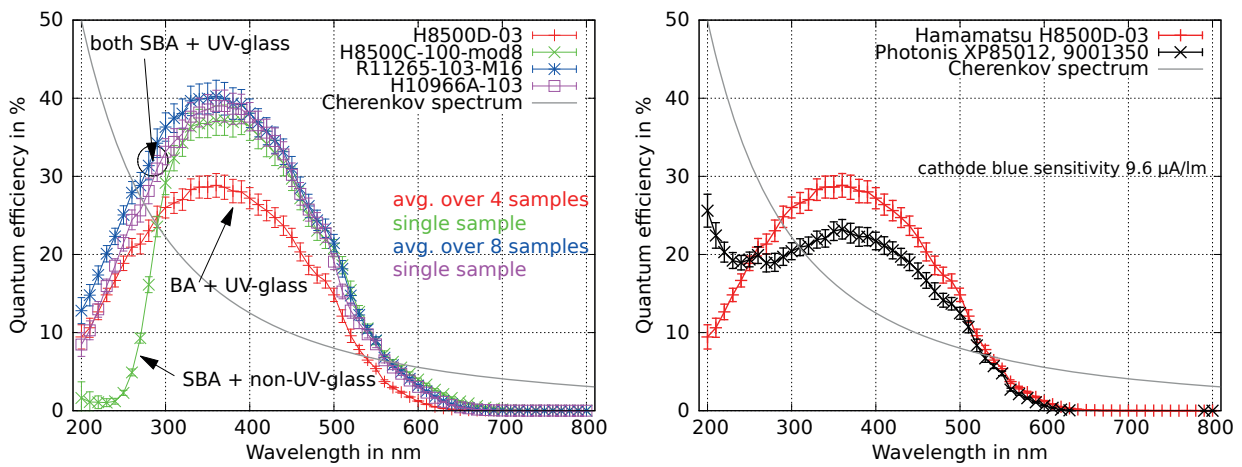


Figure 3.4. – Left: Measured quantum efficiencies of several Hamamatsu MAPMTs: H8500D-03 (red; averaged over 4 samples), H8500C-100-mod8 (green; single sample), R11265-103-M16 (blue; averaged over 8 samples), H10966A-103 (purple; single sample). For comparison the Cherenkov-spectrum with $1/\lambda^2$ is also plotted (gray). Right: Measured quantum efficiencies of 2 samples of Photonis XP85012 MCPs. For comparison the QE of Hamamatsu H8500D-03 MAPMT and the Cherenkov-spectrum are also shown.

Overview of the 2012 prototype beamtest at CERN

After a successful beamtime with the CBM-RICH prototype in 2011, in which the prototype detector could be put into operation for the first time and valuable knowledge, in particular on the operation of the new nXYter-based readout chain, could be obtained, a second beamtime was performed in 2012 with some slightly modifications of the prototype camera and a further extended list of goals. Main goals of the 2012 beamtest were the comparison of the three photon sensor types (H8500, R11265, XP85012) under realistic conditions, further studies of the wavelength-shifting films (WLS; [28, 29]), and mirror misalignment studies ([30]).

In Section 4.1 the prototype will be discussed, including a brief description of general system-components and a detailed description of the prototype camera system. Section 4.2 includes a short introduction to the properties of the used beamline and an overview of the complete setup during the beamtest (which included also prototypes of other subdetector groups).

4.1 The CBM-RICH prototype

To be able to study all the different aspects not only within simulations but also under realistic conditions, a dedicated CBM-RICH prototype has been built, matching the design of the CBM-RICH detector as close as reasonable. These important properties include essentially the radiator type (CO₂) and the radiator length of 1.7 m, the dimensions of the mirror tiles (curvature radius 3 m, mirror tile size of 40 cm × 40 cm) and the manufacturer of the mirror tiles (JLO Olomouc). An important aspect was the newly developed photon camera, which this time allowed for the comparison of all three considered sensors in a common detection plane.

Technical drawings of the prototype (side-view) and the mirror-system can be seen in Figure 4.1. The prototype has a size of 2.4 m × 1.2 m × 1.4 m, is made of stainless steel, and is also gas-tight.

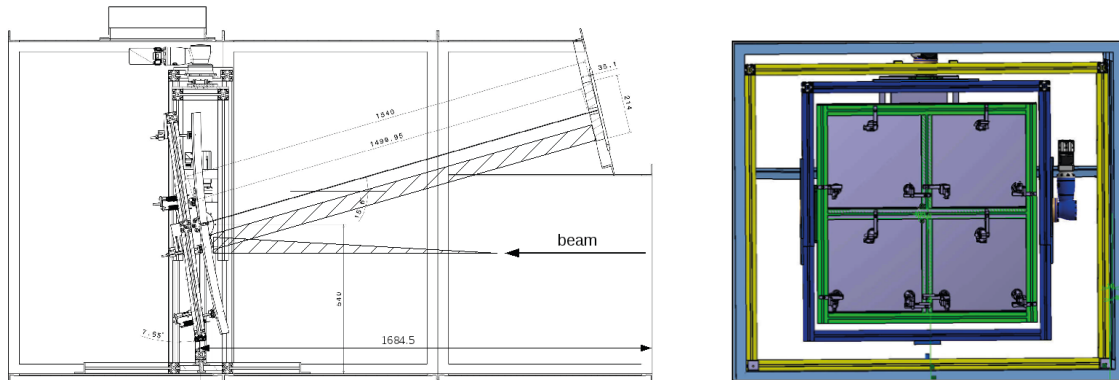


Figure 4.1. – Left: Technical drawing of the CBM-RICH prototype box with mirrors on a rotatable frame. The photon detector is mounted on the upper right side, above the beam entry. The hatched area visualizes the Cherenkov cone and its reflection onto the photon detector. Right: The mirror system. Each mirror tile is adjustable at three points. From [18].

The front and the back are made of plastic boards of 10 mm and 20 mm, respectively, and contain dedicated entrance and exit windows of 2 mm thick plastic. These thin windows should keep particle scattering inside the prototype box and also behind it low (for the other detectors which were tested during the beamtest and were positioned behind the RICH box).

Several rails are installed inside the box to be able to mount and also completely remove a frame holder, on which the complete mirror system is mounted. Removing the mirror system from the box is necessary for an appropriate adjustment of the mirror tiles so that they form a homogeneous spherical mirror plane. This adjustment is done with a laser placed in the centre of curvature of the mirrors and the minimization of the area of the superimposed images of the laser.

An additional light pulser system made of a plastic tube and containing several LEDs (245 nm, 275 nm, 470 nm), a light fibre coupled to a picosecond pulsed laser (405 nm), and an optical diffuser, big enough to cover all light sources, is installed on top of the mirror frame holder. This light pulser system points directly towards the photon camera illuminating it nearly homogeneously. The LEDs are driven by a pulse generator. Only one of these four light sources is used at the same time. The light pulser system is operated in parallel to the overall data taking, with a low trigger rate of 5 Hz to not disturb the general data taking. The differentiation of hits from the beam and hits from the light pulser system is done based on different trigger-timing, and also via simple selection of a trigger number in the analysis. A picture of the mirror frame holder with the light pulser system on top is shown in Figure 4.2.

The photon camera is positioned above the front window of the prototype box, tilted by 74° (with respect to the z-axis/horizontal beam axis) to match the geometry and to keep distortions of the Cherenkov rings low. It can completely be removed. By rotating the focussing mirror around its x- and y-axis the focussed Cherenkov ring image could be moved to different positions on the photon detector surface, thus illuminating different PMTs. Due to the low angular divergence of the incoming beam particle the resulting ring image is always on the same ring position (for a fixed mirror rotation) covering 2×2 sensors (for H8500 and XP85012; for R11265 this is a total of 8 sensors due to the different size and arrangement) at a time, with an electron ring radius of around 45 mm.

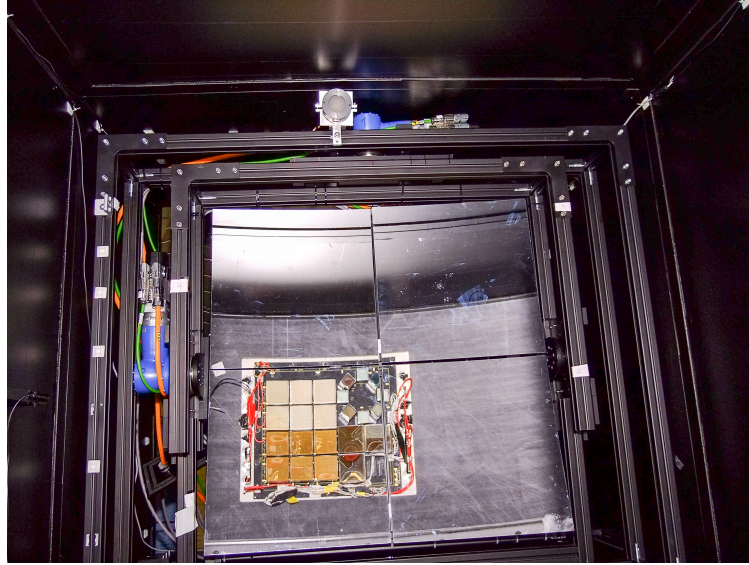


Figure 4.2. – Installed mirror frame holder inside the CBM-RICH prototype with the light pulser system on top of the frame. Visible is only the diffuser mounted inside a plastic tube. A picture of the photon camera can be seen in the mirror.

For the prototype three main system components have been developed: the gas system, the mirror system, and the photon camera. The gas system should keep the radiator at a high purity level (low fraction of O_2 and H_2O) and a constant overpressure of 2 mbar above atmospheric level. The gas system and the mirror system are of less relevance for the presented work and will therefore only be briefly discussed in Section 4.1.1, whereas the photon camera and its read-out system will be presented in detail in Section 4.1.2 and Section 4.1.3.

4.1.1. General system components

The gas system and the mirror system were designed as standalone systems. They are important to operate the CBM-RICH prototype successfully and under stable conditions but are not relevant for the analyses and hence will only be discussed briefly. More details can be found in the RICH Technical Design Report ([18]).

The gas system: To ensure stable conditions of the CO_2 radiator a dedicated gas system was build which should keep the radiator at a constant overpressure of 2 mbar relative to the atmospheric pressure and the contamination with O_2 and H_2O as low as possible (100 ppm and 200 ppm, respectively). The gas system was designed such that it can also be used for the full CBM-RICH detector later with just a few modifications.

The conceptual design of the gas system follows the scheme of gas systems designed for the two experiments STAR and PHENIX at the Brookhaven National Laboratory (BNL) ([31, 32]). The gas system can operate at two different modes, either in normal operation or in purging mode. During normal operation it is run in a closed-circuit mode with the majority of the gas recirculating through the prototype and in case only a small portion of fresh gas being added. For purging it is run in an open configuration.

To ensure clean and stable conditions up to 30 % of the circulating gas can be passed through the purifier and dryer to remove oxygen and moisture. The purifier uses active copper for cleaning which is operated at a temperature of 220 °C. The dryer consists of molecular sieves operating at 22 °C.

Several sensors are included which allow for monitoring the amount of oxygen and moisture and also of all relevant process variables. A dedicated control system monitors all these sensors and provides differential pressure stabilization ([33, 34]).

During the beamtest the gas system worked very successful, achieving a constant overpressure of (2.00 ± 0.15) mbar (although the barometric pressure changed in the range of 37 mbar). Also impurity levels downstream of the purifier and the dryer could be kept at a low level of 9 ppm of oxygen and 15 ppm of moisture ([35]).

The mirror system: The mirror system is an integral component of the CBM-RICH, but also of the CBM-RICH prototype. It focusses all generated Cherenkov photons onto a ring which can be detected by the photon sensors.

From previous tests ([36]) it was known that the manufacturer JLO Olomouc produces the mirrors best fitting to the requirements of the CBM-RICH and therefore several mirror tiles were ordered to be used in the CBM-RICH prototype. All four mirror tiles were kept in place via three actuators on each tile and were mounted on an aluminium frame. The purpose of these actuators is the possibility to adjust all mirror tiles such that they share one common focal point and therefore form one big spherical mirror plane. To move the resulting Cherenkov ring onto different positions on the camera the whole aluminium frame could be tilted in two directions. All positions and their corresponding settings of the mirror system could be saved in a dedicated mirror positioning control system and individually selected for each measurement ([37]). With this mirror system it is possible to project the Cherenkov ring image on different photon sensors, and to directly compare the sensor response. The high precision of the mirror system, when selecting a specific saved position, allows to adequately repeat measurements on various positions.

4.1.2. Prototype photon camera system

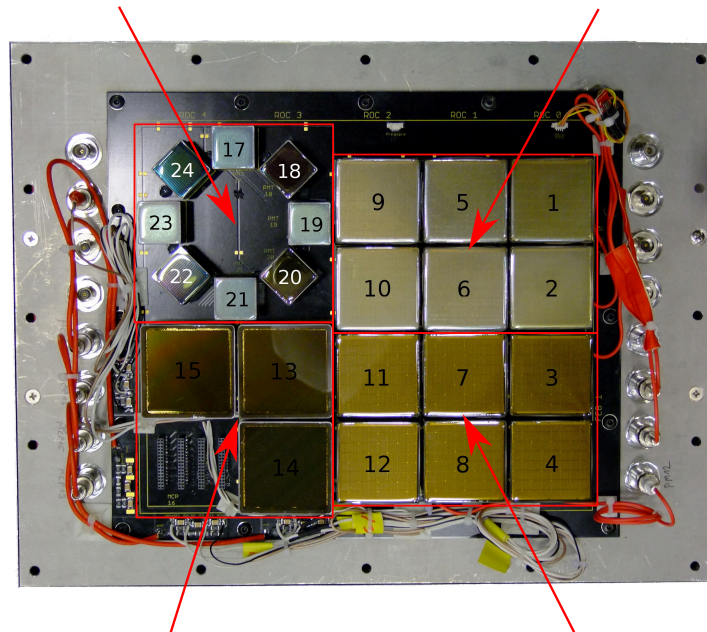
One main goal of the beamtests in 2011, and especially in 2012, was the comparison of various photon sensors with the aim of deciding which one to use in the full CBM-RICH. The tested devices of the 2012 beamtest include various types of the Hamamatsu H8500 MAPMT (with various dynode systems and cathode materials), the Hamamatsu R11265 MAPMT, and the Photonis XP85012 MCP.

The different sensors were arranged on the read-out plane as shown in Figure 4.3. Only 8 pieces of the R11265 MAPMT were available for testing, which was the reason for arranging them in the ring-like shape to cover the highest fraction of electron ring Cherenkov photons in a rather symmetric way (this also means that pion rings at low momenta cannot be detected with the R11265 PMTs due to the smaller Cherenkov ring radii). It also contained 3 MCPs, covering 3/4 of an electron Cherenkov ring. The missing 4th MCP was not available in time for the beamtest. The spacing between the H8500 MAPMTs was 2 mm, and 1 mm for the three MCPs. By tilting the mirrors it was possible to focus the Cherenkov rings on different positions on the camera. These

positions include tests, when only one type of sensor was covered, but also comparison-tests where the two halves of the ring lie on different sensor types.

To also be able to judge on the minimum expected quality of the production chain of Hamamatsu, we got three H8500 sensors which were explicitly marked as ‘bad’ by Hamamatsu. Two of those sensors were used during the beamtest covering one half of a ring (MAPMTs #3 and #4).

8x Hamamatsu R11265 (half covered with WLS) 6x Hamamatsu H8500 with WLS



3x Photonis XP85012 MCP

6x Hamamatsu H8500 without WLS

Figure 4.3. – CBM-RICH prototype camera during the beamtest 2012. The numbers indicate the position used in the analysis (compare Table 4.1).

Some of the photomultipliers were covered with a wavelength-shifting film (WLS) which was removed during the beamtest (run #41). This can be recognized in Figure 4.3 by the milky-looking surface of the six upper H8500 MAPMTs and each second one of the R11265 MAPMTs. The WLS shifts photons from the deep-UV region into the blue region by absorbing it and re-emitting a photon at a larger wavelength. Thus the WLS aims at increasing the detection efficiency of the photomultiplier in the UV-region. A realistic test of the performance gain due to the WLS coating is only possible using real Cherenkov photons due to their specific spectral shape, which can not be easily reproduced in the lab. The WLS has also been studied in the 2011 beamtest and the thickness of the coating was optimised for the 2012 beamtest. The analyses of the WLS and the study of its behaviour were part of a dedicated thesis ([27]) and will not be discussed here.

An overview of all used sensor devices during the beamtime can be found in Table 4.1 including the position of the sensor on the camera, the serial number, and also the gain as given by the manufacturer.

All sensors were mounted on a dedicated PCB (‘MAPMT carrier board’). On the other side of the carrier board the connectors for the attenuator boards are placed. The whole carrier board was fix mounted on an aluminium frame which could be completely taken off the prototype box, e.g. to exchange some sensors or to remove the WLS coating. With this construction only the sensors are

Table 4.1. – Positions and serial numbers of the PMTs used during the beamtime. In addition the gain as given by the manufacturer is included.

Position	Serial No.	Type	Gain [10^6]	additional info
1	ZL003	H8500	0.35	8-stage version (H10996A-103)
2	ZL001	H8500	0.40	8-stage version (H10996A-103)
3	CA5101	H8500	1.20	SOR PMTs (marked 'bad')
4	CA5093	H8500	1.48	SOR PMTs (marked 'bad'), → changed to CA5535, run044
	CA5535	H8500	1.82	SOR PMTs (very 'bad')
5	DA0154	H8500	1.64	-
6	DA0141	H8500	2.06	-
7	DA0140	H8500	2.24	-
8	DA0134	H8500	2.16	-
9	DA0142	H8500	1.77	-
10	DA0147	H8500	1.46	-
11	DA0150	H8500	2.27	-
12	DA0129	H8500	3.55	-
13	MCP339	XP85012	n/a	MCP, borrowed
14	9001350	XP85012	n/a	MCP
15	MCP336	XP85012	n/a	MCP, borrowed
16	-	XP85012	-	not delivered in time
17	ZN0593	R11265	6.27	-
18	ZN0591	R11265	4.43	-
19	ZN0590	R11265	2.66	-
20	ZN0768	R11265	2.14	-
21	ZN0733	R11265	2.22	-
22	ZN0734	R11265	1.80	-
23	ZN0731	R11265	2.03	-
24	ZN0557	R11265	2.46	-

inside the prototype box and everything else (mainly electronics) outside. One main advantage of this is the easier accessibility of all components of the read-out electronics without affecting the radiator volume inside the box (especially keeping it from being contaminated with oxygen or water). In addition several connections could be established without the necessity of special lead-throughs, e.g. power connectors and cooling hoses of the electronics. Only HV-supply of the sensors required dedicated lead-throughs. Following the positive experience made during the beamtests, a similar construction of the photon sensor camera is also foreseen for the full CBM-RICH later.

On the inner side (i.e. the side within the box) the carrier board had connectors for temperature and pressure sensors and on the outer side connectors for temperature sensors for each pair of FEBs. All sensors were then connected via I²C bus with an Arduino board which logs all received values from the sensors and sends them via Ethernet to the prototype slow-control system ([38]). The slow-control system ([37]) is based on EPICS and monitors all relevant properties, which include the above mentioned temperatures and pressure, but also the HV of the sensors and their currents.

Each of the sensors had an individual HV supply line, which gave the possibility for slight gain-adjustments due to different gain of the individual sensors (this adjustment was done in run #125 for several sensors based on the fitted amplitude of the single-photon peak in the ADC spectra).

4.1.3. The camera read-out system

The read-out of all sensors was done via charge attenuator boards followed by Front-End Boards (FEBs) based on the n-XYter chip which were controlled and read-out by additional SysCore Read-Out Controller (ROCs). The n-XYter chip ([39]) is an ASIC and has been developed as the common read-out solution for three different neutron detectors, among them a silicon strip detector. The chip is self-triggered and data-driven. With the n-XYter chip it is possible to measure pulse height and time simultaneously. To achieve this each of the single read-out channels (a total of 128 channels are available) has two different shapers with distinct time constants, one optimized for timing resolution (shaping time 18 ns for 30 pF input capacitance), the other one optimized for pulse height resolution (shaping time 140 ns for 30 pF input capacitance). The slow-shaped signal is digitized using an external ADC with roughly 10 bit – 11 bit effective resolution. This very good pulse height resolution is then used for peak detection with a derived signal time stamp from the timing shaper.

As the n-XYter chip was initially designed for the read-out of detectors with much lower signal amplitudes (input signal range $1.2 \cdot 10^5$ electrons) compared to photomultipliers (typical output signal strength 10^6 electrons, corresponding to the gain of $1 \cdot 10^6$), it was necessary to build special attenuator boards for an attenuation of the sensor signal. They were placed in between the sensors and the FEBs. As also the signal strength/gain of the different sensor types slightly varies, attenuator boards with different attenuation factors for the different sensor types were used (see Table 4.2). A circuit diagram of the attenuator boards is shown in Figure 4.4. The attenuation factor only depends on the ratio between the capacitances C_2 and C_1 . R_2 prevents a static charge-up of the otherwise DC-isolated PMT anode pads. R_1 is used to match the input impedance and to minimize reflections.

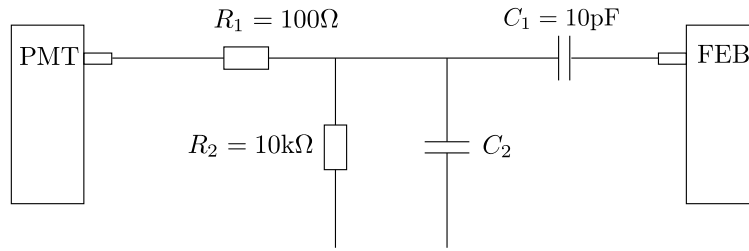


Figure 4.4. – Circuit diagram of attenuator board used for attenuating the signals from the sensors.

Table 4.2. – Capacitances of the attenuator boards in dependence of the PMT.

PMT no.	PMT type	C_2 [pF]	attenuation
1 - 2	H10966A	100	~ 10
3 - 12	H8500	470	~ 47
13 - 15	XP85012	220	~ 22
17 - 24	R11265	680	~ 68

The Front-End Boards were developed at the GSI DetectorLab ([40]). Each FEB contains one n-XYter chip and can therefore be used for the read-out of two sensors with each 64 pixel. In addition to the n-XYter ASIC itself each FEB contains one single-channel 12 bit analogue-to-digital converter (ADC). With this setup a time stamp resolution of 1 ns and a timing precision of ~ 2 ns – 3 ns can be achieved.

To keep the influence of surrounding electromagnetic fields on the analogue signals low, the whole signal chain from the sensor-pins up to the ADC on the FEB was designed in a way that the analogue signal is only transmitted via short PCB tracks without any cables. After conversion of the signal into digital data electromagnetic disturbances are of less relevance and allow for the usage of cables in between the FEBs and the ROCs. In addition each attenuator board was wrapped with a copper shielding plate and the whole camera (i.e. sensor PCB board, attenuator boards, and FEBs) was covered with an aluminium box for further shielding.

The control of the FEBs and the transport of all data and communication with the Data-Acquisition System (DAQ) is done with the SysCore Board/ROC ([41, 42]). It is based on an FPGA and can be connected to a PC either by a 100 Mbit Ethernet link or by an optical link. Each ROC can control two FEBs at the same time. With dedicated software packages it is possible to set various properties of the FEBs and ROCs ('ROClib'), read-out and save the data ('DABC') or monitor and analyse the transmitted data ('Go4').

The n-XYter chip features a strong temperature dependence of the baseline in its analogue part. To achieve stable conditions a dedicated water-cooling was used, keeping the n-XYters at nearly constant temperatures. The temperature of every two FEBs was monitored via digital temperature sensors placed on the coolers.

4.2 Beamtest Overview

A first beamtest of the CBM-RICH prototype took place in October 2011 at the T9-beamline of the CERN/PS accelerator (a main part of the results of the 2011 beamtest can be found in [27]). One year later in October 2012 a second beamtest at the same beamline was done with the aim of further studies. The main goal was the comparison of three different sensor types (H8500, R11265, XP85012), including the investigation of photon detection efficiency, crosstalk, or ring resolution, also depending on the used high-voltage of the sensors or the hardware-threshold of the n-XYter chips. This comparison was of interest due to the complete new dynode system of the R11265 (which should improve detection efficiency) and the different electron multiplication scheme (microchannel plates, instead of a dynode system in photomultiplier) of the XP85012 MCPs (which makes them resistant to magnetic fields).

The test plan also included advanced studies on wavelength-shifting films (WLS) of optimised thickness (which is based on the first data and experience from 2011) on H8500 and R11265 MAPMTs, and mirror-misalignment studies for judging the effect of misaligned mirrors on the ring detection and reconstruction routine.

The T9-beamline is able to provide a secondary beam of electrons, pions, and, to a low fraction, also muons up to a momentum of around 10 GeV/c. At low momenta the electron fraction dominates in the beam but becomes smaller when coming to higher momenta where pions dominate. Each supercycle (approximately every 40 s) provides 1 – 3 spills of ~ 350 ms with each spill containing several 1000 particles. Each electron generates around 200 – 300 Cherenkov photons but due to absorption in the gas radiator, reflection losses on the mirror and low detection efficiency of the photon detectors only 20 – 30 hits per Cherenkov ring are detected.

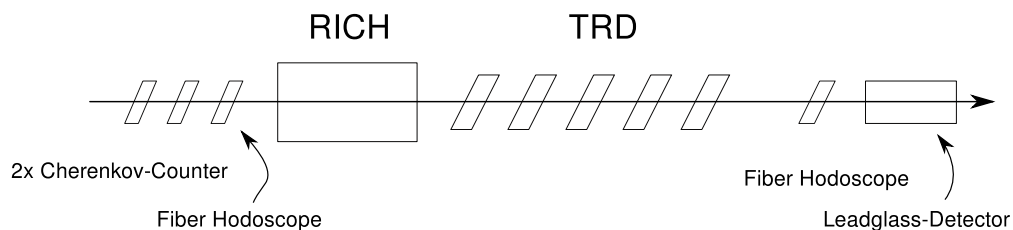


Figure 4.5. – Complete setup during the beamtest 2012. In the front two Cherenkov counters for particle identification and one fiber hodoscope for particle tracking were placed. The CBM-RICH prototype box and several CBM-TRD prototypes were arranged behind them. At last another fiber hodoscope for tracking and a leadglass detector for further particle identification were set up. The beam direction is indicated by a long arrow.

A sketch of the complete beamtest setup 2012 can be seen in Figure 4.5. The beamtime setup includes two additional threshold Cherenkov counters in front of the RICH prototype and a lead glass detector behind all tested detectors for an independent separation of electrons, pions, and muons. The gas pressure in the two threshold Cherenkov counters was adjusted such that one of them only yields a signal for electrons and the other one for electrons and muons; both were blind for pions. With this setting it is possible to distinguish between all three particle types on a event-by-event basis. Further information can be gathered from the leadglass detector. This was not used for the present RICH analyses. For tracking of all particles two fiber hodoscopes

were placed in the front and in the back of all detectors. The data of these fiber hodoscopes is not relevant for the RICH prototype but only for the TRD detectors, as the RICH doesn't need tracking information for the data analyses. In addition the fiber hodoscope in the front provided a coincidence timing trigger signal, and was used for beam alignment and diagnostics.

To be able to compare the different PMT types based on the Cherenkov data, several ring-positions on the camera were defined, with each position covering different PMTs on the camera. Different positions could be illuminated by rotating the mirror accordingly. The absolute rotation angles were stored to achieve reproducible position settings and could be set at any time. The PMT camera with all indicated ring-positions used in the further analyses can be seen in Figure 4.6. Position A was set as a reference position and was regularly measured during the beamtest, especially to be able to verify the stability of the whole prototype system.

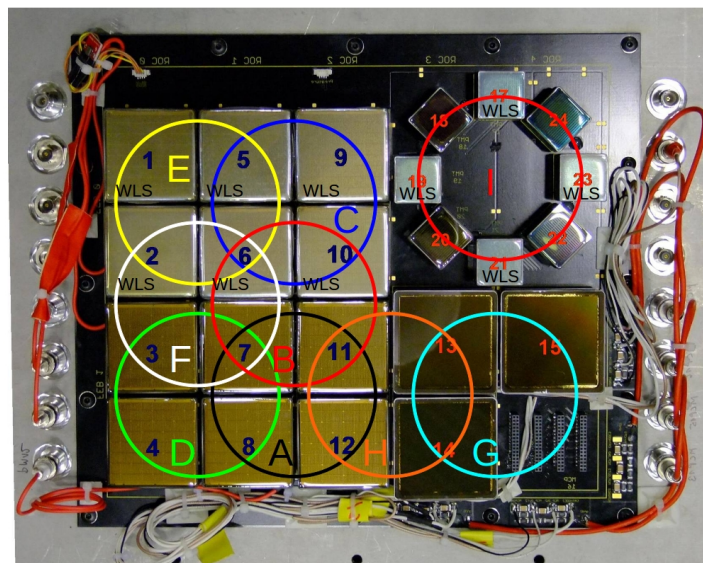


Figure 4.6. – Indicated Cherenkov ring positions on the camera during the beamtest 2012.

Various different runs were taken during the beamtest to cover several aspects of investigation:

Threshold-scan: For the threshold-scan the hardware threshold of the used n-XYter read-out electronics was varied from a value of 25 (in arbitrary units; this value can roughly be converted 1:1 to ADC values), 28, 35, 50, up to a value of 70. The standard hardware threshold used for all other runs was 28.

Two threshold-scans were done, covering runs #126 - #155 (threshold-scan 1) and runs #171 - #196 (threshold-scan 2).

High-Voltage-scan: The high-voltage-scan covers various high-voltages between 900 V and 1100 V for the photomultipliers and between 1600 V and 1900 V for the MCPs with the standard hardware threshold of 28.

The high-voltage scan covers run #97 - #123.

LED-runs: A few runs were taken with the beam switched off and only the light pulser system was generating data. To increase the amount of data the pulserate of the system was

increased. These runs were taken for dedicated crosstalk studies and will mainly be used in the later analyses.

Table 4.3. – Overview of the LED runs taken. Shown are the run number, the used LED and the high-voltage setting (explained in the next chapter).

Run #	201	202	203	204	205	206	207
LED	470 nm	470 nm	275 nm	275 nm	245 nm	245 nm	470 nm
HV	new	old	old	new	new	old	new

An overview of all relevant taken runs during the beamtest 2012 can be found in Appendix A.

Analysis of the CBM beamtest 2012

During the beamtest a lot of data were successfully taken. This chapter will now present different aspects of the analyses, including necessary corrections and basic studies to deduce detailed information of the used sensor candidates with the goal to compare and judge them in view of the requirements in the CBM experiment.

There are several aspects of photomultipliers that are of particular interest and which can be studied with the data taken at the beamtest. One aspect to judge the quality of the sensors are the single-photon spectra, which will be the first study, discussed in Section 5.1. Another very important aspect in the comparison of the different photon sensors is the number of detected photons per Cherenkov ring. The measured number is mainly influenced by the sensor efficiency, but also depends on the individual crosstalk behaviour, the geometrical coverage and the temperature and pressure of the environment. Necessary corrections will be discussed in Section 5.2 and Section 5.3, with an extensive analysis of the crosstalk in Section 5.4 and a comparison of the results in Section 5.5.

5.1 Single-photon spectra

Single-photon spectra are a good tool to judge on the quality of a photomultiplier tube in terms of single-photon counting/detection. A good spectrum is characterised by a pronounced single-photon peak and a clear peak-to-valley distance towards the peak at the low amplitudes of the spectrum. The entries in the spectrum originate either from photons hitting the photocathode and emitting an photoelectron or from single thermal electrons emitted from the photocathode or dynodes. Some of the entries also occur due to crosstalk in the photomultiplier tube, which is mainly generated by charge sharing in neighbouring channels (in the case of multianode tubes).

In addition, the spectrum might also be influenced by the used read-out electronics producing noise in single channels .

From the single-photon spectra several informations and properties of the sensors can be deduced. The position of the single-photon peak is equivalent to the gain. Separated by each pixel this gives access to the gain variation. The character of the single-photon peak, especially the peak-to-valley ratio, shows the quality of the sensor. A clear pronounced single-photon peak simplifies finding an optimal operation threshold, and improves the signal-to-background ratio.

In case of multianode photomultipliers single-photon spectra for each channel can be measured as also a sum spectrum containing all channels. The spectra include all signals with a signal strength above the hardware threshold. In these measurements the effective threshold could be set quite low due to the low electronic noise of the n-XYter, as well as of the connected PMTs, and is nearly negligible in the full ADC spectrum. A proper adjustment of the hardware threshold is of particular importance for the self-triggered n-XYter, since a too low threshold, and thus high trigger rates, could completely spoil the data quality, and cause severe data loss. Thus all detected noise comes mainly from the photomultiplier darknoise.

The 'typical single-photon spectrum of a photomultiplier' has a peak at 0 with an exponential decrease (usually identified as 'pedestal peak') together with a Gaussian-distributed single-photon peak at higher ADC-values and a (mostly) clear pronounced valley in between those two peaks (see also [24]). Depending on several aspects also additional peaks can be visible in the spectrum, e.g. from photoelectrons hitting the second dynode resulting in a lower signal amplitude (this would lead to a peak in between the pedestal peak and the single-photon peak).

The shape of the single-photon spectra and especially the position of the single-photon peak highly depends on the high-voltage of the PMTs and MCPs and the different behaviour can easily be studied. The analyses presented here are based only on the data measured at standard HV, in order to ensure comparable conditions for all sensor candidates. A different hardware threshold doesn't have a strong influence to the spectra as it only affects the cut-off of the spectra at low signal strengths but doesn't change the rest of the spectrum.

5.1.1. Single-photon spectra without corrections

As basis for the following analyses of the single-photon spectra data from run #207 were chosen. In this run only data from the LED (470 nm) was taken, the beam was off. The LED runs are well suited for these analyses as all pixels of the complete camera are nearly homogeneously illuminated and the statistics are therefore high enough (in contrast to beam events, where just a small fraction of the camera is illuminated). For this run a standard hardware threshold of 28 (in arb. units) was used together with optimised high-voltages, which were adjusted after run #125. The reason for this adjustments were the single-photon spectra partially showing single-photon peaks at low ADC values. By increasing the high-voltage of several MAPMTs the single-photon peak was shifted to higher ADC values, matching the values of the other MAPMTs. The corresponding high-voltages can be seen in Table 5.1.

The single-photon sum-spectra of all 23 tested devices in units of ADC amplitude can be seen in Figure 5.1. For an optical separation of the different types dedicated lines were drawn, also for separating the two 8-stage versions of the H8500 and the two devices marked as 'bad' by Hamamatsu.

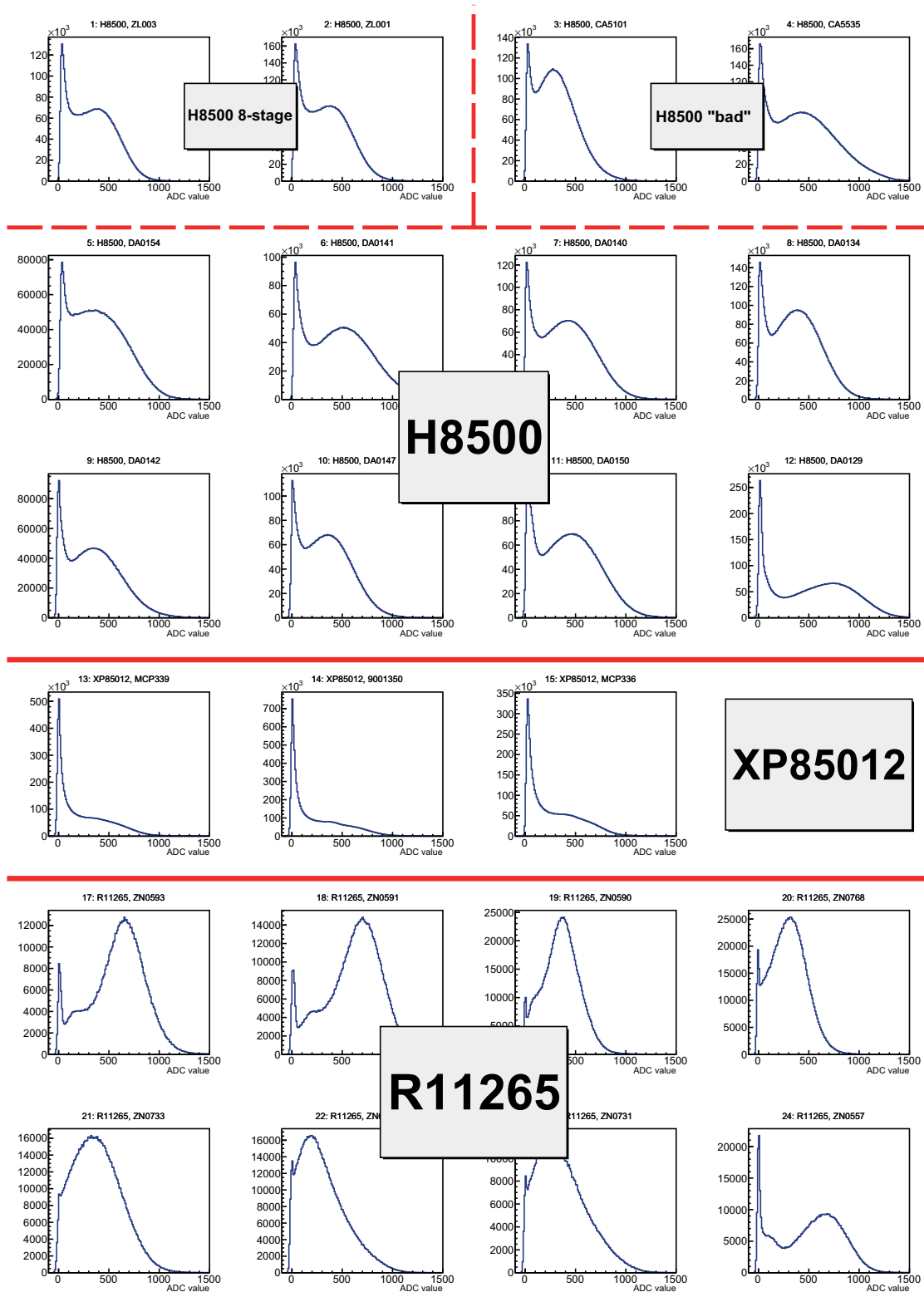


Figure 5.1. – Single-photon sum spectra of all 23 sensors used during the beamtest. The different models are indicated as also some ‘non-standard’ versions of the H8500 PMT are. These spectra only include the data from run #207 without any corrections.

Table 5.1. – Used high-voltages of the PMTs and MCPs during the beamtest. HV_{old} refers to the runs up to #125, HV_{new} to the runs above #125. Some of the high-voltages were optimised based on the single-photon spectra from the LED measurements during the HV-scan (#097 - #123).

PMT	1 – 6	7,8,11,12	9,10	13 – 16	17	18 – 20	21 – 23	24
HV _{new} [V]	1050	1000	1050	1850	950	1000	1050	1000
HV _{old} [V]	1000	1000	1000	1650	900	1000	1050	1000

The different behaviour of the three types is clearly visible. The H8500 PMTs show typical single-photon spectra with a pedestal peak at 0, a Gaussian-distributed single-photon peak at higher ADC-values, and a (mostly) clearly pronounced valley in between those two peaks. The position of the single-photon peak varies as also the peak-to-valley ratio does, but in total all H8500 single-photon spectra look similar. Even the two ‘bad’-marked devices (#3 and #4, in the upper right) show a clearly distinguishable single-photon peak. The two 8-stage versions of the H8500 (#1 and #2, in the upper left) show a worse behaviour with a less pronounced single-photon peak.

In contrast to the relatively good single-photon spectra of the H8500 PMTs the Planacon XP85012 MCPs show much worse spectra as the single-photon peak nearly completely vanishes and the pedestal peak dominates the whole spectra. Due to this strong dominance of the pedestal peak - which mainly contains noise and/or crosstalk hits (dedicated analysis of this pedestal peak are shown later in this chapter) - it is hardly possible to extract a clear single-photon peak position. It also makes it hard to set a threshold with a reasonable signal-to-background ratio (i.e. at least more signal than background entries, but still a high detection efficiency).

A contrary result (to the MCPs) is achieved with the R11265 PMTs: In all spectra the single-photon peak dominates the spectrum and the pedestal peak is either completely (like PMT #21) or at least partially below threshold. For some devices (PMT #17, #18, #24) also a peak below the single-photon peak is visible. This peak occurs when an electron from the cathode hits the second dynode instead of the first one, and therefore gets less amplified but is still being detected.

For a detailed analysis of the single-photon spectra it is necessary that the pixel-to-pixel variations of the ADC-values are corrected by fitting an appropriate function to every single-pixel spectrum. The following function was used for fitting:

$$f(x) = a_1 \cdot \exp\left(-\frac{1}{2} \left(\frac{x - x_0}{\sigma}\right)^2\right) + a_2 \cdot \exp(a_3 \cdot (x - a_4)) \quad (5.1)$$

a_i , x_0 , and σ are the free parameters to fit. This function consists of one Gaussian for the single-photon peak and an exponential distribution for the pedestal peak. It is fitted to the spectra of individual pixel of all the sensors.

Based on these fits the x-axis of the ADC spectra can be normalized to ‘number of photons’ instead of an ADC value, as the position of the Gaussian corresponds to the signal strength caused by a single-photon hitting the PMT. Based on a charge calibration of the full read-out chain, the single-photon peak position can be used to calculate the gain of each pixel and, by averaging, the

mean gain of the PMT. The resulting fits of the single-photon spectra for three exemplary single pixel for all three sensor types can be seen in Figure 5.2, including the complete fitted function as well as the two contributing parts (exponential and Gaussian). The spectrum of the R11265 MAPMT can not be perfectly described, having larger differences at low ADC values due to the lack of this exponential peak in the fitted function. Nevertheless the main single-photon peak is adequately fitted.

All fits are acceptable, mainly resulting in a χ^2/ndf of up to 10 – 15, and in a few cases even higher. Although some fits show larger χ^2/ndf -values, the results are judged as appropriate based on a visual inspection. Mainly important for that is the result of the Gaussian part to be able to extract an accurate value for the single-photon peak position, especially for normalizing the spectra.

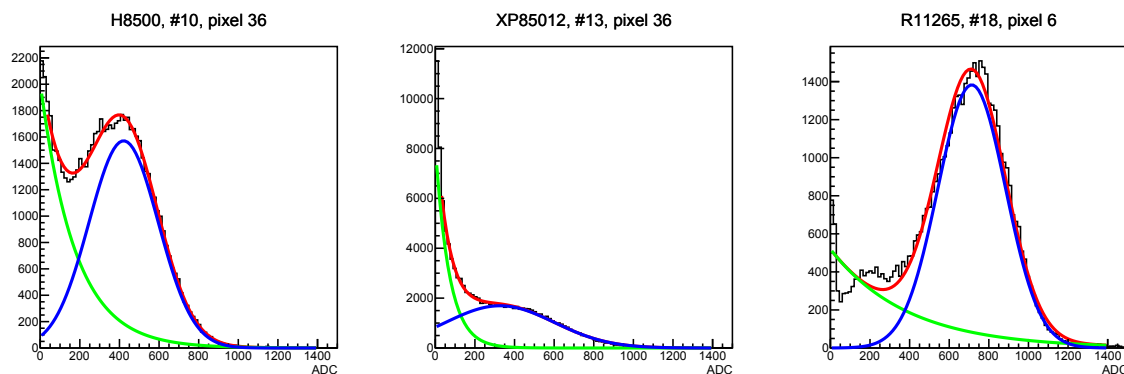


Figure 5.2. – Resulting fit distributions of the single-photon spectra of three single pixel for each sensor (left: H8500, PMT #10, pixel 36, middle: XP85012, PMT #13, pixel 36, right: R11265, PMT #18, pixel 6). Black remarks the data taken, red is the fitted sum functions consisting of an exponential part and a Gaussian and green (exponential) and blue (Gaussian) illustrate the separate parts. Larger differences in the result are visible for the R11265 MAPMT at low ADC values, as the second peak is not included in the fit function.

By comparing the main single-photon peak and the small peak at lower ADC values in the R11265 spectrum, which is caused by photoelectrons hitting the second dynode directly (and thus missing the amplification between the first and second dynode), the dynode gain of the first dynode of this sensor can be estimated. A rough judgement of the peak position from this distribution results in a first dynode gain in the order of 3 – 4, which is comparatively high, explaining the generally well single-photon response of the R11265 PMTs.

With the single-photon peak position it is possible to estimate the gain of each sensor and also of each pixel based on a charge calibration of the complete read-out chain. For our electronics setup, including the various attenuator boards, this has been done in the laboratory, yielding the conversion factors from ADC counts to a charge seen in Table 5.2. The charge can then simply be converted to number of electrons, which is equivalent to the gain of the sensor.

By calculating the gain of each pixel it is possible to estimate the mean gain and also the gain variation of each sensor. The mean gain can then be compared to the data given by the manufacturers (see Table 4.1; remark: the gain values given by Hamamatsu were all measured with a high-voltage of 1000 V).

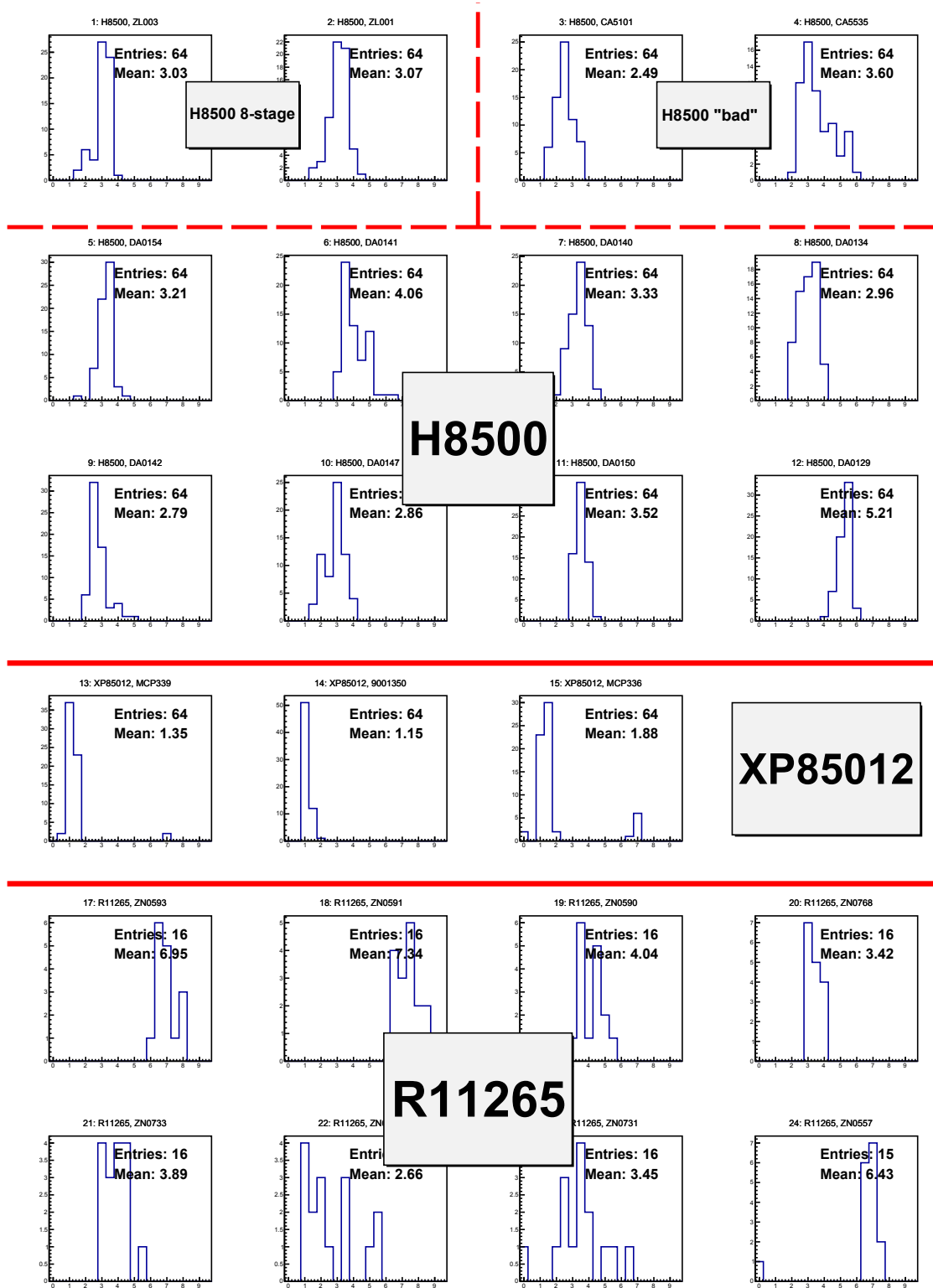


Figure 5.3. – Calculated gain values of all pixel for all sensors (in factors of 10^6).

Table 5.2. – Charge calibration of the used read-out electronics. The resulting conversion factors can be used to calculate the gain of each sensor from the single-photon peak position.

PMT type	Attenuator board	Conversion factor
XP85012	220 pF	1 pC = 1798.9 ADC counts
H8500	470 pF	1 pC = 863.4 ADC counts
R11265	680 pF	1 pC = 600.3 ADC counts

Figure 5.3 shows the absolute gain distributions (in factors of 10^6) for all measured sensors. The given mean value is the arithmetic mean without any fitting of the distributions. Although the absolute numbers differ (in the range of a factor of 2) from the gain values given by the manufacturers, the order of magnitude (10^6) and the tendency among the sensors yield reasonable values. Sensors with a high manufacturer-measured gain show also a high gain within the presented analyses, e.g. PMTs #12 for the H8500 types or #17 and #18 for the R11265 types. However, the gain values provided by Hamamatsu are derived in a completely different way, by illuminating the full photocathode and measuring the anode sum-current. Thus the numbers cannot be directly compared.

5.1.2. Corrected single-photon spectra

The results presented above can be used to correct the single-photon sum-spectra of the sensors for the gain variations between all pixel and to normalize the x-axis of the spectra to ‘number of photons’. A photon number of 1 is then equal to the single-photon peak position (which is the mean-value of the Gaussian part of the fit). Figure 5.4 (blue curves) shows the result of this correction and normalization. This gives a more realistic picture, since later in the experiment, the gain variations from pixel to pixel can be compensated by channel-individual thresholds.

The correction show a slight improvement in the shape of the spectra. The normalization makes it possible to directly compare all sensors, and especially the different sensor types, in terms of single-photon peak width and peak-to-valley ratio.

The H8500 MAPMTs show all very similar corrected spectra with comparable peak widths, except for PMT #5 which is worse also in terms of peak-to-valley ratio. The two sensors marked as ‘bad’ are also very similar to the standard H8500, which illustrate that the delivered sensors at the lower edge of quality still show a good performance, at least in these terms. The two 8-stage versions (H10966) show a slightly worse peak-to-valley ratio, as can be generally expected due to the reduced gain.

The XP85012 MCPs still show relatively bad single-photon spectra, as no dedicated single-photon peak is visible and the whole spectra is still dominated by the low-amplitude peak. As will be seen in following analyses, this low-amplitude peak contains mainly crosstalk hits, i.e. not direct hits from photons, but hits due to e.g. charge sharing in the microchannel plates.

The corrected single-photon spectra of the R11265 MAPMTs show very similar shapes. Judging from these spectra it seems, that there are two ‘quality-types’: those with a very narrow single-photon peak (PMTs #17 - #19) and those with a broader single-photon peak (PMTs #20 - #24). Explanations for this behaviour could not be given. Overall these spectra are very good.

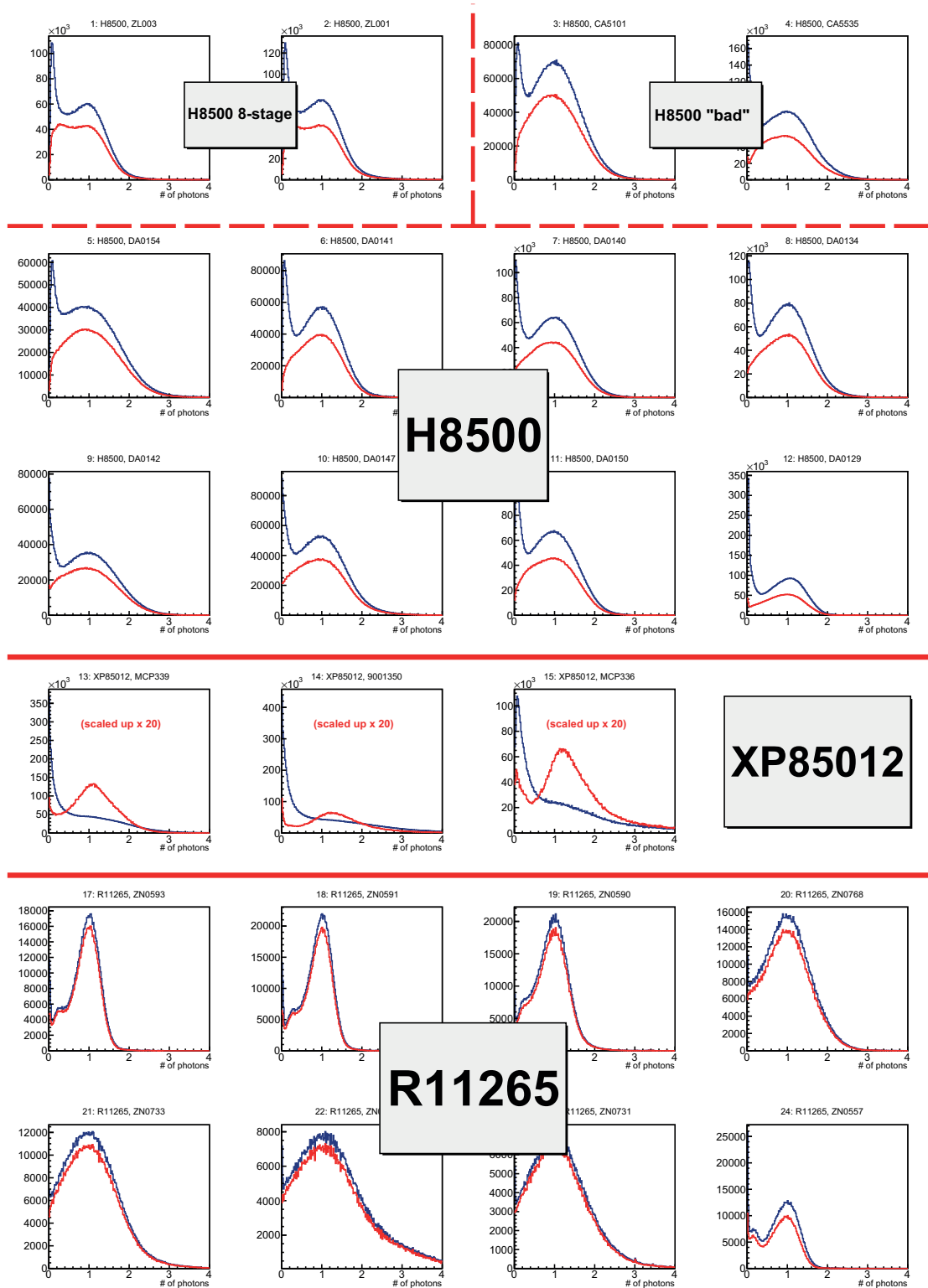


Figure 5.4. – Blue: normalized (to ‘number of photons’) and corrected (for pixel gain variations) single-photon sum-spectra of all 23 tested sensors. Red: resulting spectra only considering amplitude of hits, which do not have a hit in the 8 surrounding pixel. All spectra only include data from run #207.

The red curves in Figure 5.4 show single-photon spectra for a specific case (for the XP85012 MCPs the spectra have been scaled up with a factor of 20 for better visibility of the shape). They only include entries from single hits, which do not have an additional hit in their 8 surrounding pixel (or 5 or 3 surrounding pixel for border and corner pixel, respectively). This selection aims at separating real hits without crosstalk from all entries, although real hits are partially cut away with this selection. It is assumed here, that crosstalk hits occur nearly only in the direct neighbours and to a negligible (one order of magnitude less) fraction in the further away pixel (see e.g. [43], or the Hamamatsu datasheets [44], which only state numbers for the direct neighbours).

Comparing the overall single-photon spectra (in blue) with these reduced spectra (in red) one can see, that this additional cut has a quite different effect on the spectra of different PMT types: clear differences are visible for all H8500 MAPMTs and the XP85012 MCPs, but nearly no differences for the R11265 MAPMTs, neither in shape nor in number of entries. On the one hand these differences are due to less statistics, but the main difference is a change of the shape at very low entries, resulting in a vanishing of the low-amplitude peak for the H8500 MAPMTs or a reduction of this peak for the XP85012 MCPs, respectively.

The influence of this cut can be explained with the assumption that the low-amplitude peak mainly contains crosstalk hits. In addition to this several factors have to be considered here:

- The different sensor types have all different crosstalk properties, especially in the amount of produced crosstalk hits. From our point of know the R11265 MAPMTs produce the least crosstalk hits, whereas the XP85012 MCPs produce a very huge amount.
- The fraction of border and corner pixel is different for H8500 and XP85012 (both with a total of 64 pixel), compared to the R11265 (with a total of 16 pixel). As the main reason for crosstalk is charge sharing within the dynode system, hits detected in those border or corner pixel are expected to produce less crosstalk than pixel in the inner region of the sensor.

Charge-sharing in the dynode system means that a few electrons get into neighbouring dynodes and will be amplified. This leads to a slightly weaker signal in the hit pixel (compared to the case without crosstalk) but also to a signal of low amplitude in the neighbouring pixel. This explanation also supports the conclusion that the pedestal peak mainly contains crosstalk hits.

5.1.3. Summary: Results from the single-photon spectra

From the above presented analyses of the single-photon spectra several results of the different sensors can be deduced.

The uncorrected spectra (i.e. no correction for pixel-to-pixel variations of the gain) already point out the different behaviour of the three different sensor types. The Hamamatsu R11265 MAPMTs show very good spectra with nearly no low-amplitude peak, the H8500 have also good spectra but with a clearly pronounced low-amplitude peak, and the spectra of the Photonis XP85012 MCPs are strongly dominated by the low-amplitude peak and do not show a (visible) separable single-photon peak.

The correction of the pixel-to-pixel gain variations of all sensors and the normalization of the x-axis to 'number of photons' slightly improves the spectra and allows for a better comparability of the different sensor types and also of the various sensors of the same type. The results show

a relatively constant quality of each sensor type, although a few differences are still visible, e.g. slightly varying peak-to-valley ratios of the H8500 MAPMTs or different single-photon peak widths of the R11265 MAPMTs.

The two tested 8-stage versions of the H8500 MAPMT (H10966; PMTs #1, #2) show worse single-photon spectra compared to the standard H8500 type, especially with a less pronounced single-photon peak.

The 'bad' marked H8500 MAPMTs (PMTs #3, #4) show a comparable single-photon spectrum to the standard H8500 ones and therefore indicate a relatively constant production process.

Selecting isolated hits only results in a reduction of the low-amplitude peak for the XP85012 MCPs and nearly a complete removal of this peak for the H8500 MAPMTs, but no big difference for the R11265 MAPMTs. As a conclusion the entries in the low-amplitude peak are judged as crosstalk hits, which are expected to have low signal amplitudes due to the charge-sharing process.

5.2 Correction of the geometrical coverage

As all the sensors have different outer dimensions and were arranged in different ways (different shape and spacing between sensors), the differing geometrical coverages of the Cherenkov rings have to be considered to be able to properly compare the performance of the sensor types in terms of number of registered photon hits per Cherenkov ring. Important to mention is, that only the outer dimensions of the sensors were considered here, and not the active area of the sensors. The correction of the beamtest data for the geometrical coverage is then done to a coverage of 100 %, i.e. no gaps between the sensors. Although the final camera design includes gaps between sensors, this correction is done for better comparability.

For estimation of the individual correction factors, derived from the geometrical coverages, dedicated simulations were done considering the different arrangements. These simulations include exactly the arrangement of the sensors as it was used for the prototype camera, i.e. for each sensor type different properties have to be considered.

1. H8500: Each ring position covers a maximum of 4 devices, with a spacing between the MAPMTs of 2 mm and outer dimensions of each sensor of 52 mm × 52 mm.
2. XP85012: For this ring position only 3 out of 4 devices were available, with a spacing in between of 1 mm and outer dimensions of each sensor of 59 mm × 59 mm.
3. R11265: This ring position only included 8 devices, arranged in a symmetric ring-like shape and with outer dimensions of each sensor of 26 mm × 26 mm.

The exact effective ring coverage for each PMT was derived in the following way:

1. Simulate several rings (here a total of 10^5 rings were simulated). For each ring the ring radius and the exact ring centre are generated randomly with given input values as will be described below. Each ring is divided into a certain number of points (here 36 000, i.e. a step size of 0.01° , equivalent to $\approx 8 \cdot 10^{-3}$ mm for the given ring radii), distributed equidistant on the ring shape.
2. For each point it is checked whether this point lies on a sensor or not.

3. The geometric coverage is calculated as fraction of all points lying on a sensor divided by all simulated points. All values are filled into a histogram to extract a mean value.

As mentioned above, the simulations require several input values, which were all extracted as mean values from fits of the Cherenkov ring radius and position in the obtained beamtest datasets, and which are necessary to achieve realistic results. As basis the runs from the second threshold-scan were used (runs #176 - #181), all with the standard hardware threshold of 28 a.u. and at a beam energy of 4 GeV/c. The runs cover the ring positions A, B, D, E (all H8500), G (XP85012), and I (R11265). For each sensor type a dedicated simulation was done to cover the slightly different results of ring radius and center (although the differences can nearly be neglected) due to minimal variations of the radiator length towards the different positions and not perfectly aligned mirror settings.

Ring radius: The ring radius is Gaussian distributed with mean radii of $r_{\text{H8500}} = 45.8$ mm and a width of $\sigma_{r, \text{H8500}} = 0.7$ mm, $r_{\text{R11265}} = 45.3$ mm and a width of $\sigma_{r, \text{R11265}} = 0.7$ mm, and $r_{\text{XP85012}} = 45.6$ mm and a width of $\sigma_{r, \text{XP85012}} = 1.4$ mm, respectively. For the radius of the H8500 type the mean value of the positions A, B, D, and E was taken and an upper limit of their widths.

Ring center: The ring center is Gaussian distributed in x- and y-direction. The mean value of this distribution is not centered between the sensors (this would be the ideal ring position) what has also been considered in the simulations. This leads to a small offset of the simulated ring position towards the ideally centered position. The values for the offset in x-direction d_x and in y-direction d_y and the corresponding widths σ_{d_x} and σ_{d_y} can be found in Table 5.3.

Table 5.3. – Ring centers and widths used for the simulations of the geometrical coverages. The values were extracted from the beamtest data. In case of the H8500 sensor the center positions are the mean value of the four considered positions and the width is the upper limit.

Sensor type	d_x in mm	σ_{d_x} in mm	d_y in mm	σ_{d_y} in mm
H8500	3.0	3.2	2.0	2.6
R11265	0.3	3.3	0.0	2.7
XP85012	-0.6	2.1	1.2	3.2

As the direction of the shift (\rightarrow algebraic sign) does not matter for the simulations due to the discrete symmetric behaviour, the positive values of the positions with H8500 MAPMTs were used.

In Figure 5.5 the center distributions for different positions from the beamtest data can be seen, the red lines indicating the outer borders of the sensors.

The results for the geometrical coverages for each sensor type can be seen in Figure 5.6 and are summarized in Table 5.4. Figure 5.7 gives a crosscheck of the simulations by drawing all hits, which lie on one of the sensors. Especially for the H8500 it is visible that some of the rings (with big ring radii) are bigger than four sensors. But this is only a low fraction and should be negligible for the full prototype camera.

Another interesting thing to look at is the geometrical coverage in dependence on the ring center as can be seen in Figure 5.8. The different sensor arrangements result here in different behaviours

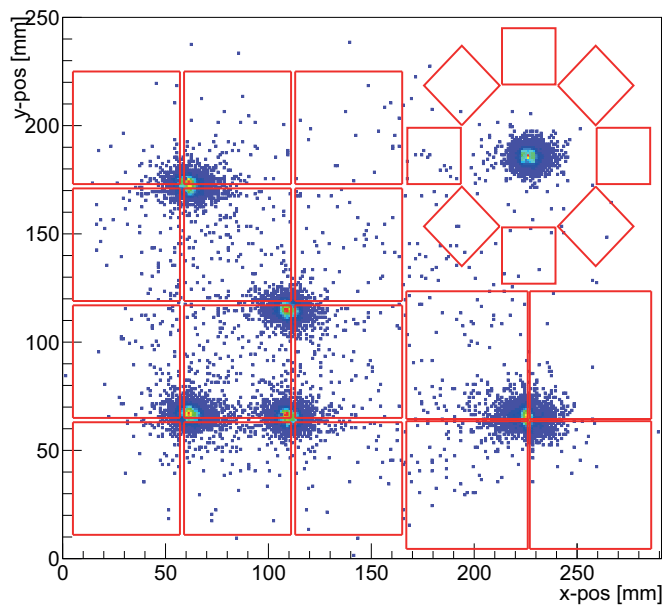


Figure 5.5. – Distributions of ring centers from the circle fit. Basis is the beamtest data (threshold scan 2), runs #176 - #181. Shown are ring positions A, B, D, E, G, and I.

in dependence on the ring centre position. The shape for the R11265 MAPMT (mid) can simply be explained by the ring-like and symmetric arrangement of the sensors. For the H8500 MAPMTs it first looks like very asymmetric results, but this is due to the offset of the ring centre position (positive values in both directions). Otherwise the results show a very constant ring coverage for a wide range of x - and y -displacements and a small decrease for a displacement in one direction for displacements > 7 mm, as parts of the ring are outside of the MAPMTs in that case. The results for the XP85012 can also be explained. On the one hand the shape does not look like for the H8500 because of their larger outer dimensions of 59 mm (in comparison to 52 mm for the H8500), thus all simulated rings lie completely on the sensors. The missing coverage in the lower right corner is due to the fact, that only 3 MCPs were available for the beamtime.

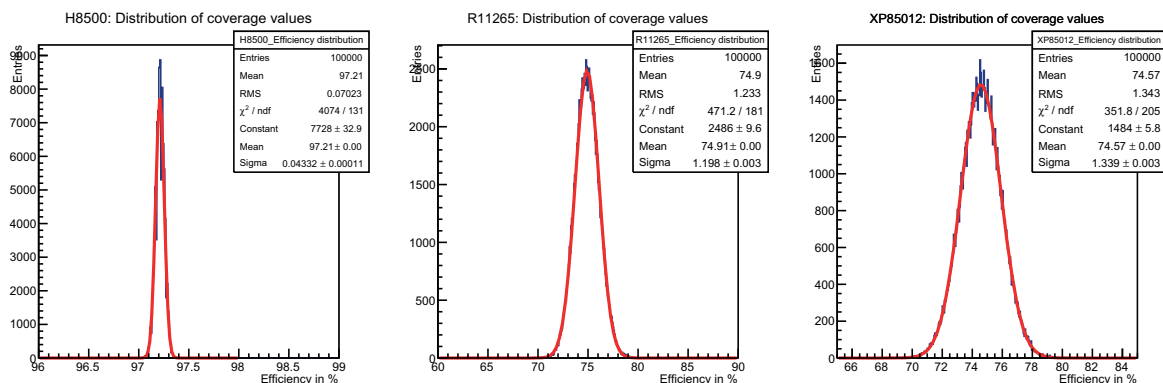


Figure 5.6. – Resulting coverage distributions of the different arrangements (left: H8500, mid: R11265, right: XP85012). Each distributions has been fitted with a Gaussian.

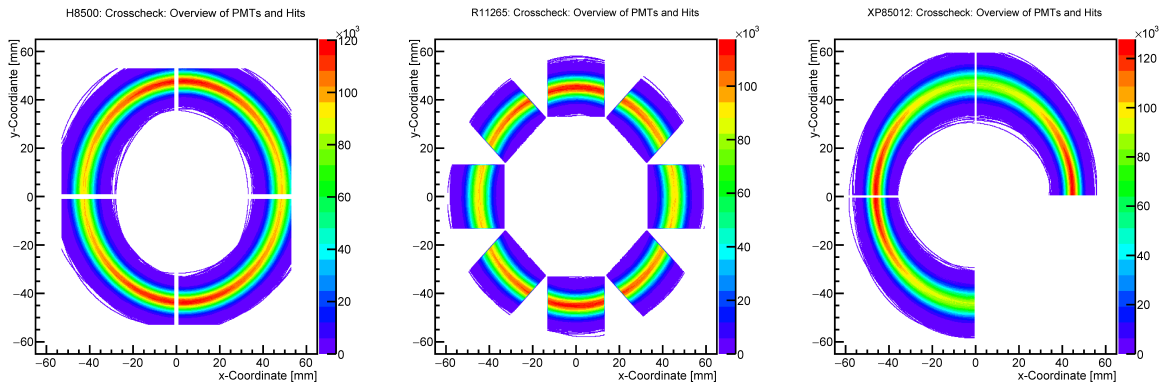


Figure 5.7. – As a crosscheck of the simulations all points lying on a sensor have been drawn (this excludes points in between two sensors and beneath the sensors) (left: H8500, mid: R11265, right: XP85012). The different behaviour in the ring mean range (i.e. the red colored area) is a result of the squared binning of the histograms.

Table 5.4. – Results from the fits of Figure 5.6 given as mean geometrical coverage and width of the distribution. Due to the high statistics errors of the fit are very small and not relevant here.

PMT type	H8500 in %	XP85012 in %	R11265 in %
Mean coverage	97.21	74.57	74.91
Width	0.04	1.34	1.20

The mean coverage values from Table 5.4 were used in the later analysis as a correction factor to compare the efficiencies of the different sensor types.

5.3 Correction of temperature and pressure

The measured number of photons per Cherenkov ring, as well as the ring radius, are influenced by the varying atmospheric conditions prevailing at the test site at CERN. An adequate correction of this influence is done by considering the theoretical correlation between those parameters and deriving a correction factor from that. The corrections are always done towards standard conditions, i.e. a pressure of $p_0 = 1000$ mbar and a temperature of $T_0 = 0^\circ\text{C} = 273.15$ K, which are also the common standard conditions used in all CBM simulations.

Correction of the ring radius for temperature and pressure

For the ring radius the necessary correction can easily be done by approximating the theoretical formula. With $r = f \cdot \tan \theta_C$, $\cos \theta_C = \frac{1}{\beta n}$, and $n - 1 = (n_0 - 1) \cdot \frac{p}{p_0} \cdot \frac{T_0}{T}$ the following can be derived with the assumption of $\tan \theta_C \approx \theta_C$ [rad] for small Cherenkov angles θ_C (as it is given for

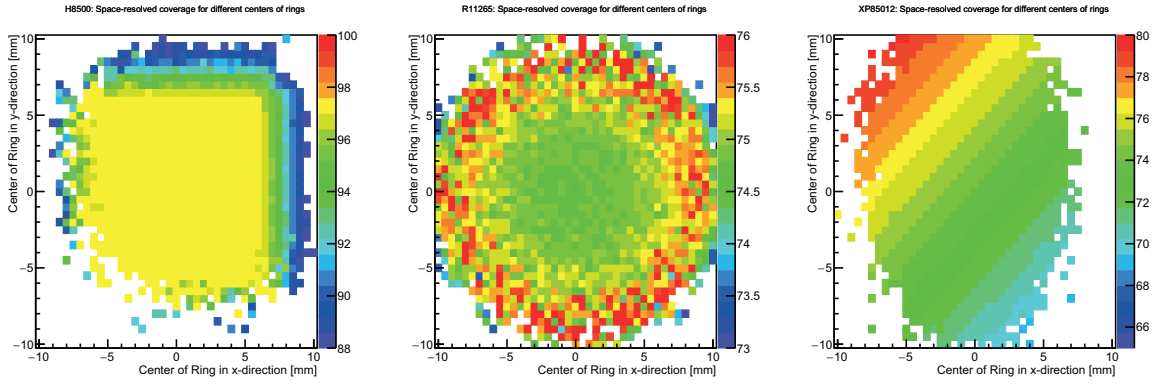


Figure 5.8. – Geometrical coverage as function of the simulated ring center (left: H8500, mid: R11265, right: XP85012). The different behaviour of the arrangements can clearly be recognized.

CO₂ with $\theta_C \approx 1.72^\circ$) and the series expansion $\arccos x = \frac{\pi}{2} - x + \frac{1}{2} \frac{x^3}{3} + \dots$:

$$\begin{aligned}
 r &= f \cdot \tan \theta_C \\
 &= f \cdot \tan \left(\arccos \frac{1}{\beta n} \right) \\
 &\approx f \cdot \left(\frac{\pi}{2} - \frac{1}{\beta n} \right) \\
 &\approx f \cdot \left(\frac{\pi}{2} - \frac{T}{p \beta} \right) \tag{5.2}
 \end{aligned}$$

Here r is the Cherenkov ring radius, f the focal length of the mirror, θ_C the Cherenkov angle, and n the refraction index of the radiator.

From this approximation we get a correction factor of $\frac{\pi}{2} - \frac{T}{p}$ for electrons ($\beta = 1$). As a reference for temperature T_0 and pressure p_0 the values commonly used in the CBM simulations have been taken here, i.e. a temperature of $T_0 = 0^\circ\text{C} = 273.15\text{ K}$ and a pressure of $p_0 = 1000\text{ mbar}$.

To prove the performance of this correction, ring radii extracted from several beamtest runs are compared to simulations. Simulations give a mean radius of 46.7 mm with a width of $\sigma_r = 0.6\text{ mm}$ for a beam energy of 3 GeV/c ([27, p. 135]). From data a total of 33 different runs for position A (as this is the reference position, which was regularly used for reference measurements) were taken (runs no. 54, 64, 71, 73, 81, 92, 95, 97, 103, 107, 112, 117, 121, 126, 131, 138, 144, 152, 170, 171, 176, 182, 187, 192, 197, 322, 324, 326, 329, 332, 335, 343, 346) and each time the mean fitted ring radius is extrapolated to the reference conditions, which were also used in the simulations. A comparison of these extrapolated to the simulated values under the same pressure and temperature conditions can be seen in Figure 5.9. It is clearly visible that the applied corrections reduce the variations of the ring radius of all the runs and shift the radii to slightly larger values, and especially that the corrected results are closer to the simulated value as the uncorrected ones.

The considered runs cover different properties like beam energies between 3 GeV/c and 8 GeV/c, various high-voltages of the MAPMTs (900 V – 1100 V), several hardware thresholds (25 – 70 in arbitrary units), and also runs with a high contamination of the CO₂ radiator with water and oxygen.

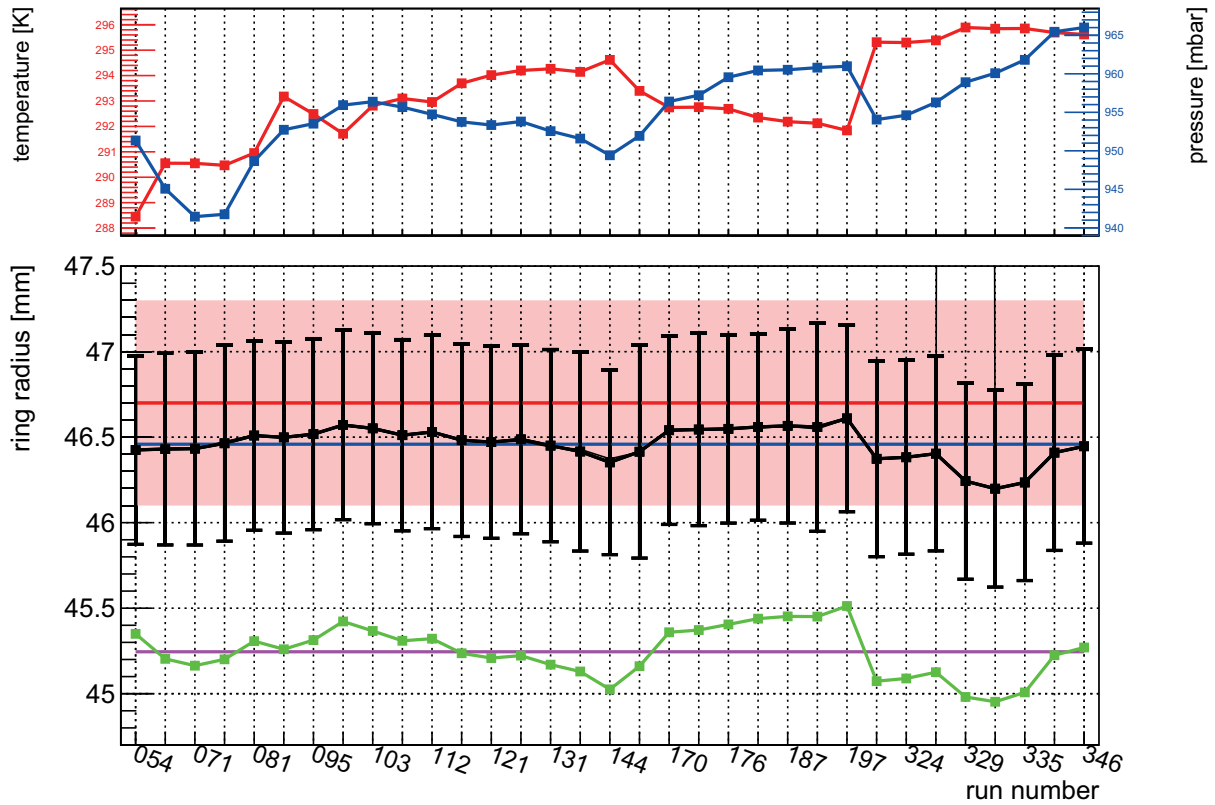


Figure 5.9. – Bottom: Mean ring radius for Position A for 33 different runs (black) covering a time period of roughly 12 days. The error bars mark the widths of the radius distribution (Gaussian shaped) of each run. In blue the mean value of all 33 ring radius distribution-means from these runs is shown ($\approx 46.46 \text{ mm} \pm 0.02 \text{ mm}_{\text{RMS}}$), and in red the mean value and distribution width from simulations ($r_{\text{mean, sim}} \approx 46.7 \text{ mm}$, $\sigma_{r, \text{mean, sim}} \approx 0.6 \text{ mm}$). Additionally in green the uncorrected values from the runs are plotted with the mean of the uncorrected data in purple. For readability only every second run number is given. Top: Corresponding temperatures (red) and pressures (blue) inside the RICH prototype.

From these 33 runs a mean ring radius of $\approx 46.46 \text{ mm}$ can be estimated, with a standard deviation of the mean value of $\sigma \approx 0.02 \text{ mm}_{\text{RMS}}$. This corrected value is very close to the simulated one ($46.7 \text{ mm} \rightarrow \sim 0.2 \text{ mm} \approx 0.4\% \text{ deviation}$), much better compared to the uncorrected value ($45.2 \text{ mm} \rightarrow \sim 1.2 \text{ mm} \approx 2.5\% \text{ deviation}$). Also the variations of the single-values around the mean decrease with the corrections, representing the good quality of the correction.

Most of the runs were taken at a beam energy of $3 \text{ GeV}/c$ (runs #54 - #121 and #322 - #346), a few with $4 \text{ GeV}/c$ (threshold scan 2, runs #170 - #197), and $8 \text{ GeV}/c$ (threshold scan 1, runs #126 - #152). As electrons are ultrarelativistic already at the lowest beam energies no variation in the ring radius as function of the beam energy is expected, in agreement with the measurements. Larger deviations of the corrected ring radius only occur at the last runs (from #322 on) and might be caused by several electronics tests (including changing parts of the electronics). The influence of the high-voltage and the hardware threshold on the ring radius should be comparable in case there is an effect. An increased high-voltage should therefore show similar results to decreasing the hardware threshold as both properties mainly influence the distribution of detected signal amplitudes and the amount of additional crosstalk-hits being detected.

After the second threshold scan, i.e. from run #322 on, the ring radius slightly drops. A similar drop also occurs in the temperature and pressure trend. The correction of the ring radius for temperature and pressure softens this drop but cannot eliminate it completely. An obvious reason for this behaviour is not known, but it might be caused by a reset of the electronics with a slightly different re-initialization, causing a baseline shift, and thus changing the effective threshold.

Correction of the ring hit multiplicity for temperature and pressure

The number of detected photons N per Cherenkov ring for an specific RICH detector can be described via

$$N = N_0 \cdot L \cdot \sin^2 \theta_c \quad (5.3)$$

with L the radiator length and θ_c the Cherenkov angle ([45]). N_0 is a performance parameter depending on the specific parameters (radiator absorption, mirror reflectivity, photon detector efficiency) of the RICH detector and is therefore a fixed value.

By using $\sin^2 x + \cos^2 x = 1$ and $n - 1 = (n_0 - 1) \cdot \frac{p}{p_0} \cdot \frac{T_0}{T}$ one can calculate

$$\begin{aligned} N &= N_0 \cdot L \cdot \sin^2 \theta_c \\ &= N_0 \cdot L \cdot (1 - \cos^2 \theta_c) \\ &= N_0 \cdot L \cdot \left(1 - \left(\frac{1}{\beta n}\right)^2\right) \\ &= N_0 \cdot L \cdot \left(1 - \frac{1}{\beta^2} \cdot \frac{1}{\left(1 + (n_0 - 1) \cdot \frac{p}{p_0} \cdot \frac{T_0}{T}\right)^2}\right) \end{aligned} \quad (5.4)$$

Here $n_0 = 1.00045$ is the refractive index of CO_2 at $\lambda = 600\text{nm}$ and standard conditions, i.e. $p_0 = 1000\text{mbar}$ and $T_0 = 273.15\text{K}$. For electron rings $\beta = 1$ is assumed resulting in an (analytic) correction factor of $1 - \left(1 + (n_0 - 1) \cdot \frac{p}{p_0} \cdot \frac{T_0}{T}\right)^{-2}$. Additionally an approximation can be derived with $n_{\text{CO}_2} \approx 1.00045 \approx 1$ leading to a simple linear dependence $N \sim \frac{p}{T}$.

The results of these corrections can be seen in Figure 5.10 showing the analytical and the linear correction applied to the mean value and to each single event.

Using a linear correction gives a very good approximation of the ring hit multiplicity as the results are nearly identical to the analytical correction independent of correcting each single event or the mean value of all summed up events afterwards. The differences in both corrections are below 0.01 % with only 3 points of higher deviations for the event-wise correction which are also visible in Figure 5.10 (blue and red line). But there is a clear absolute difference of around 0.6 hits per ring (with maximum difference of 1 hit per ring) visible when applying the corrections event-wise or on the mean value. This small discrepancy occurs to be very constant and can be included as an offset in the analyses.

The behaviour of the hit multiplicity between run #126 and #197 is caused by two consecutive threshold scans, the first from run #126 to #152 with thresholds 25 - 28 - 35 - 50 - 70, and the second scan including runs #170 to #197 with thresholds 28 - 25 - 28 - 35 - 50 - 70 - 28. Increasing

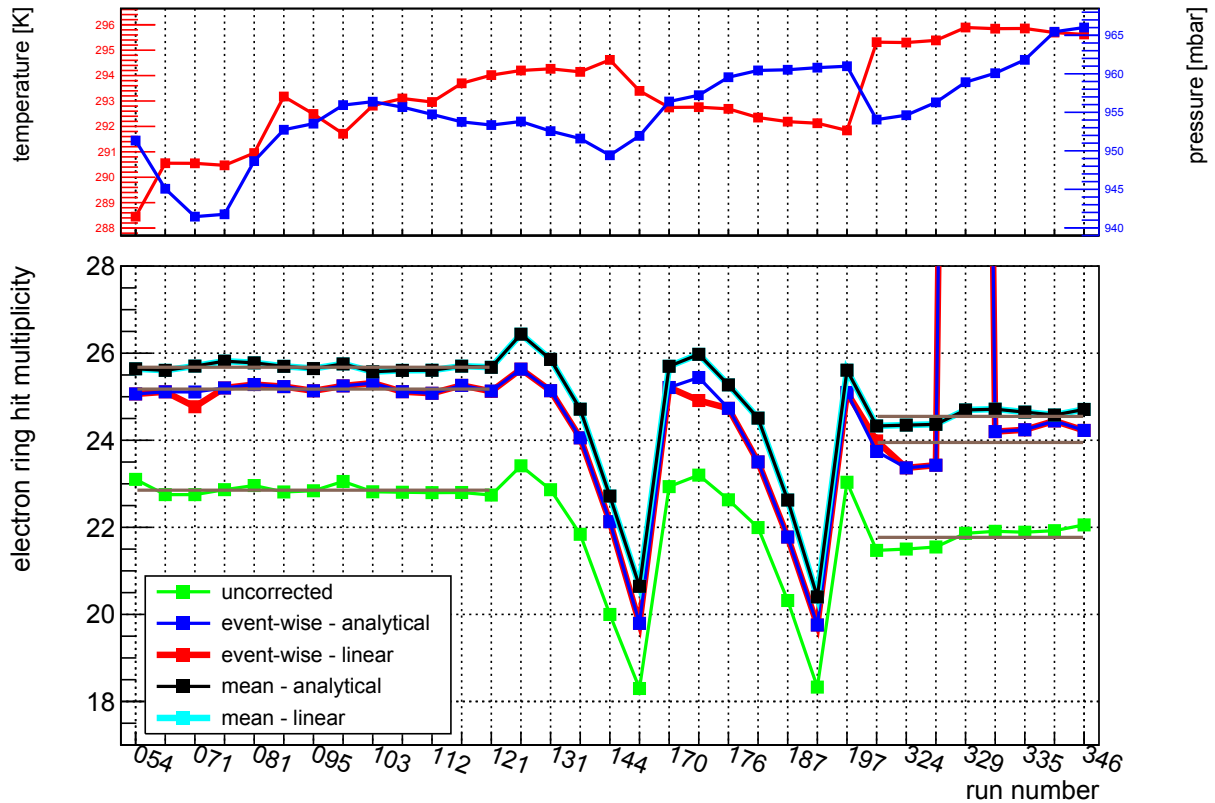


Figure 5.10. – Bottom: Mean electron ring hit multiplicities for Position A for 33 different runs (black) covering a time period of roughly 12 days. The error bars mark the widths of the radius distribution (Gaussian shaped) of each run. In blue the mean value of all 33 ring radius distribution-means from these runs is shown ($\approx 46.43 \text{ mm} \pm 0.02 \text{ mm}_{\text{RMS}}$), and in red the mean value and distribution width from simulations ($r_{\text{mean, sim}} \approx 46.7 \text{ mm}$, $\sigma_{r, \text{mean, sim}} \approx 0.6 \text{ mm}$). Additionally in green the uncorrected values from the runs are plotted with the mean of the uncorrected data in purple. For readability only every second run number is given. Top: Corresponding temperatures (red) and pressures (blue) inside the RICH prototype.

the threshold lowers the mean number of detected hits per ring as more and more hits are going undetected due to an amplitude below threshold.

From run #322 on (i.e. after the threshold scans) an overall (constant) drop in hit multiplicity occurs, correlated with the drop in the ring radius seen in Figure 5.9. The important runs considered for further analyses are the runs up to the second threshold scan, hence this drop is not relevant for the presented analyses.

Whether the correction on ring radius and hit multiplicity are applied to individual events, or to the average values over many events, does not make a significant difference. For simplicity, the corrections were therefore applied on the mean values.

5.4 Crosstalk Estimation

Crosstalk is a phenomenon of multi-pixel photon detectors, like MAPMTs or MCPs, and sums up all effects leading to additionally registered hits ('crosstalk hits') from one real hit due to charge sharing in neighbouring dynodes/pixel or due to capacitance coupling effects. As a result one incoming photon produces a signal in two or even more pixel. In order to compare the different sensor types in terms of efficiency or hit multiplicity, it is important to correct for the different amount of crosstalk in the hit samples, since these crosstalk hits do not add any significant information, and do not contribute to the photon multiplicity per Cherenkov ring. Thus 'crosstalk' is the probability to detect an additional hit in one of the surrounding pixel of the originally hit, which is not caused by a second incoming photon.

Crosstalk can be used (and might even be intentionally implemented) to increase the spatial resolution of the sensor by weighting the signal amplitudes in the different pixel. However, this is only possible to a certain degree and requires a low hit density on the sensor. In the CBM-RICH detector the hit density, especially in the inner region of the camera, is quite high and therefore a high amount of crosstalk is not acceptable as a large number of additional crosstalk hits would have a negative effect on the ring detection and reconstruction efficiency.

The analysis of the beamtest data includes fits of each Cherenkov ring with access to all relevant parameters, amongst them the ring hit multiplicity, which is important for the further analyses. This ring hit multiplicity strongly depends on the sensor type and includes real hits as well as crosstalk hits, but it is not possible to distinguish between real and crosstalk hits on an individual hit basis. Only the number of detected real hits is important for the comparison of the sensors as this reflects the detection efficiency of the sensors. Therefore a statistical method had to be developed to estimate the fraction of detected crosstalk hits to be able to correct the measured average ring hit multiplicity.

In a previous work ([27]) a first approach for crosstalk estimation had been developed for the data of the 2011 beamtest. This method is based on selected events from the LED data (see Section 4.2), in which one sensor registered exactly two hits, and compares the distribution of distances of these two hits with simulations. These 2-hit-events are caused in two different ways:

- The two hits are caused by two real photons being registered by the sensor. No crosstalk hit is produced. The individual hit positions on the sensor are randomly distributed.
- One of the two hits is caused via a photon, the second hit is caused by the crosstalk from the (usually nearby) first real photon hit. Thus the positions of the hits on the sensor are correlated and not randomly distributed anymore.

It is also possible to adapt this method for events with more than two hits per sensor, but this would strongly complicate the analysis as the number of possibilities, how an event can be generated, increases (e.g. for 3-hit-events we can have one, two, or three photons together with two, or one, or zero crosstalk hits). Each event has to include at least one real photon hit as this is the requirement for the production of crosstalk.

The crosstalk is extracted from this data by comparing the distribution of distances of these two registered hits (calculated as distance between mid-points of the two participating pixel in units

of pixel, i.e. horizontal and vertical neighbours have a distance of 1, and diagonal neighbours have a distance of $\sqrt{2} \approx 1.4$, and so on) with a simulated distance distribution.

The simulated distance distribution is generated by randomly placing two hits on the 8×8 (or 4×4 for the R11265 MAPMTs) pixel matrix. As these two hits are uncorrelated, this simulation is equivalent to events without any crosstalk hits but only two real photon hits. The simulated distance distribution matches the experimentally derived distribution very well as shown in Figure 5.11. Only in the bin corresponding to both hits in neighbouring pixel (i.e. at a distance of 1 (horizontal/vertical) or 1.4 (diagonal); both are included in the first bin), a significant excess is seen in the experimental data. This excess is caused by the additional crosstalk hits (and also indicates, that crosstalk hits are only produced in direct neighbour pixel). The fraction of crosstalk is extracted as the number of hits within this excess (\equiv crosstalk hits) divided by the number of real hits (all hits except the crosstalk hits). To ensure comparable number of entries the simulations are scaled to the data based on the number of entries for distances ≥ 2 (i.e. all bins except the first one containing crosstalk hits).

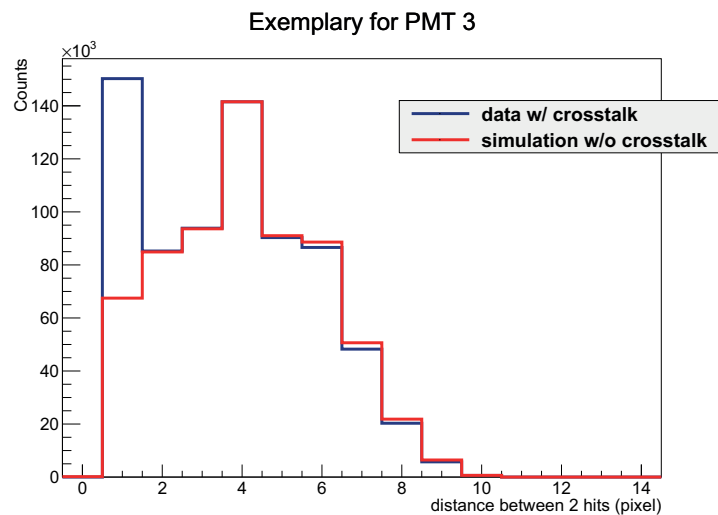


Figure 5.11. – Exemplary distance distribution for events containing exactly two hits, simulation (red) and data (blue). The simulation fits nearly perfectly in all bins except the first bin. This excess in the first bin can be explained by the amount of crosstalk (usually appearing in neighbouring pixel, i.e. at a distance of 1 or 1.4) in the data.

This method was applied in the analysis of the 2011 data, where it gave quite reasonable results. However, the normalization to the total number of 2-hit-events, and thus the extraction of the crosstalk result, slightly depends on the absolute illumination intensity, or the fraction of real 2-photon events with respect to crosstalk induced 2-photon events. As long as the fraction of crosstalk induced events is small, the dependence is small and can be neglected. This was the case in the 2011 beamtest. In 2012 however, the illumination was much weaker, causing a significantly larger fraction of crosstalk induced 2-photon events in the data sample.

The influence of the absolute illumination intensity (or the fraction of two-photon hits and one-photon + crosstalk hits) on the crosstalk results with the above presented method can clearly be seen by simulating the distance distributions for many different illumination distributions and applying the above described method of crosstalk estimation. The illumination intensity, in terms

of number of produced photons, is Poisson-distributed with the only relevant factor being the mean value of this distribution. These simulations were done the following way:

1. Choose the mean number of the illumination distribution. Leave this mean value fixed and repeat the following steps for a large number of loops. Each loop represents one event.
2. For each loop/event choose a Poisson-distributed number of photons (with the above chosen mean value).
3. For each photon in this event generate an uniformly-distributed position on the PMT and a crosstalk hit with fixed probability in one of the neighbouring pixel. The exact probability for generation of crosstalk was set at the beginning of the simulation.
4. Fill a histogram with the total number of hits in this event (i.e. real photon hits and crosstalk hits).
5. Select only events with a total of two hits (i.e. either two real hits or one real hit and one crosstalk hit) and calculate the distance between these two hits.
6. Fill histogram with calculated distance.
7. After simulating a certain amount of events, apply the above presented method of crosstalk estimation for this simulation.

As the results also depend on the input crosstalk amount (in step 3), several simulations were done for different fixed input crosstalk amounts (5 %, 10 %, 15 %, 20 %, 25 %, 30 %) and for a wide range of illumination mean values (between 0 and 12 with a stepsize of 0.2). The results of this Monte Carlo test is seen in Figure 5.12, with the mean number of the illumination distribution on the x-axis and the calculated crosstalk amount on the y-axis. For clarification horizontal lines were drawn to indicate the value for the input crosstalk belonging to each graph.

If the method would work as initially expected, the resulting graphs would be flat, pointing to the correct 'calculated crosstalk value', independent of illumination. However, they are not flat, but show an exponential-like relation between the absolute illumination intensity and the resulting crosstalk value, like it is expected following the above explanation as the fraction of single-photon + crosstalk hits significantly decreases with increasing illumination and thus has a significant influence on the crosstalk results.

5.4.1. Data based method for crosstalk estimation

The 2012 beamtest allowed for the first time for an adequate comparison of different PMTs (with different crosstalk amounts) under realistic conditions. Therefore a reliable method for crosstalk extraction was needed and could not be provided using the same method as for the 2011 beamtest. Hence, an improved method was developed for the 2012 beamtest considering the specific requirements mentioned before, i.e. to consider the absolute illumination intensity for calculation of the crosstalk. As mentioned above the term 'crosstalk' always describes the probability to detect an additional hit in one of the surrounding pixel of the originally hit pixel, not stemming from a direct photon hit.

This new method for estimating the crosstalk works the following way: simulations are done to generate several distributions for the illumination intensity (which is Poisson-distributed) and the

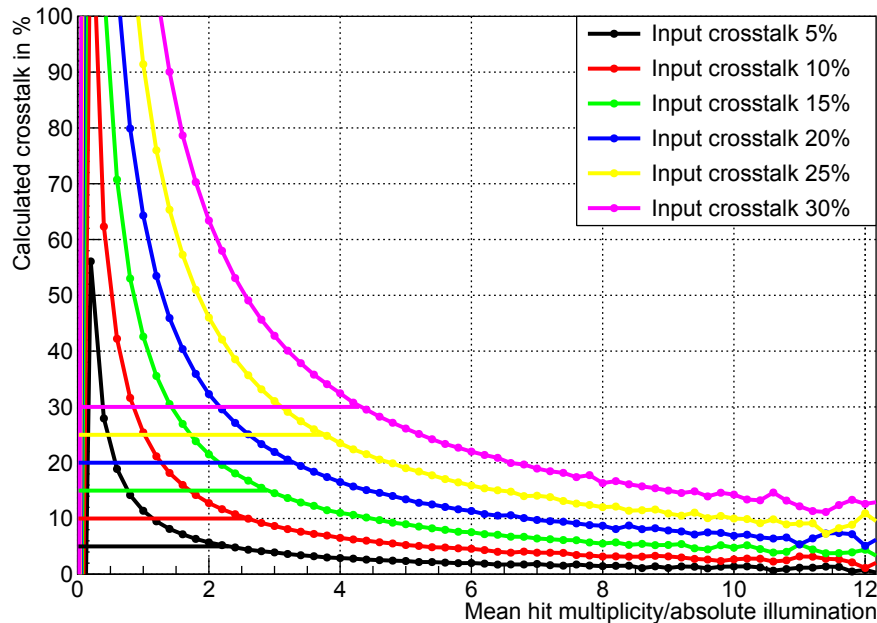


Figure 5.12. – Simulation of the behaviour of the old method of crosstalk calculation for different absolute illumination values and fixed input crosstalk values. Several simulations were done each with a fixed amount of crosstalk between 5% and 30%. Horizontal lines are additionally drawn (uo to the point, where the calculated crosstalk matches the input crosstalk) to indicate the input crosstalk value for each result.

distance of two hits on the sensor for two-hit events only based on two specific input parameters for the crosstalk amount and the mean value of the illumination distribution. In the end a large set of distributions for several crosstalk amounts and illumination mean values are available.

In the next step the distributions from the beamtest data are derived. Generating the distribution for the illumination intensity is done by counting the number of detected hits for each event, separately for each sensor. The distance distribution (distances of two hits on the sensor for two-hit events) is created as described before.

Afterwards, each simulated pair of distributions is first scaled to the distributions from data by minimizing the sum of differences of each bin (using the `BrentMinimizer1D` class of ROOT, documented in [46]), and then both are compared based on a χ^2 -test. The pair of simulated distributions with the smallest sum of the two χ^2 -values (one for each histogram) is then supposed as best matching the data and the according input values for this pair is accepted as representing the crosstalk properties of the sensor.

In more detail the procedure was applied in the following manner:

1. Choose a Poisson-distributed number of photon hits for a specific mean value of the underlying Poisson-distribution.
2. Place each photon hit into a randomly chosen sensor pixel. For each hit generate potential crosstalk hits in the neighbouring pixel for a given probability.

3. Count all hits in this event (photon hits plus crosstalk hits) and fill a histogram with this value. Double hits in a single pixel (two photon hits, or photon hit plus crosstalk hit from a neighbouring pixel) are counted once only.
4. If the overall number of hits in this event is equal to two, calculate the distance between these two hits and fill a histogram with this value.
5. Repeat this procedure to get enough statistics.
6. Repeat steps 1-5 for several values of the Poisson-mean (from step 1) and of the crosstalk probability (from step 2).

Based on these simulations the two distributions from data are compared to the simulations. In an ideal case the simulated distributions should perfectly match the data, but due to partially low statistics in the data or a non-Poisson-like behaviour smaller deviations can occur.

All simulated pairs of distributions are generated from 10 000 000 events, with a stepsize of 0.1 for the input illumination mean value, and a stepsize for the input crosstalk value for the MAPMTs of 0.1 % and for the MCPs of 0.5 %. The reason for the different stepsize is the strongly increased effort (and therefore time) which is needed to simulate higher amounts of crosstalk (which is necessary as the MCPs show much more crosstalk). Due to the differing fraction of 2-hit-events the number of entries of the distance distribution also varies. Separate sets of distributions for each PMT type were simulated to cover the different requirements (only 16 pixel of the R11265 MAPMT, and much higher crosstalk of the XP85012 MCP), but all with the same underlying algorithm to create them.

From the comparison of all simulated distributions and the data taken, two distributions of the χ^2 -values (for the distance distributions and for the illumination intensity distribution) can be generated as exemplary shown in Figure 5.13 for PMT #1. The extracted minimum values for the crosstalk and the illumination are marked by the black lines (here: crosstalk 10.6 %, illumination mean 1.5).

There are clear structures visible in both distributions. For the distance distribution the lowest χ^2 values form a curve similar to a low-order polynomial function, whereas for the illumination distribution this forms nearly a linear or constant curve. From these two different characteristics it should therefore be possible to extract clear values for the best fitting simulations from the sum of both distributions.

For each PMT the measured distributions for the absolute illumination and for the distances of 2 hits on the PMT were extracted from run #207 (LED-run; extra taken for these analyses; the applied high-voltages of the sensor is the typical voltage, at which the sensors are expected to perform optimal) and compared to the simulated distributions. Run #207 was taken with regard to these analyses with increased statistics of the LED data. A summary of the extracted crosstalk and mean illumination values can be seen in Table 5.5 and in Figure 5.14, together with results from the 2011 beamtest for a few sensors (in black).

The results resemble the expectations, that the H8500 MAPMTs produce a decent amount of crosstalk (typically in the range of 8 % – 16 %), the R11265 produce nearly no crosstalk (typically up to 2 %), and the XP85012 MCPs produce quite a lot of additional crosstalk hits (in the order of 80 %). The results for each sensor of the same type are very similar, already indicating the reliability of this new method for crosstalk estimation. Only two sensors (PMT #12 and #24) show

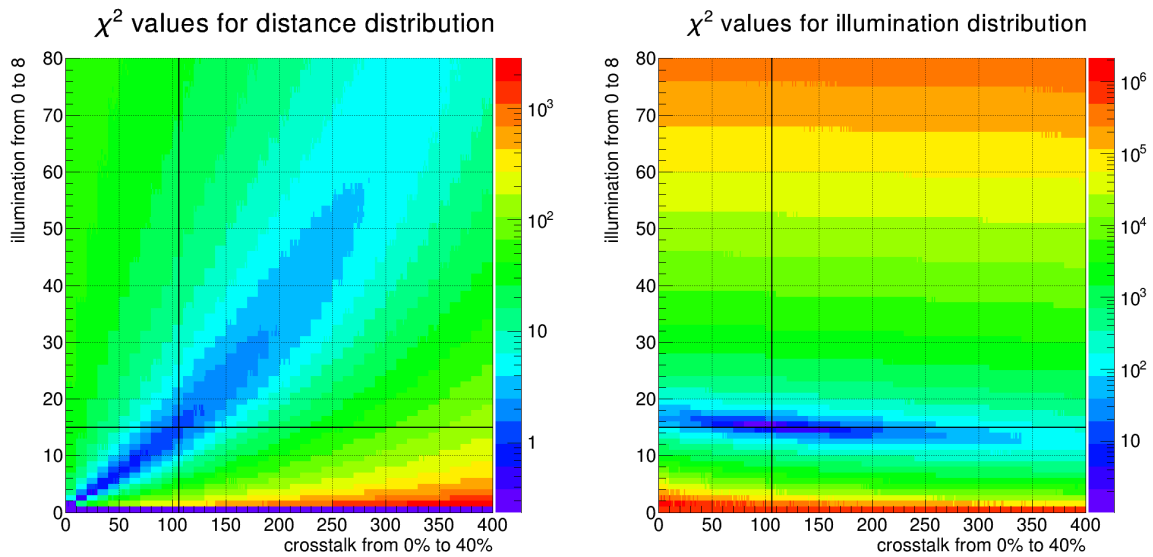


Figure 5.13. – Distributions of χ^2 for the distance distribution (left) and for the illumination distribution (right) for 400 simulated values of crosstalk (from 0% – 40%) and 80 simulated values of the illumination mean (from 0 – 8). The results are for PMT #1, the data was taken from run #207.

a different behaviour, which was also seen in their single-photon spectra, resulting in an increased amount of calculated crosstalk.

The different amounts of crosstalk for the different sensor types can be explained by several points:

- The H8500 should typically have a crosstalk in the order of 3% (Hamamatsu datasheet, [44]), and has been previously measured with a crosstalk in the order of magnitude of around 11% (from 2011 beamtest data, [27]). The results gained here confirm these previous measurements. The numbers from Hamamatsu cannot be directly compared to the results presented here, as the method of deriving the amount of produced crosstalk is completely different. Hamamatsu uses an aperture of $\sim 5 \text{ mm} \times 5 \text{ mm}$ to illuminate one pixel (the pixel-size is $5.8 \text{ mm} \times 5.8 \text{ mm}$, i.e. not the complete pixel was illuminated). As could be seen in single-photon scans ([47]), the amount of produced crosstalk depends on the hit position on the pixel itself, with a strongly increasing amount of produced crosstalk towards the edges of a pixel. Therefore the measurements from Hamamatsu should show a smaller amount of produced crosstalk.
- The R11265 is optimised for single-photon measurements and has by design a very small amount of produced crosstalk hits, especially in comparison to the H8500 MAPMT type, which was not specifically developed for single-photon measurements. Crosstalk is one factor, besides e.g. thermal emission of electrons from the cathode, which causes false hits being detected, and thus needs to be reduced to get a clear signal-only response from the sensor.
- The XP85012 MCPs use a completely different charge amplification scheme (microchannel plates) which is known to cause an increased amount of crosstalk via charge-sharing in

Table 5.5. – Results of the crosstalk estimation for all measured sensors. The corresponding value of the illumination distribution is also given. All results are based on the LED-run #207. The given errors remark just an uncertainty region and no real error of the calculated value.

PMT no	type	resulting crosstalk in %	resulting illumination mean
1	H8500	10.6 ± 3.3	1.5
2	H8500	10.7 ± 3.1	1.9
3	H8500	8.2 ± 3.6	1.9
4	H8500	15.9 ± 3.2	2.2
5	H8500	12.0 ± 2.3	1.2
6	H8500	15.0 ± 3.1	1.3
7	H8500	12.8 ± 3.0	1.7
8	H8500	10.6 ± 3.1	2.0
9	H8500	8.5 ± 3.3	1.0
10	H8500	10.0 ± 2.9	1.4
11	H8500	13.2 ± 3.2	1.7
12	H8500	24.2 ± 1.5	2.0
13	XP85012	71.0 ± 12.0	1.4
14	XP85012	80.0 ± 21.0	1.7
15	XP85012	78.0 ± 25.0	1.2
17	R11265	1.1 ± 5.1	0.3
18	R11265	1.8 ± 2.3	0.3
18	R11265	0.7 ± 4.5	0.4
20	R11265	0.7 ± 2.4	0.4
21	R11265	0.7 ± 4.5	0.4
22	R11265	0.7 ± 2.3	0.3
23	R11265	0.9 ± 3.6	0.2
24	R11265	3.6 ± 6.4	0.2

neighbouring channels compared to a photomultiplier based on a dynode system. As far as we know this MCP type includes intentionally a certain amount of crosstalk, to be able to increase the position resolution by weighting over all detected signals. Further explanations of the crosstalk behaviour of the MCPs will be discussed below. Newer versions of this MCP type were produced with a smaller distance between the anode pad and the microchannel plates, resulting in a reduced amount of crosstalk, nearly comparable to the H8500 MAPMTs.

Comparing these new results with results from the 2011 beamtest (from [27]) (which is only available for some H8500 sensors), partially larger differences become visible, especially up to PMT #6. For PMT #7 to #12 the results are nearly identical. The reason for this difference is the method of crosstalk calculation as already explained above. The results obtained with the new method give a much more uniform behaviour, with crosstalk values being fairly constant for sensors of the same type. To verify these results, the old method was applied to the 2012 beamtest

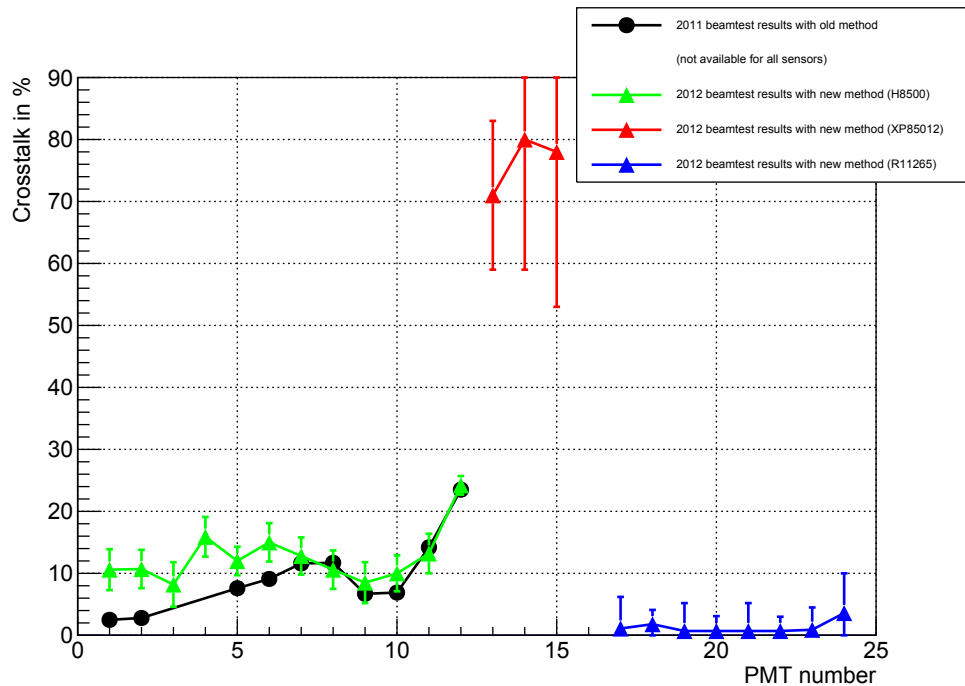


Figure 5.14. – Calculated crosstalk amount of all used sensors during the beamtest 2012 gained from run #207 (triangles). The different sensor types are marked by different colors (green: H8500, red: XP85012, blue: R11265). In addition results gained from the 2011 beamtest for some H8500 MAPMTs are shown (black dots). The lines are only drawn for better visual assignment of the different data points. The error bars remark just an uncertainty region and no real error of the calculated crosstalk value.

data and in addition corrected with the calculated dependence between the calculated crosstalk amount and the absolute illumination intensity shown in Figure 5.12. The corresponding results are included in Figure 5.15 together with the previous gained results.

The results show, that the old method is not sufficient for the 2012 beamtest data (Figure 5.15, marked in red), although it is possible to adequately correct them (shown in blue), giving nearly the same crosstalk values as extracted with the new method (shown in green). Larger differences remain for PMT #12 and #24.

Discussion of MCP crosstalk

The calculated results for the three tested Photonis XP85012 MCPs with around 70 % – 80 % are quite high, especially in comparison to the decent amount of both Hamamatsu MAPMT types. But all measurements up to now indicate, that the tested MCPs indeed produce a significant larger amount of crosstalk than the MAPMTs. This was also observed with single-photon scans from our group ([47, 48]), which used a completely different way of analysis, and can as well be judged by the data distributions used for the crosstalk estimation (see Appendix B), where the first bin in the distance distribution (i.e. the bin containing all crosstalk hits) is much more distinct for the MCPs than for the MAPMTs.

Unfortunately there doesn't exist any other quantitative studies about the crosstalk behaviour

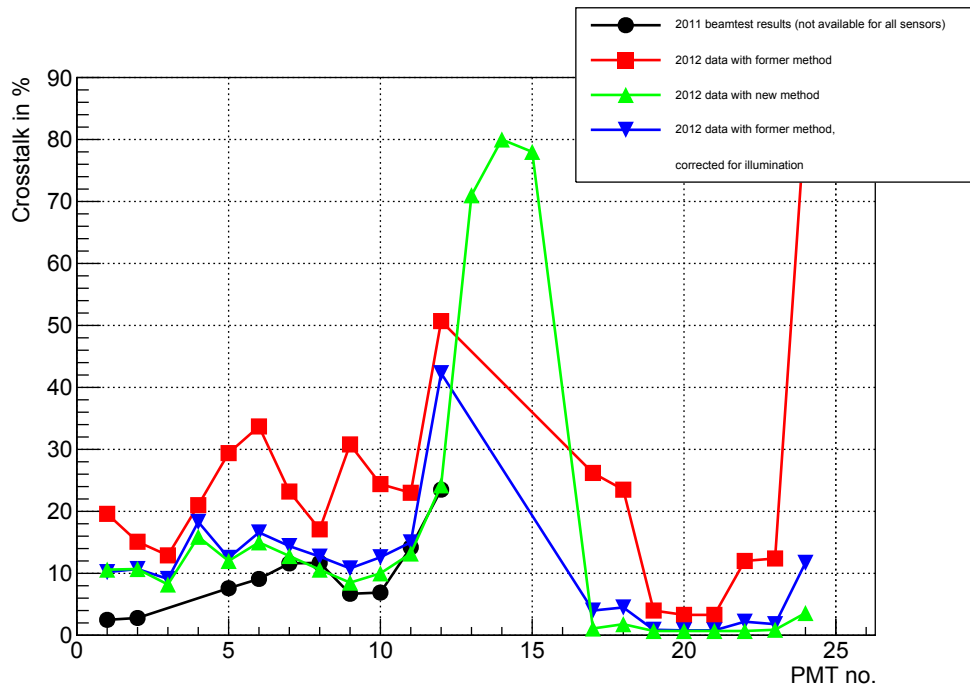


Figure 5.15. – Calculated crosstalk results from the beamtest 2012 gained from run #207 with the new enhanced method (green), with the old method (red), with the old method and applied corrections (blue), and results previously gained during the 2011 beamtest (black).

of this MCP type, only a few qualitative ones presented e.g. in [49, 50]). The authors conclude that the amount is relatively small and can be handled without problems, which cannot be seen as a confirmation or refutation of our results. A very important remark, when comparing the presented crosstalk results to the results of any other group, is the difference in handling and setting the hardware threshold. The choice for MCPs instead of MAPMTs is nearly always driven by a magnetic field in the operation region, which therefore excludes MAPMTs from the beginning on. Subsequently, when only testing MCPs, the hardware settings (mainly the signal thresholds) are adjusted based on the signal response of the MCPs.

There is nearly no data available directly comparing MCPs and MAPMTs under exactly the same conditions. Thus hardware adjustments like the thresholds are most likely very different in comparison to other groups (which either tested MAPMTs or MCPs) and were done here with respect to the MAPMTs. As a result a difference occurs, because the MAPMTs are nearly noise-free within short time-intervals, opening up the possibility to set the thresholds to extremely low values (MAPMTs and MCPs had the same thresholds in our setup). Analyses from the beamtest data show (mentioned in [51]) that the noise-rate of the MCPs is at least one order of magnitude larger than of the MAPMTs, making it necessary to increase the threshold for MCPs.

As a conclusion from that, the different thresholds cause a very varying crosstalk behaviour, which explains the various results. Further, by applying an additional ADC cut on the taken data, it is possible to reduce the amount of measured crosstalk of the MCPs, but at the expense of a lower detection efficiency. A related study is shown below in Section 5.5.

Uncertainties of the new enhanced method

The presented method of crosstalk estimation was completely new developed, being based on the comparison between simulations and real data. Since the simulated distributions match well the data, the systematic uncertainties are expected to be small. Statistical variations of the simulated data can be minimized by simulating a large amount of data. The influence of the statistics of the real data is also quite small due to the large number of entries (the distributions used for crosstalk calculation and shown in Appendix B have statistics in the order of magnitude of 10^5).

To get an estimate on the error of the derived crosstalk values, the width of the sum of both χ^2 -distributions is evaluated (by projection onto the x -axis, which is the simulated crosstalk amount). The extracted curve is then fitted with a polynomial of second degree ($f(x) = y_0 + m \cdot (x - x_0)^2$) with a fixed value for x_0 being the best resulting crosstalk value. The uncertainty region is then defined as the range that is necessary to double the vertex-value, i.e.

$$f(x) = 2y_0 = y_0 + m \cdot (x - x_0)^2 \Rightarrow x - x_0 = \pm \sqrt{\frac{y_0}{m}} \quad (5.5)$$

The absolute value of $\sqrt{\frac{y_0}{m}}$ is then assumed as the uncertainty of the crosstalk results. For the Hamamatsu H8500 MAPMTs this is in the order of 3 %, for the Hamamatsu R11265 MAPMTs in the order of 5 %, and for the Photonis XP85012 MCPs in the order of 20 %.

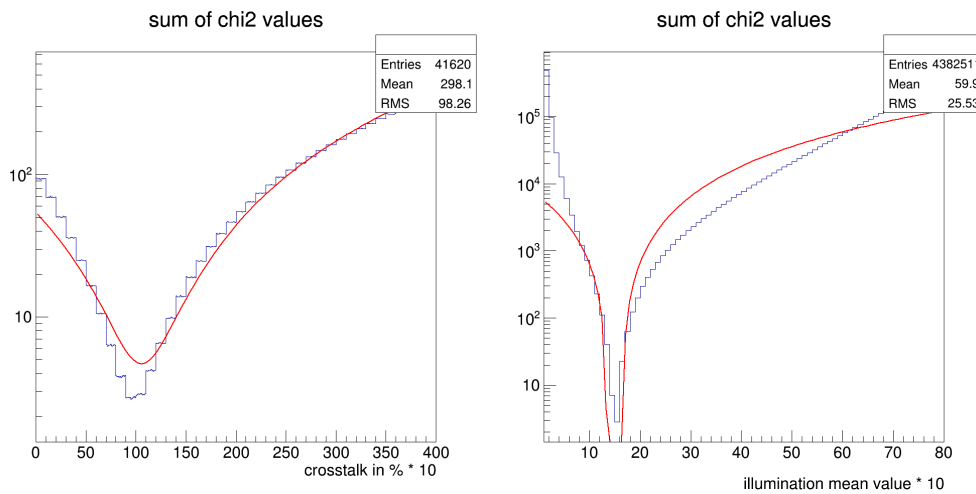


Figure 5.16. – Projected χ^2 -values of the χ^2 -sum distribution along the crosstalk-axis (x -axis) for the best fitting illumination-value (left) and along the illumination-axis (y -axis) for the best fitting crosstalk-value (right). Both projections were fitted with a second order polynomial function (red).

5.5 Photon detection efficiency

An absolute value for the detection efficiency was not the aim of the analyses, but only a comparison of the detection efficiencies of the different sensor types. The basis for the photon detection efficiency presented here is the mean number of detected real photons per electron Cherenkov ring, i.e. crosstalk hits should not be included in this number. For an adequate comparison of the sensor types the different correction factors as described in the previous chapters have to be considered, especially the correction of the crosstalk amount.

From the ring finding and fitting routines the number of hits for each found and fitted ring can be extracted, including crosstalk hits. The analysed data are taken from the HV-scan and the threshold-scan to get results for different high-voltages and for different hardware thresholds.

All rings have a different number of detected photons and result in Gaussian distributions. Therefore the mean value of this distribution is used for the further calculations. As described above several corrections are applied to the extracted number of detected photons per electron Cherenkov ring. The applied correction factors are summarized briefly in the following.

Geometrical coverage: To correct the results for the different geometrical coverages realised in the 2012 beamtime, the following values were used: H8500 - 97.21 %, XP85012 - 74.57 %, R11265 - 74.91 % (see Section 5.2). With these factors the results were scaled up to a geometrical coverage of 100 % for better comparability (as would be achieved, if multiple PMTs would be installed without any additional gaps between the PMTs).

Temperature and pressure: The correction of the temperature and pressure is applied to the mean value of the hit multiplicity distribution with using the linear approximation. This can be done, as there is no significant difference between the analytical and the approximative correction. Correcting the mean value instead of each single event changes the absolute results, but does not affect the conclusion made from this point. This correction aims at achieving the same conditions of temperature and pressure ($p = 1000 \text{ mbar}$ and $T = 0^\circ\text{C}$) as used in the simulations to get comparable values.

Crosstalk: The crosstalk is subtracted (based on the calculated values previously shown), leaving in statistically only real photon hits. As crosstalk hits are additional hits resulting in a total of $(100 + X) \%$ measured hits, the correction is always done towards 100 %.

The corrected mean number of photons per Cherenkov ring $N_{\text{corrected}}$ is obtained by applying all corrections consecutively to the uncorrected mean number $N_{\text{uncorrected}}$ via the following formula:

$$N_{\text{corrected}} = N_{\text{uncorrected}} \cdot \frac{1}{\alpha_{\text{geo}}} \cdot \frac{1000 \text{ mbar}}{\alpha_{\text{pressure}}} \cdot \frac{\alpha_{\text{temperature}}}{273.15 \text{ K}} \cdot \frac{1}{1 + \alpha_{\text{crosstalk}}} \quad (5.6)$$

$N_{\text{uncorrected}}$ is the mean number of photons per Cherenkov ring directly extracted from the beamtest data. The factors α_{geo} , α_{pressure} , $\alpha_{\text{temperature}}$, and $\alpha_{\text{crosstalk}}$ are the correction factors for the geometrical coverage, pressure, temperature, and the crosstalk.

For the estimation of the error of $N_{\text{corrected}}$ only the error of the crosstalk estimation $\alpha_{\text{crosstalk}}$ needs to be considered, as the statistical errors of the geometrical coverage estimation, the temperature, and the pressure are too small. This results in an error estimation via

$$\begin{aligned}\Delta N_{\text{corrected}}^2 &= \left(N_{\text{uncorrected}} \cdot \frac{1}{\alpha_{\text{geo}}} \cdot \frac{1000 \text{ mbar}}{\alpha_{\text{pressure}}} \cdot \frac{\alpha_{\text{temperature}}}{273.15 \text{ K}} \cdot \frac{1}{(1 + \alpha_{\text{crosstalk}})^2} \cdot \Delta \alpha_{\text{crosstalk}} \right)^2 \\ &= N_{\text{corrected}}^2 \cdot \left(\frac{\Delta \alpha_{\text{crosstalk}}}{1 + \alpha_{\text{crosstalk}}} \right)^2\end{aligned}\quad (5.7)$$

For the value of $\Delta \alpha_{\text{crosstalk}}$ the above explained value for the uncertainty is used.

Dependence of the detection efficiency on PMT high-voltage

The results from the high-voltage scan in terms of number of detected hits per electron Cherenkov ring can be seen in Figure 5.17. During this scan the high-voltage of the sensors on position I (Hamamatsu R11265), G (Photons XP85012), and E (Hamamatsu H8500) was varied. Position A (Hamamatsu H8500) is the reference position (black line), which was always set at a constant high-voltage of 1000 V, as data at this position was taken regularly. The shown results include the values only with the correction of the geometrical coverage (dashed lines) and with all applied corrections (continuous lines). The MCPs have a different scale of the high-voltage axis, ranging from 1600 V up to 1900 V, whereas the MAPMTs were tested with high-voltages between 900 V and 1100 V. It was adjusted such that the typical high-voltage (MCPs: 1750 V – 1800 V, MAPMTs: 1000 V – 1050 V) is at the same x-position and the division along the axis is equal. The drawn error bars remark the uncertainty region, which was calculated with the above estimated uncertainty of the resulting crosstalk values.

The constant distribution of the reference values implies very stable conditions during the whole high-voltage scan. Applying the corrections for these values is not necessary as this would not alter the shape significantly but would only lead to a shift along the y-axis.

There is clearly a large difference visible when comparing the XP85012 MCPs and the H8500 and R11265 MAPMTs. Applying the overall corrections to the MAPMTs leads to an increase in number of detected hits per ring, whereas for the MCPs this yields in a decrease due to the large crosstalk correction.

Overall a nearly linear increase in detected number of hits is visible for all three sensor types with roughly the same slope. After applying all corrections the Hamamatsu R11265 MAPMT detects most photons per electron Cherenkov ring, ranging from 23 photons at 900 V up to nearly 31 photons at 1100 V. The Hamamatsu H8500 MAPMT in comparison detects between 2 and 4 photons less, depending on the high-voltage, with an increasing difference at higher high-voltages. Considering the different cathode types (R11265: SBA, H8500: BA) and the numbers presented in Table 3.1, this explains the difference partially.

The XP85012 MCPs in contrast show the highest number of detected Cherenkov photons per ring before applying the corrections, but fewest number of detected photons with applied corrections. This large difference here is due to the high amount of produced crosstalk of the MCPs. After correction the results are slightly worse in comparison to the H8500 MAPMTs.

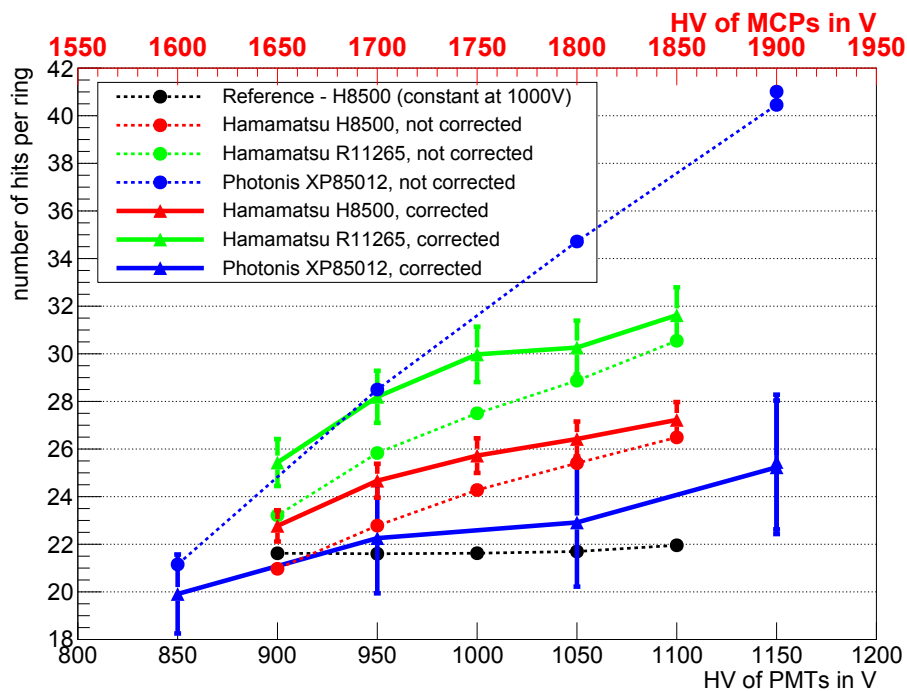


Figure 5.17. – Results for the number of detected hits per electron Cherenkov ring from the high-voltage scan. The high-voltage on positions I (Hamamatsu R11265), G (Photonis XP85012), and E (Hamamatsu H8500) was varied, and on position A (Hamamatsu H8500) was at a constant value for reference. The dashed lines remark the results with the correction of the geometrical coverage only, the continuous line with all applied corrections. The drawn error bars mark the uncertainty region based on the uncertainty of the calculated crosstalk.

Dependence of the detection efficiency on hardware threshold

A similar procedure as with the HV-scan was done with a constant high-voltage but different hardware threshold values, ranging from 25 to 70 (25 - 28 - 35 - 50 - 70 in a.u.). The results are shown in Figure 5.18.

Increasing the hardware threshold when keeping the high-voltage at the same level is expected to behave similar like decreasing the high-voltage and keeping the hardware threshold at the same level, with respect to the efficiency, as in both cases the fraction of entries above the threshold stays the same. A different high-voltage stretches the spectrum, whereas the hardware threshold cuts away entries at low amplitudes. The results indicate that this indeed seems the case.

Again the Hamamatsu R11265 MAPMTs show the highest number of detected hits per ring, starting from 29.5 hits at a threshold of 25 down to around 26 at a hardware threshold of 70. The Hamamatsu H8500 show a similar trend going down from around 22 hits to nearly 20 hits per ring. In this comparison the Photonis XP85012 MCPs show roughly the same performance as the H8500 MAPMTs with slightly less detected hits. Again there is a large difference for the MCPs before and after applying the correction, mainly influenced by the large amount of crosstalk at low thresholds.

Table 5.6. – Used correction values for the HV-scan for the calculation of the number of mean hits per electron Cherenkov ring. Different values for temperature and pressure are a result of a different time the runs were taken.

PMT type	run no.	HV in V	α_{pressure} in mbar	$\alpha_{\text{temperature}}$ in K	$\alpha_{\text{crosstalk}} \pm \Delta\alpha_{\text{crosstalk}}$
H8500	102	1100	955.9	291.7	0.09 ± 0.03
	106	1050	956.4	292.8	0.08 ± 0.03
	111	1000	955.7	293.1	0.06 ± 0.03
	116	950	954.7	293.0	0.04 ± 0.03
	120	900	953.8	293.7	0.04 ± 0.03
R11265	101	1100	956.6	292.1	0.08 ± 0.04
	104	1050	956.1	292.9	0.07 ± 0.04
	108/9	1000	955.4	293.0	0.03 ± 0.04
	113/14	950	954.5	293.1	0.03 ± 0.04
	118	900	953.5	293.9	0.03 ± 0.04
XP85012	100	1900	956.2	291.8	0.80 ± 0.20
	105	1900	955.9	293.1	0.80 ± 0.20
	110	1800	954.8	292.7	0.70 ± 0.20
	115	1700	954.4	293.2	0.44 ± 0.15
	119	1600	953.4	294.2	0.20 ± 0.10

Reducing the crosstalk of the MCPs with an ADC-cut

As explained above the Photonis XP85012 MCPs show a large amount of crosstalk, also when comparing to the results of other groups. To explain the different results an additional cut on the signal value (in terms of ADC values) was applied and the amount of crosstalk and the resulting number of hits per Cherenkov ring extracted. The results are shown in Figure 5.19 for five different ADC cuts ranging from 0 to 400 (for comparison: the single-photon peak position is in the range of 200 – 300, thus a high cut value strongly affects the efficiency). The data was taken from run #110.

The results clearly show, that the amount of produced crosstalk of the MCPs can be significantly reduced by applying an additional cut on the signal strength, from around 75% with no cut (i.e. only hardware threshold counts here) down to less than 10% at an ADC cut of 400. At the same time this also drastically reduces the number of detected real photon hits, decreasing from around 16 hits down to 8 hits (the correction for the geometrical coverage was not applied here). But already an ADC cut of 100 or 200 is enough to reduce the crosstalk by a large fraction and keep a lot of the real photon hits.

This behaviour also gives a further hint on the previous assumption, that other groups use a higher relative hardware threshold and therefore do not detect this high amount of crosstalk in the MCPs, which has been identified in our data.

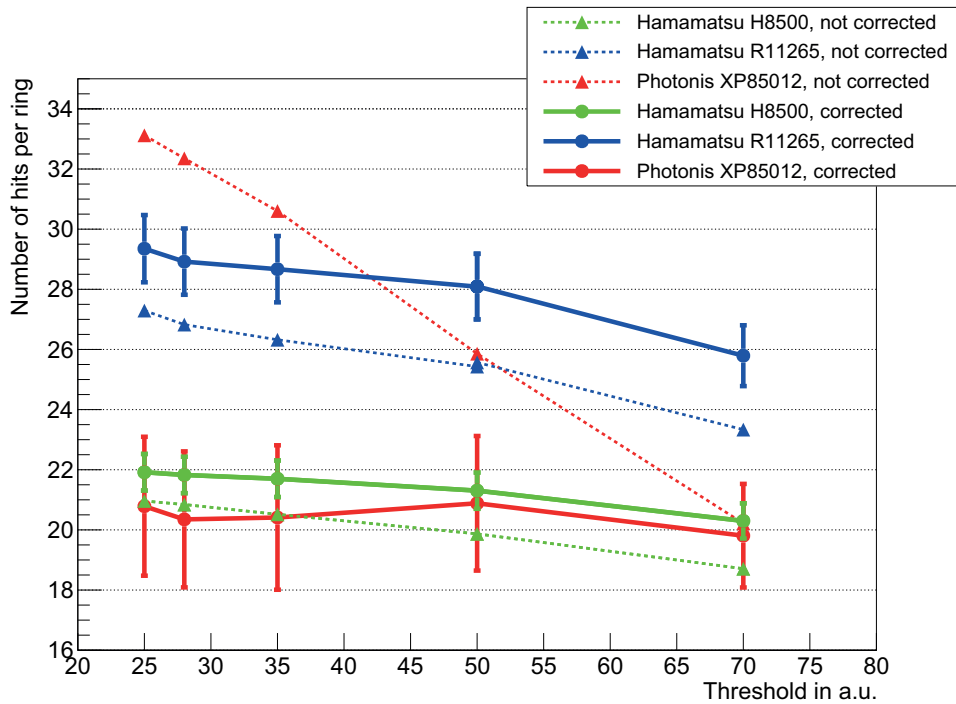


Figure 5.18. – Results for the number of detected hits per electron Cherenkov ring from the threshold scan. The dashed lines remark the results with the correction of the geometrical coverage only, the continuous line with all applied corrections. The drawn error bars mark the uncertainty region based on the uncertainty of the calculated crosstalk.

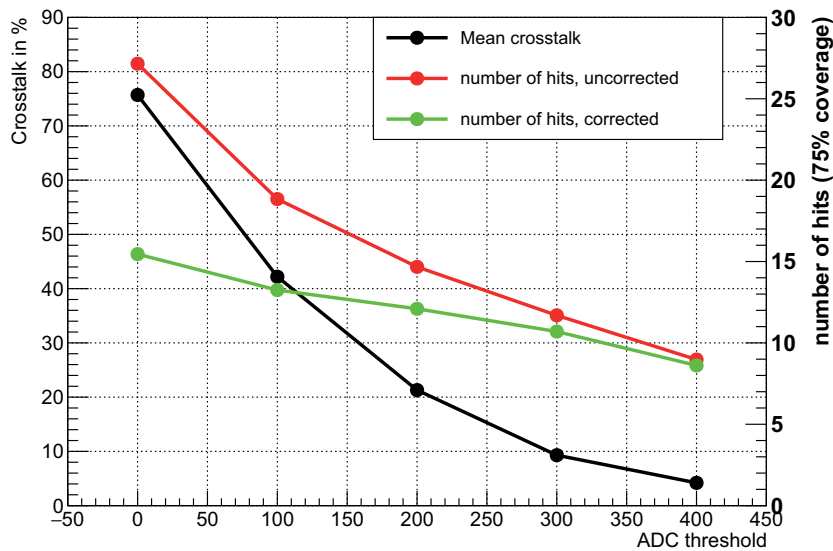


Figure 5.19. – Behaviour of the data for the Photonis XP85012 MCPs in terms of number of hits per ring for different applied ADC cuts. Black: development of crosstalk amount, red: mean number of hits per ring (without corrections for geometrical coverage, temperature, pressure, and crosstalk). green: mean number of hits per ring with crosstalk correction.

5.6 Summary: Overall performance comparison

The overall performance comparison of the three different sensor types, which were tested during the 2012 beamtest at the CERN PS/T9 beamline, includes several aspects: the single-photon spectra, the estimation of the crosstalk amount, and the resulting numbers of photons per electron Cherenkov ring for various high-voltages of the sensors and thresholds of the used read-out electronics.

Single-photon spectra

The response to single-photons is very different for all three tested sensors. The H8500 MAPMTs show spectra with most often a clearly distinct single-photon peak and an additional low-amplitude peak. The R11265 MAPMT spectra feature nearly no low-amplitude peak (at least above the - very low - hardware threshold) and only the single-photon peak. A complete lack of a low-amplitude peak cannot be excluded, but it consists of signal strengths much lower than for the H8500 type and mainly below hardware threshold. The single-photon spectra of the XP85012 MCPs are strongly dominated by the low-amplitude peak and the single-photon peak is only hardly visible in the spectra, if no further cuts are applied.

By applying a cut, which only considers hits without any additional hit in the neighbouring pixel, the single-photon spectra can be improved, especially for the MCPs, as this results in a clearly better single-photon peak and a decreased low-amplitude peak. Due to the results from this additional cut it is assumed, that the low-amplitude peak mainly consists crosstalk hits.

Since CBM will use triggerless and free-streaming electronics, a certain hardware threshold has to be applied to cut out noise. Deriving such a threshold from the single-photon spectra of the Hamamatsu MAPMTs is easy due to the clear separation of low-amplitude and single-photon peak, but is much worse for the Photonis MCPs.

Crosstalk behaviour

The crosstalk behaviour of all three tested sensors is very different. The Hamamatsu H8500 MAPMTs show a decent amount of crosstalk in the range of 8% – 16% (probability for an additional hit in one of the neighbouring pixel), whereas the Hamamatsu R11265 MAPMTs show nearly no crosstalk of up to 3% at typical high-voltages of 1000 V – 1050 V at a hardware threshold of the n-XYter of 28 a.u. The Photonis XP85012 MCPs show a very large amount of crosstalk in the order of 70% – 80% at typical high-voltages of 1850 V and the same hardware threshold.

The Hamamatsu data-sheet of the H8500 type shows a resulting crosstalk of around 3%, which is less than what has been estimated here. The reason is a completely different method of crosstalk estimation used by Hamamatsu, by just illuminating an area of 5 mm × 5 mm of one pixel (pixelsize is 5.8 mm × 5.8 mm, i.e. not the whole pixel is illuminated) and measuring the sensor response. As could be seen in single-photon scans of the sensors, the amount of produced crosstalk drastically increases near the edges of a pixel, thus explaining the different amounts of crosstalk, stated by Hamamatsu in comparison to the present results.

Crosstalk is a property negatively influencing the occupancy of the camera. From simulations a total pixel-coverage per event (central Au + Au collision at 25 AGeV) of around 10 % of all camera pixels has been estimated (i.e. which produce a signal), mainly concentrated on the central region. The number of hits within this high-density region is around a factor of 5 – 10 higher than in the low-density regions (see e.g. [18]). Crosstalk in the order of 10 % – 20 % is expected to have just a minor influence in the high-density region, but everything above will negatively influence the ring identification and reconstruction possibilities. Therefore, crosstalk should be avoided or at least tried to be kept as small as possible.

Detection efficiency in dependence on high-voltage of sensors and hardware threshold

The efficiency in terms of number of hits per electron Cherenkov ring was estimated for different high-voltages (with fixed hardware threshold) and for different hardware thresholds (with fixed high-voltage). The number of detected hits has to be corrected for the geometrical coverage, for the varying temperature and atmospheric pressure, and for the different crosstalk amounts, to get comparable numbers.

The resulting corrected values show that the Hamamatsu R11265 MAPMTs perform best of all three sensor types, yielding the highest numbers of detected hits per ring. The Hamamatsu H8500 MAPMTs and the Photonis XP85012 MCPs yield roughly the same numbers, with a slight better tendency for the H8500.

The quantum efficiency of the sensor's cathode significantly determines the number of detected Cherenkov photons per ring. Comparing the relative numbers for the quantum efficiency folded with the Cherenkov spectrum from Table 3.1 with the results described within this chapter, underlines these results and confirms the expectations, that the Hamamatsu R11265 MAPMT should yield the highest number of detected Cherenkov photons. Also, a nearly similar result for the Hamamatsu H8500 (D-03) and the Photonis XP85012 MCP has already been expected from these relative numbers and were confirmed.

Overall conclusion

Based on the presented results both Hamamatsu MAPMT types are well suited to be used in the CBM-RICH camera, whereas the Photonis XP85012 MCPs do not fulfil our requirements to the same extend as Hamamatsu's models (especially when considering the high price). The performance in terms of number of detected hits per electron Cherenkov ring is worse than of both MAPMT types. The high amount of crosstalk at low hardware thresholds drastically increases the overall signal and data rate, which is a problem especially in the high-density regions of the CBM-RICH camera. Although the crosstalk amount can be handled by increasing the threshold, this also negatively affects the detection efficiency.

Further developments

In 2013/14 Hamamatsu presented a new type of MAPMT as a successor of the H8500, the H12700. This model combines the advantages of both tested MAPMT types (H8500 and R11265): it has the

same dimensions as the H8500, it has a completely reworked dynode system based on the R11265, and it is available with an improved bialkali cathode, which reaches nearly the same quantum efficiencies as the super-bialkali cathode of the R11265.

Several pieces of the H12700 were tested during another beamtest in November 2014 and did undergo detailed studies in our laboratory. All these tests showed clearly better results in comparison to the H8500 and R11265, which was the reason to decide for this MAPMT type to be used in the CBM-RICH.

Also the Photonis MCPs benefitted from several improvements. The main improvement is a shorter distance between the anode and the microchannel plates, which strongly reduces the amount of produced crosstalk and thus yields better single-photon spectra. In addition the quantum efficiency capabilities of the cathode has been enhanced.

Pre-studies for conversion analysis of dileptons

The previous chapters covered the comparison of different sensors for the photon detector camera of the CBM-RICH detector, which is one important technical aspect to detect electrons with high efficiency, in particular as the RICH detector plays a key role for electron identification. The high electron detection capabilities of the RICH detector together with the high momentum resolution of the tracking system can now be used to reconstruct photons via conversion into electrons.

In this chapter several simulation studies for the conversion analysis are presented, which help understanding the simulation properties and estimating cut-values for the case, where only reconstructed data is used to identify electrons and combine them to photons.

A short introduction into the conversion method is given in Section 6.1, followed by an explanation of the used CBMROOT framework and details on the simulation in Section 6.2. The so-called detector tomography is a first application of the conversion method, revealing all parts of the detector with a high conversion rate, shown in Section 6.3.

Reconstruction studies only based on MC-true data to identify electrons and combine them to π^0 are presented in Section 6.4. Studies with the additional use of reconstructed momenta for the combination are presented in Section 6.5.

Section 6.6 covers the estimation of exact cut-values for reconstructed tracks to be identified as electrons and for their further combination to photons. This provides the basics for the results presented in Chapter 7.

Some very first studies on the topic of the reconstruction of π^0 by the conversion method were made by Melanie Klein-Bösing in 2009 ([52]), but with a much less amount of statistics for the simulations and outdated detector geometries (e.g. the RICH will now use a different radiator and the photomultiplier have increased detection efficiencies).

6.1 The Conversion Method

The conversion method has already been successfully applied in the analysis of data from the PHENIX experiment at RHIC in Au + Au collisions at a nucleon-nucleon center-of-mass energy of $\sqrt{s_{NN}} = 200$ GeV ([53]), from the ALICE experiment at LHC in proton-proton collisions at $\sqrt{s_{NN}} = 7$ TeV ([54]), and from the HADES experiment at GSI in p + Nb collisions at a beam energy of 3.5 GeV ([55]).

The main idea of the conversion method is relatively simple: Instead of measuring photons, e.g. from π^0 decays, directly using an electromagnetic calorimeter, the photons are measured indirectly by detecting e^+e^- -pairs stemming from conversion $\gamma \rightarrow e^+e^-$ somewhere in the target or in the material of the detector. Those reconstructed photons are then further combined to form a π^0 or η from the decay-channels $\pi^0/\eta \rightarrow \gamma\gamma$. Also the Dalitz decay-channel $\pi^0/\eta \rightarrow \gamma e^+e^- \rightarrow e^+e^-e^+e^-$ can be reconstructed with the conversion method.

In CBM all charged particles are tracked with the MVD and the STS, and the identification of electrons is done with the RICH, the TRD, and the TOF detector. The good position and time resolution of the tracking system, together with the very good electron identification properties of the RICH detector, allow for a very precise reconstruction of π^0 and η with the conversion method.

Compared with the photon reconstruction using an electromagnetic calorimeter, both methods have different advantages. In CBM the calorimeter is planned to be positioned behind all other detectors, impairing the energy resolution and increasing the background in the calorimeter due to the overall material budget of the other detectors. Another advantage of the conversion method is the (expected) better invariant mass resolution of π^0 and η , as the momentum resolution of electrons and positrons combined will be better than the photon energy resolution of the calorimeter. A disadvantage is the low conversion rate of photons within the first 70 cm downstream of the target and thus a low reconstruction probability for π^0 and η (each electron or positron track must be detected in at least 3 STS stations for reconstruction and therefore be originated before $z = 70$ cm).

The conversion of the decay-photons can either happen directly within the target itself or somewhere within the detector material. In standard track reconstruction in STS each particle is expected to originate from the primary vertex and accordingly fitted. Thus particles (here electrons and positrons) with an origin in the detector will suffer from an incorrect reconstructed momentum. A dedicated software package 'KFParticle Finder Package' ([56]) has been developed to specifically account for reconstruction of secondary vertices outside the target, but will not be used for the presented analyses in this thesis to fully understand the basic behaviour and influences of this method. Due to that, the presented studies only include conversion inside the target and not within the detector material.

For an expectation of the different amounts of conversion within the target alone, in contrast to including conversion within the detector material, the radiation lengths of the target and the sub-detectors in term of X_0 are used. For the 250 μm gold target this gives approx. 8.3% X_0 . For the MVD a material budget of 0.3% X_0 for the first station and 0.5% X_0 for each of the three following stations is estimated, summing up to 1.8% X_0 for the complete MVD. For the STS a material budget between 0.3% X_0 and 1.2% X_0 per station has been estimated (depending on the

sector of the station; see STS TDR), summing up to a total maximum of 6% X_0 for the first five STS stations (being before $z = 70$ cm). Thus, the detector alone makes up a material budget of 7.8% X_0 , which is nearly the same as of the thick gold target. From this an increase of reconstructed π^0 from conversion within the detector by a factor of 3 – 4 is expected.

6.2 The CbmRoot framework

The CbmRoot framework is used for all simulations and analyses. CbmRoot is a specific branch of FairRoot ([57]), which is based on the ROOT package ([58]) and was extended by several software packages. These additional packages include different particle generators, transport engines, and detector specific geometries and reconstruction routines.

During simulation and reconstruction several containers are generated and filled and can be used for further analyses. The most important of these containers for the presented analyses include:

MCTrack The MCTrack array stores all tracks generated during the simulations for all particles, which either themselves or one of their daughter particles (e.g. from decay or conversion) hit one detector. Each track is stored as a CbmMCTrack, including all MC-true information about this track, like momentum, origin, particle type, or mother particle ID. The MCTracks can for instance be used to crosscheck the reconstruction, particle identification, or pair matching. Based on the true MC information, all background from falsely reconstructed pairs can be suppressed.

GlobalTrack The GlobalTrack array contains all reconstructed tracks. For proper track reconstruction at least 3 hits in the STS detector are necessary. Within each GlobalTrack, information about the hits in the different detectors, the matching to an according MC-true track from simulation, and references to further arrays like StsTrack or RichRing are stored.

The matching of reconstructed and simulated tracks is based on a distance calculation and a projection and extrapolation of the STS tracks onto the RICH sensor camera (see also [59]).

Within the simulated sample, each event contains around 430 ± 22 global tracks, in comparison to around 7350 ± 1200 MCTracks.

Particle generator: UrQMD Two different particle generators are used for the input of the simulation, the first one is the Ultrarelativistic Quantum Molecular Dynamics (UrQMD, [60]) model, which is used to simulate (ultra)relativistic heavy-ion collisions in the energy range from the most important accelerators, like Bevalac and SIS up to AGS, SPS and RHIC.

For most of the simulations presented here, previous calculated input files, generated with UrQMD and each containing 1000 events, are used.

Particle generator: boxgenerator The second used particle generator is a boxgenerator, also known as particle gun. This generator allows to generate particles of a certain type (via their PDG code) within given range over the transversal momentum p_t , emission azimuth angle ϕ and polar angle θ , pseudorapidity η , or rapidity y at a fixed multiplicity per event. This is for example used for the generation of a pure π^0 event sample.

All presented analyses are made with a simulated sample of $5 \cdot 10^6$ central gold-gold collision with a beam energy of 10 AGeV, which were generated from UrQMD. The used geometry versions of

all sub-detectors are shown in Table 6.1, which is the SIS100 setup from summer of 2015.

Table 6.1. – Geometry versions of the sub-detectors used for the simulation of $5 \cdot 10^6$ UrQMD events. This setup resembles the SIS100 electron setup from summer 2015.

Detector	magnet	MVD	STS	RICH	TRD	TOF
geometry version	v15a	v15a	v13y	v14a_1e	v15a_1e	v13-5b

For the simulation the field strength of the magnetic field was set to a reduced value of 70%. This was done to increase the amount of electrons not being bended out before the RICH-detector and therefore to increase the reconstruction probability of π^0 .

6.3 Detector tomography

To understand the behaviour of photons in the CBM detector and to gain knowledge of the position-dependent conversion probabilities in the detector, the so-called ‘detector tomography studies’ are a good tool. Photons can only convert to an e^+e^- -pair in the presence of an atomic nucleus to satisfy conservation of momentum. Therefore, the conversion probability within materials of high density is larger compared to low-density materials or even gases. This can be used to study the density distribution of the implemented geometries in the simulation by investigating the conversion coordinates of photons.

As basis for the detector tomography studies the MC-true tracks from the simulation are used. The reason for taking only MC-true tracks and not reconstructed tracks is, that only conversion within MVD or STS can be reconstructed, as the origin of reconstructed tracks only covers the MVD and the first stations of the STS, but no detectors behind the STS (because to be able to reconstruct a track there must be a signal in at least 3 STS stations \rightarrow the origin of a reconstructed track is between $z = 0$ cm and $z = 70$ cm). Usage of MC-true information allows to reconstruct the conversion vertex density independently from the reconstruction capabilities of the detectors.

For the detector tomography studies only electrons and positrons were selected, which stem from the conversion of a photon, and their startvertices (which are the points of conversion of the photons) are used for further analyses.

The detector tomography studies presented here are based on a simulation sample of $5 \cdot 10^6$ events, generated from UrQMD at energies of 10 AGeV for central Au + Au collisions and with the SIS100 setup of CBM. There is also the possibility to use simulations based on randomly distributed single photon tracks of well defined momentum from the boxgenerator. The difference of the two methods is mainly the directional distribution of the photons, as it can be freely set in the boxgenerator but is fixed for the UrQMD sample. There are advantages for both. The reason here to take the photons generated during real collisions is the possibility to find out parts of sub-detectors, which might increase the background in subsequent sub-detectors. One example of this is the very inhomogeneous mirror mount structure of the RICH detector, which might cause a reduction of the reconstruction efficiency of the TRD due to conversion.

The result of this analysis, if all conversion points are projected into the x - z -plane (i.e. the view on

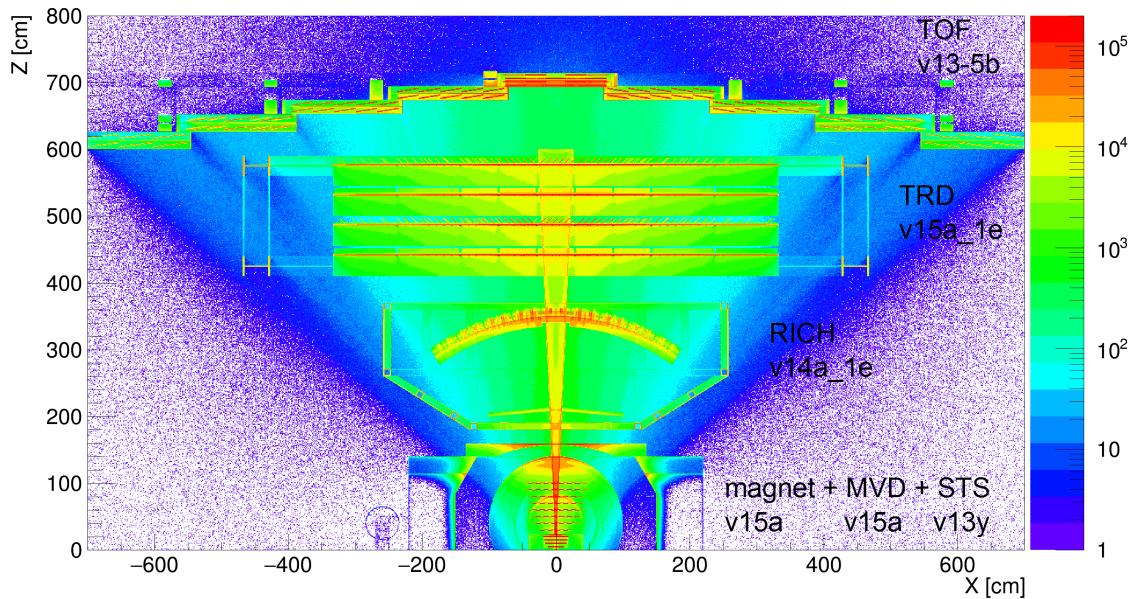


Figure 6.1. – Detector tomography of the CBM detector for the SIS100 setup. As basis $5 \cdot 10^6$ UrQMD events were taken. The colour scale of the plot was cut off at higher values for better visibility of the different structures in the detector.

the detector from the top side), can be seen in Figure 6.1. For a better visual differentiation of certain parts the z -axis was slightly zoomed in.

The different sub-detectors of CBM can clearly be distinguished in this picture, with the complete magnet at the beginning (starting at $z = 0$; e.g. the round-shaped structures are the magnet coils), the MVD and the STS inside the magnet (visible as horizontal lines of increasing size in downstream direction), and the RICH behind the magnet, with a good visibility of the camera (close to the magnet), the beampipe, and the mirror holding structure (most downstream part). The TRD, divided into four dedicated stations, and the TOF with its stepwise structure are also clearly recognizable. Conversion not only happens in the material but also in the surrounding air or gas boxes but orders of magnitude lower compared to the dense material.

Selecting only the z -region of the RICH detector ($170 \text{ cm} \leq z \leq 400 \text{ cm}$) and projecting all hits into the x - y -plane (i.e. to look from the front/back onto the RICH) results in Figure 6.2. The structures visible there is mainly the mirror holder with an overall frame and single frames and actuators for each mirror tile. The beampipe in the middle yields in a wide ring due to its conical shape. The mirror tiles make a homogeneous background and their most outer borders are visible at the outer parts. As UrQMD events were used for the generation of these pictures, the distribution of conversion points is very inhomogeneous with most of the points close to the z -axis (at $x/y = (0/0)$) and less points towards the edges. Therefore these results cannot be used for an absolute comparison of the conversion probabilities of the different parts but just for small local estimations. To be able to do an absolute comparison an homogeneous distribution of photons converting in the material is necessary (with the boxgenerator).

By projecting all conversion points from all sub-detectors onto the z -axis, one can then judge on

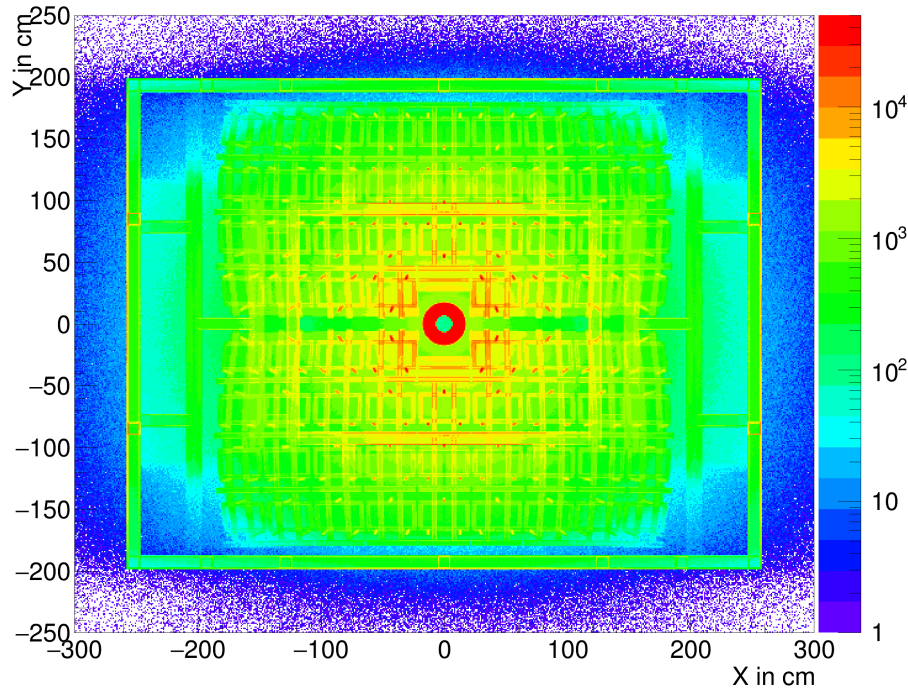


Figure 6.2. – Detector tomography of the CBM detector for the SIS100 setup. As basis $5 \cdot 10^6$ UrQMD events were taken. The colour scale of this plot was cut off at higher values for better visibility of the different structures in the detector. Shown here is the x-y-projection of the region of the RICH detector, with applying a cut on the z-axis of $170 \text{ cm} \leq z \leq 400 \text{ cm}$.

the different conversion amounts within certain parts of the sub-detectors. The result is shown in Figure 6.3. For a better separation of some of the sub-detectors red vertical lines are additionally drawn. The four MVD stations and the eight STS stations at the very beginning are clearly identifiable by very large and narrow peaks. Parts of the magnet or the magnet yoke are also visible, generating a lot of conversion in the region between the last STS station (at $z = 100 \text{ cm}$) and $z = 160 \text{ cm}$. The four TRD stations (roughly between $z = 400 \text{ cm}$ and $z = 600 \text{ cm}$) also look identical as it is expected.

Over the complete z-range a lot of underground is visible, which stems mainly from conversion in the surrounding air or gas boxes (e.g. the CO_2 inside the RICH box). The huge volume then sums up to a significant amount.

Summed up the detector tomography is a good tool to get an detailed overview of the implemented geometries of the different sub-detectors in terms of material budget or sources of background-generation in some detectors. From this it is also possible to identify errors in the implemented geometry files, e.g. wrong volume materials or dimensions.

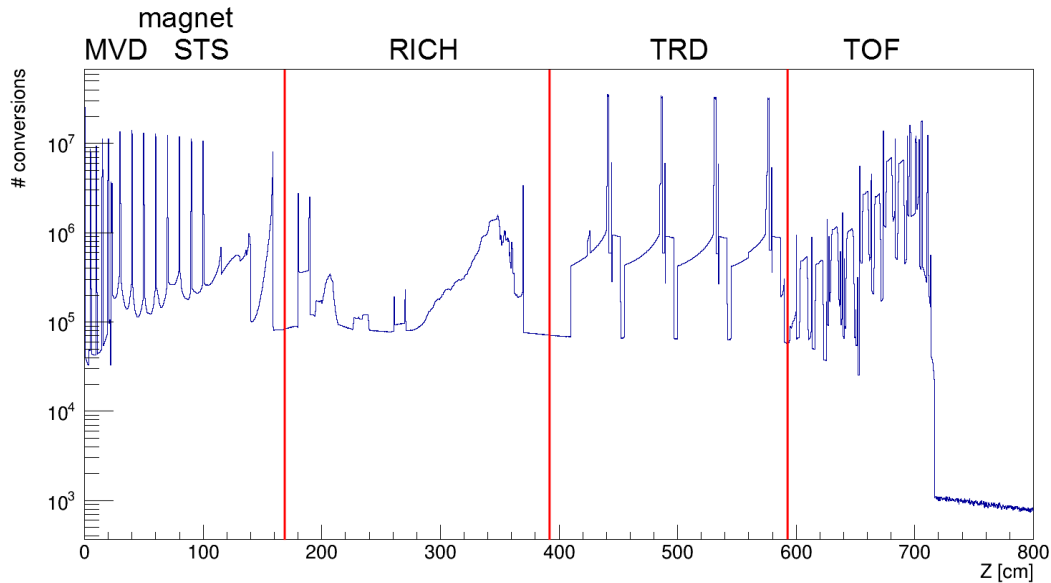


Figure 6.3. – Amount of photon conversion along the z-axis. The vertical red lines remark the edges between the magnet + MVD + STS detector and the RICH, between the RICH and the TRD, and between the TRD and the TOF.

6.4 Upper estimate of the number of reconstructible π^0/η based on conversion

The previous sections contain a short introduction into the framework used for all analyses and an application of the first reconstruction step of a e^+e^- -pair to a photon based on MC-true data. Going one step further the possibility of reconstructing π^0 or η is investigated, starting again from all electrons and positrons within the MC-true trackbank. One important aspect in this regard is an upper estimate on the number of reconstructible π^0 and η within the simulation sample.

As a starting point the number of generated π^0 , η , and also direct photons per event is counted, shown in Figure 6.4. The results show that in average 227 π^0 per event are generated, including all production processes (i.e. also from secondary vertices, within the complete CBM detector, e.g. from the decay of baryonic resonances like Δ or N , or mesonic decays like $\eta \rightarrow 3\pi^0$). Limiting this number by the origin of the π^0 , being somewhere before $z = 4$ cm (i.e. even before the first MVD station), this average number decreases to 182 π^0 per event. A further decrease to 173 π^0 per event can be seen when only including π^0 directly coming from the target, i.e. excluding the production from particle decays into π^0 . In contrast to the large amount of generated π^0 only very few η (11 per event) and direct photons (7 per event) are generated. All η are produced in nucleon-nucleon collision within the target via baryonic resonances, which have a very low lifetime, and are not produced in secondary reactions (which is the reason for only one curve being shown in Figure 6.4). The different statistics for η in comparison to π^0 (factor of ~ 20) give a very first hint that it will be much more challenging to reconstruct η in the data than to reconstruct π^0 .

Also based on the MC-true data some first reconstruction studies can be done, to get an impression

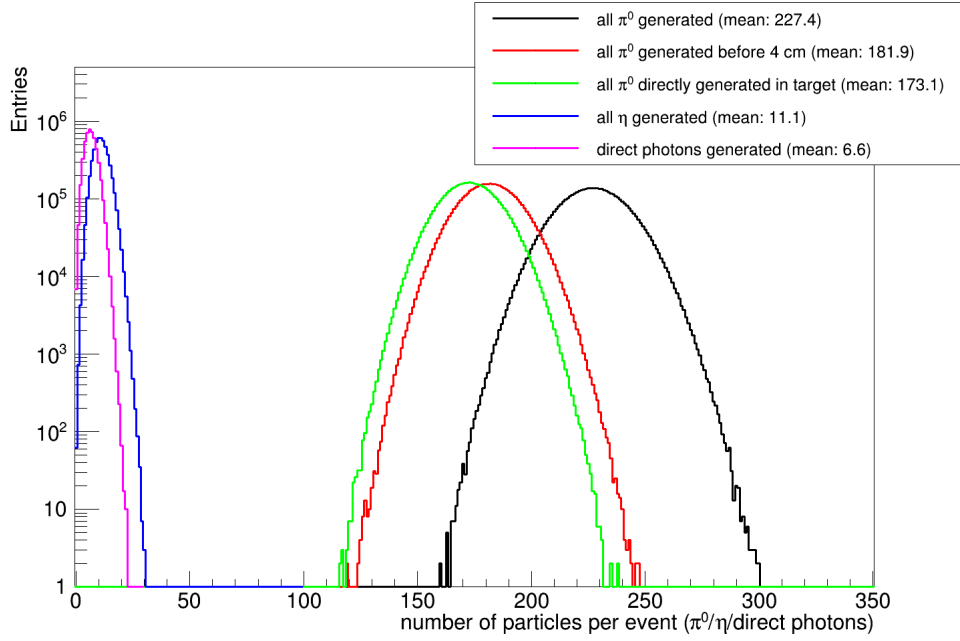


Figure 6.4. – Number of generated π^0 , η and direct photons per event for 5 million central Au + Au collisions at 10 AGeV. For π^0 it is distinguished between production in the collision, before $z = 4$ cm, and everywhere in the detector.

of the numbers of reconstructible particles. To achieve this, all electrons in the MCTrack array are selected and further combined to π^0 or η . For a realistic estimation, the spatial origin of the electrons is limited to $z \leq 70$ cm, as the track needs to make a signal in at least three STS stations, the last three of them being at $z = 100$ cm, 90 cm, and 80 cm.

To reduce the analysis sample, only electrons stemming from a photon, a π^0 , or an η are considered via the PDG-codes of the mother particle. This covers all relevant decay channels:

- $\pi^0 \rightarrow \gamma\gamma \rightarrow e^+e^-e^+e^-$
- $\pi^0 \rightarrow \gamma e^+e^- \rightarrow e^+e^-e^+e^-$
- $\eta \rightarrow \gamma\gamma \rightarrow e^+e^-e^+e^-$
- $\eta \rightarrow \gamma e^+e^- \rightarrow e^+e^-e^+e^-$

The decay channel $\pi^0 \rightarrow e^+e^-e^+e^-$ is not covered by Geant and could therefore not be studied, but it can be neglected due to the low branching ratio of approx. $3 \cdot 10^{-5}$. Also, none of the other decay channels is considered within all analyses presented in this thesis.

The results of these estimations can be seen in Figure 6.5. There only the decay channel $\pi^0 \rightarrow \gamma\gamma$ was considered, which makes up the largest fraction, and it is distinguished between π^0 directly produced in the heavy-ion collision and π^0 produced from the decay of other particles (secondary vertices; this happens everywhere in the detector). In a first step all π^0 within the trackbank were counted (first bins). Further bins include stepwise more cuts, e.g. both decay-photons are stored in the MC-true trackbank or the conversion-electrons. One important aspect to consider here is, that the estimated numbers include conversion within support structures and within the magnet,

which can not be detected and thus slightly distorts the numbers (especially important for the case with cut $z \leq 70$ cm).

The last two cuts aim for a realistic comparison with reconstructed data and therefore including the points of conversion of the two γ , either happening before $z = 70$ cm (i.e. all four leptons might be detected by the STS, hitting three stations) or directly within the target itself. For primary π^0 each of these cuts reduce the number of π^0 by one order of magnitude, for secondary π^0 the reduction is by two orders of magnitude for the first cut and one additional order of magnitude by the second cut.

Summed up, from all produced π^0 (roughly 10^9 in $5 \cdot 10^6$ simulated events) less than 0.02% decay into two γ which are directly converting in the target and all four leptons hitting one detector part. Overall less than 0.2% of all produced π^0 have a chance of being detected by the STS and further detectors (assuming that the conversion of the decay-photons must happen before $z = 70$ cm).

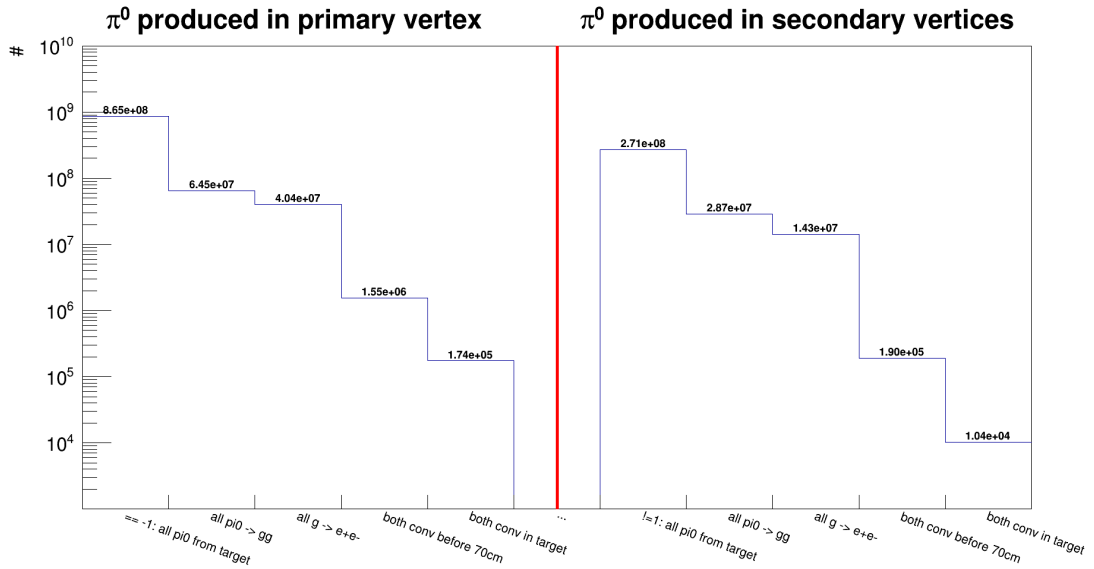


Figure 6.5. – Number of π^0 in the MC-true trackbank separated by their production within the primary vertex and within secondary vertices. Numbers are given for all π^0 produced (first column), all $\pi^0 \rightarrow \gamma\gamma$ with both γ being in the trackbank (i.e. the γ or at least one of the e^\pm from conversion hit a detector; second column), all $\pi^0 \rightarrow \gamma\gamma \rightarrow e^+e^-e^+e^-$ with all leptons being in the trackbank (third column), all conversions happening before $z = 70$ cm (fourth column), and all conversions happening in the target (fifth column). The numbers are slightly distorted as conversion within support structures and the magnet is also included, which can not be detected.

Considering now also the Dalitz decay channel of π^0 , $\pi^0 \rightarrow \gamma e^+e^-$ and $\gamma \rightarrow e^+e^-$, and calculating the invariant mass of all four leptons originating from the same π^0 and using the MC-true momenta results in Figure 6.6. These spectra only include real pions and no sort of background (i.e. wrong combination of leptons) and are calculated for the case that both (for $\pi^0 \rightarrow \gamma\gamma$) or the single photon (for $\pi^0 \rightarrow \gamma e^+e^-$) convert before $z = 70$ cm. The total invariant mass spectrum including both decay-channels is on the left side, mid and right side show only reconstructed π^0 from the decay into $\gamma\gamma$ (mid) and γe^+e^- (right). It is clearly visible that the result is not a sharp peak at the π^0 mass of 134.98 MeV ([61]) but there are also several entries especially at

lower invariant masses, with four orders of magnitude less entries. In addition the peak has a very unsymmetrical shape with a very sharp edge towards low invariant masses and a wide distribution towards higher invariant masses. Specific reasons for this behaviour cannot be given. One result from these spectra is the (relative) higher detection probability of the Dalitz-decay of π^0 due to the reason that only one photon needs to convert up to a certain point instead of two photons. This can be seen by the different number of reconstructed π^0 for each decay-channel (i.e. number of entries in the spectra), yielding the comparison

$$\frac{N_{\pi^0 \rightarrow \gamma e^+ e^-}}{N_{\pi^0 \rightarrow \gamma \gamma}} = \frac{316\,545}{1\,739\,559} \approx 0.18 > \frac{BR_{\pi^0 \rightarrow \gamma e^+ e^-}}{BR_{\pi^0 \rightarrow \gamma \gamma}} = \frac{1.174\%}{98.823\%} \approx 0.02 \quad (6.1)$$

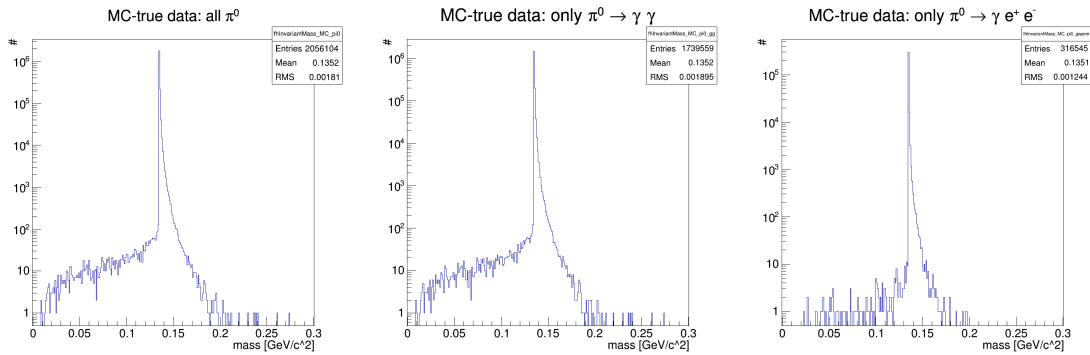


Figure 6.6. – Invariant mass of the 4 leptons originating from the same π^0 , identified and momenta via MC-true data. Left shows the sum spectrum, mid only for the decay-channel $\pi^0 \rightarrow \gamma\gamma$, and right only for $\pi^0 \rightarrow \gamma e^+ e^-$.

The resulting ratio of the number of π^0 from the two main decay-channels yields a larger value for the MC-true data in comparison to the fraction of the theoretical branching-ratios pointing out the higher reconstruction probability of the Dalitz-decay.

By additionally considering detector information, e.g. detector efficiency, particle identification or reconstruction background, a more realistic estimation can be gained, which will be discussed in the next section. Nevertheless these studies only based on MC-true data already indicate a low achievable reconstruction probability of π^0 with the conversion method.

6.5 Combined study with MC-true and reconstructed data

For a realistic estimation of the number of reconstructible π^0 it is necessary to include all detector specific aspects, especially detection efficiency and detector response, and also include the identification and reconstruction routines. Although the exact design and the specifications of all sub-detectors and the complete software and analysis framework are still subject of development (but already on a very advanced level), several aspects can be studied and might also be used for a further improvement of the detector design.

In the simulation all reconstructed tracks are stored in the `GlobalTrack` array. During reconstruction each reconstructed track is matched to a `MCTrack` which makes it possible to use the MC-true information for track selection and the reconstructed data (which consists mainly of a 3-dimensional momentum vector) for the calculation of the invariant mass of π^0 . This allows for realistic estimations of the invariant mass resolution or p_t -coverage. Also exact cuts for the later, reconstructed data-only, analysis will be derived.

Before calculating invariant mass spectra, a short illustration of the small expected reconstruction probability of π^0 via conversion, based on the number of detected electrons (i.e. rings in the RICH detector), is given, as shown in Figure 6.7.

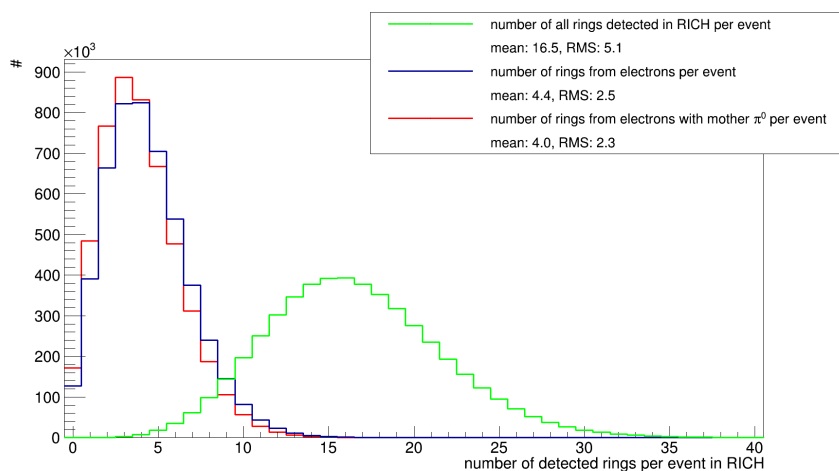


Figure 6.7. – Number of detected rings in the RICH detector for a simulation sample of 5 million central Au + Au collisions at 10 AGeV. Green: all detected rings; blue: rings from electrons, which have also a signal in the STS; red: rings from electrons, stemming from a π^0 , with a signal in the STS.

The green line shows the number of all detected rings per event without any further cuts, yielding in average 16.5 rings in the RICH detector per event. This number includes rings from particles, which have also a signal in the STS and can therefore be completely reconstructed, as also rings from particles, e.g. generated in the last STS stations or between the RICH and the STS, which have no STS information and cannot be reconstructed and used for further analyses.

As it is necessary to have a completely reconstructible track for an afterwards reconstruction of π^0 , the blue line includes only rings from electrons which have a signal in the STS and where the STS track and the RICH track were matched to the same MC-true track (i.e. excluding electrons

generated between STS and RICH or in the last STS stations). This restriction reduces the number of rings to an average of 4.4 per event. By further only taking into account electrons, which originate from a π^0 (either direct or via γ -conversion) this number is slightly reduced to about 4.0 per event.

In roughly half of the events at least four electrons from (any) π^0 are detected, which are necessary to reconstruct a π^0 . These numbers further illustrate the expected small reconstruction probability for π^0 .

By the selection of all those global tracks, which were matched to an electron/positron MC-track coming from a π^0 , it is possible to combine them to π^0 and use the refitted momenta of the four leptons to study several properties of these reconstructed π^0 , e.g. the invariant mass, the transverse momentum or the rapidity distribution.

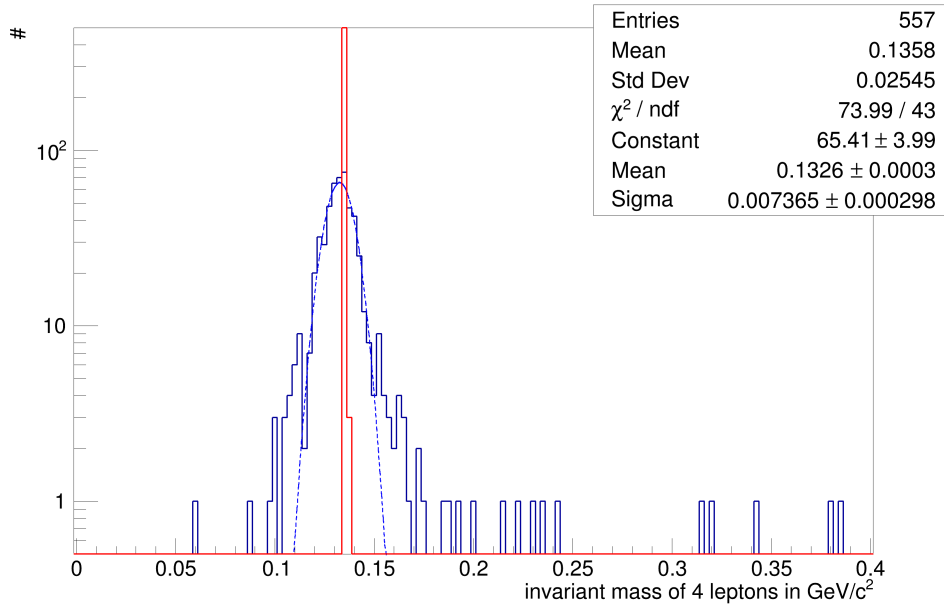


Figure 6.8. – Invariant mass of four electrons/positron from the same π^0 , identified with MC-true data. The blue entries remark the combination with the reconstructed momenta, the red entries the combination with the MC-true momenta. The dashed blue line is a Gaussian fit of the combination with reconstructed momenta.

The invariant mass for all reconstructed π^0 from four leptons is shown in Figure 6.8, including both main decay-channels of π^0 (i.e. $\pi^0 \rightarrow \gamma\gamma$ and $\pi^0 \rightarrow \gamma e^+ e^-$). The blue line was calculated with the refitted momentum and a Gaussian fit applied (dashed blue line). The red line was calculated with the MC-true momenta of the leptons. An additional cut was included for the selection of the leptons, that the origin of all four leptons has to be before $z = 1$ cm to only include decay and conversion inside the target and not within the detector. The results show 557 reconstructed π^0 . As a reference for the number of eventually reconstructible π^0 , numbers from Figure 6.5 are taken for the case of both conversions already happening in the target. This yields a total number of around $1.9 \cdot 10^5$ π^0 (for comparison: summed up around 10^9 π^0 are produced in the target), resulting in a reconstruction probability of nearly 0.2%. But this is still just an upper bound, because the electron identification was done here with the MC-true data. A realistic reconstruction takes into

account the not-ideal identification of electrons and additional selection criteria (opening angle and invariant mass of e^+e^- -pairs), which will further lower the number of reconstructed π^0 .

This plot also clearly shows the broadening of the invariant mass peak due to the limited momentum reconstruction of the involved leptons. A Gaussian fit of the combination with reconstructed momenta yields a mean value of $(132.6 \pm 0.4) \text{ MeV}/c^2$, which only slightly differs from the literature value of $134.98 \text{ MeV}/c^2$. The resulting width of the peak is $(7.4 \pm 0.3) \text{ MeV}/c^2$, which is already better compared to a π^0 reconstruction with an electromagnetic calorimeter via combination of two photons ($\rightarrow \sigma \approx 15 \text{ MeV}/c^2$, as of 2009 [62]). In the real or completely reconstructed data (i.e. without the availability of any MC-true information) the π^0 peak quality is influenced by the combinatorial background (which can be simulated quite well with the event mixing technique, discussed in Section 7.2) and can also be improved by a kinematic fit of the involved photons from the e^+e^- -pair (as it is done in the KFPARTICLE package).

The investigation of the invariant mass spectra can also be done separately for the two main decay-channels $\pi^0 \rightarrow \gamma\gamma$ and $\pi^0 \rightarrow \gamma e^+e^-$, as shown in Figure 6.9. The resulting fitted mean values and widths of the distributions are very similar. The higher reconstruction probability of the Dalitz-decay of π^0 is also visible here by the number of entries in both spectra, yielding 92 (Dalitz) and 360 reconstructed π^0 , which has been already observed in Section 6.4.

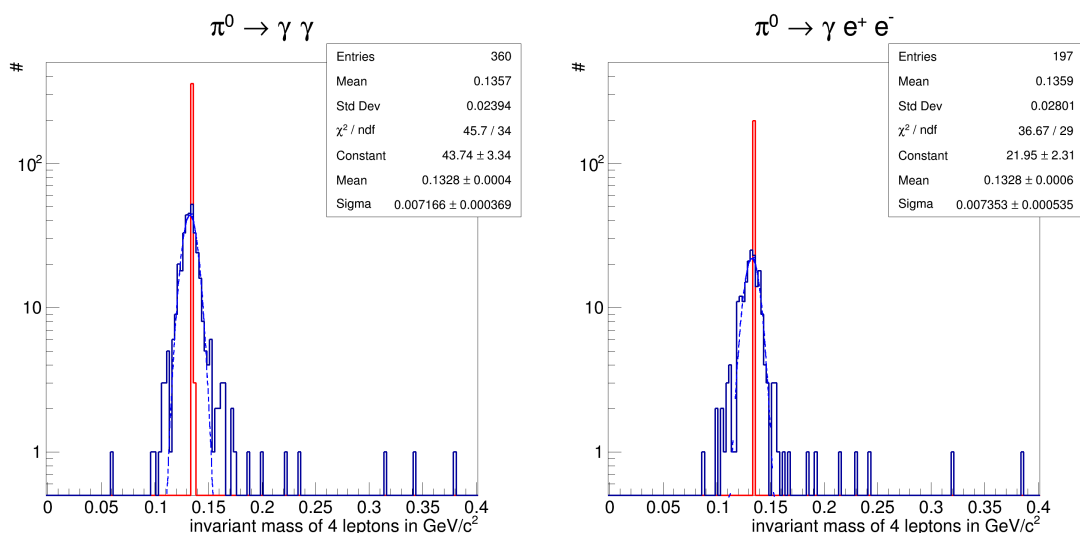


Figure 6.9. – Invariant mass of four electrons/positron from the same π^0 , identified with MC-true data, here separated by the two main decay-channels $\pi^0 \rightarrow \gamma\gamma$ (left) and $\pi^0 \rightarrow \gamma e^+e^-$ (right). The blue entries remark the combination with the reconstructed momenta, the red entries the combination with the MC-true momenta. The dashed blue line is a Gaussian fit of the combination with reconstructed momenta.

Phase-space coverage

When judging the ability of a detector to reconstruct certain particles, one important property is the phase space coverage of the reconstructed particles, which is shown in Figure 6.10 for the above reconstructed π^0 in terms of transversal momentum p_t and rapidity y . The left plot shows the entries from all simulated π^0 within the MCTrack trackbank gained with the MC-true information

of the tracks. The plot in the middle shows all entries gained from the above combined method for π^0 reconstruction and calculated with the reconstructed momenta. The right plot shows the division of both plots to estimate a realistic efficiency coverage of the π^0 reconstruction routine.

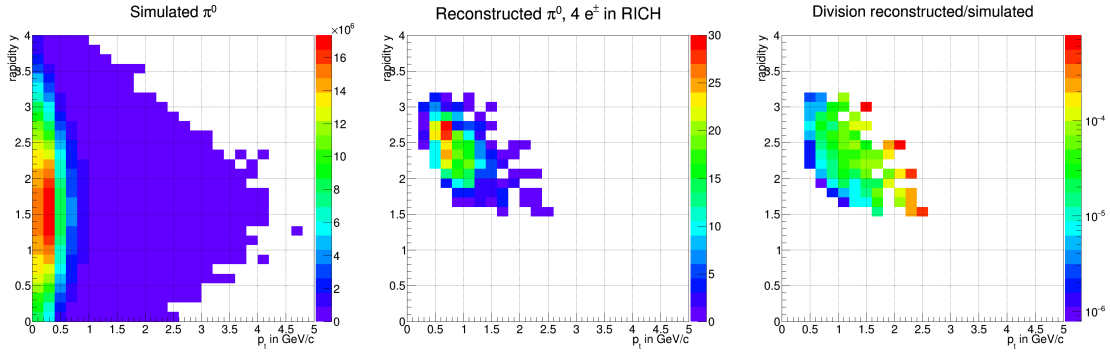


Figure 6.10. – Phase space coverage of simulated and reconstructed π^0 . Left: coverage of simulated π^0 , mid: coverage of all reconstructed π^0 (identified with MC-true data and combined with reconstructed momenta), right: efficiency within phase space, gained by division of the mid and left plot.

The phase space coverage of the reconstructed π^0 clearly differs from the simulated distribution, and has a cut-off towards low rapidities below $y \approx 1.5$ and very low transversal momenta p_t . The limitations in rapidity can be explained by the geometrical acceptance of the CBM detector. Assuming that for low particle masses, including pions ([63]), the rapidity y can be approximated by the pseudo-rapidity $\eta = -\ln \tan \frac{\theta}{2}$, with θ being the emission angle of the particle, the cut-off in rapidity can simply be calculated for the maximum geometrical acceptance with $\theta = 25^\circ$ to $\eta \approx 1.5$, confirming the results from the gained phase-space coverage. An upper limit in rapidity is expected at $y = 3.8$ (with $\theta = 2.5^\circ$), but cannot be seen due to statistics. The magnetic field has just a minor influence on the rapidity coverage of the reconstructed π^0 when using all four leptons for reconstruction. The efficiency towards low transversal momenta is limited by the magnetic field, bending out the leptons of the detector acceptance. A more detailed investigation of the limits of the reconstruction efficiency is given in Section 7.3.

Reconstruction efficiency

In the above presented studies a maximum (possible) number of reconstructible π^0 has been derived. This number was derived by only considering MC-true data for electron identification and combination to a π^0 , but is based on the signals in the detector, and does not include any cuts, which are needed when completely relying on reconstructed data to separate relevant electrons from all other detected particles. These cuts include a cut on the output from the neural network (ANN; uses the properties of the reconstructed ring and the refitted momentum of the assigned particle) for electron identification, a cut on the χ^2 of the fit of the reconstructed momentum of a particle, and a cut on the opening angle and invariant mass of electron-positron-pairs, and will be discussed in detail in Section 6.6. Nevertheless the results from the mentioned chapter will be used here for an estimation of the reconstruction efficiency.

To estimate how many of those π^0 can be reconstructed when considering these cuts, these cuts are also applied to all found π^0 and their decay-leptons here step-by-step. This gives a good indication,

which one of the cuts will have the highest influence on the reconstruction and how many π^0 can be reconstructed with the presented cuts. These results are shown in Figure 6.11 for the three different possibilities of electron identification: using the given ANN, using the properties of the fitted ring (i.e. cuts on ring radius or a - and b -axis, with data extracted from MC-true identified electrons; only mentioned for comparison, will not be used in the final analyses), or using the MC-true information (for reference).

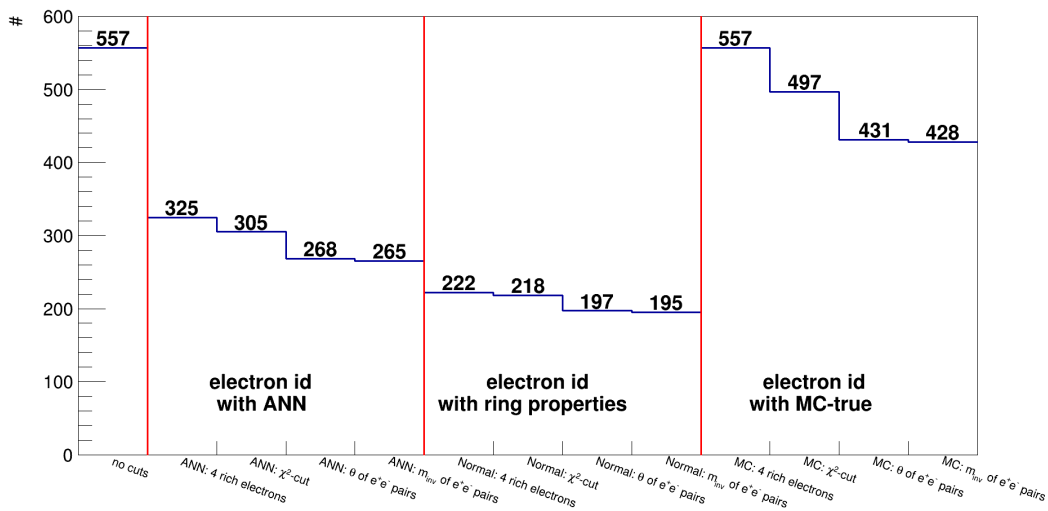


Figure 6.11. – Efficiency studies for the cuts derived in Section 6.6 for three different methods of electron identification (ANN, ring properties, MC-true). The cuts (χ^2 , opening angle θ , and invariant mass m_{inv} of the e^+e^- -pairs) are applied consecutively and their effect on the number of reconstructed π^0 is shown.

The first step is always the electron identification of all four involved leptons. The focused method is the ANN; the ANN is also method of choice for electron identification when only relying on reconstructed data. Electron identification based on the ring properties compares the ring radius/ a -axis/ b -axis of a fitted ring with reference values extracted from distributions only containing electron rings. The identification with MC-true data resembles the input and should therefore contain the same amount as with no cuts applied.

The reconstruction of a π^0 can only be done if all four leptons are correctly identified as an electron, which, as the first applied cut, prevents to reconstruct around 42% of the π^0 , and has therefore the largest influence on the reconstruction efficiency (for comparison: in the case of MC-true electron identification, all three subsequent applied cuts prevent the reconstruction of approx. 23% of the π^0). The further applied cuts (χ^2 , opening angle θ and invariant mass m_{inv} of the e^+e^- -pairs) show only a minor influence on the efficiency, cutting further away around 20% of the remaining π^0 , for the identification with the ANN as also with the ring properties.

The identification with the MC-true values can be used to judge on the efficiency of the three last cuts only (χ^2 , opening angle and invariant mass). The influence of the χ^2 is of the same order as of the opening angle cut, both reducing the number of reconstructed π^0 by about 10%, with the invariant mass cut being negligible for the reconstruction of the π^0 (but it will help to further reduce the background in the resulting spectrum).

As shown in Figure 6.12 (only influence of ANN cut, no further cuts applied) a large fraction of those π^0 , which are rejected by the ANN-cut, cannot be reconstructed because one of the leptons was not identified as an electron or positron (roughly 1/3). In a few cases two or three leptons could not be identified (roughly 8 %).

Based on these calculations it should be possible to reconstruct around 50 % of all π^0 , where all four e^\pm generate a signal in the STS and in the RICH detector (approx. 260 – 270 in the underlying data sample) with these exact cuts, not yet considering the combinatorial background, which can not be avoided in the reconstructed data-only analysis and which influences the complete spectrum.

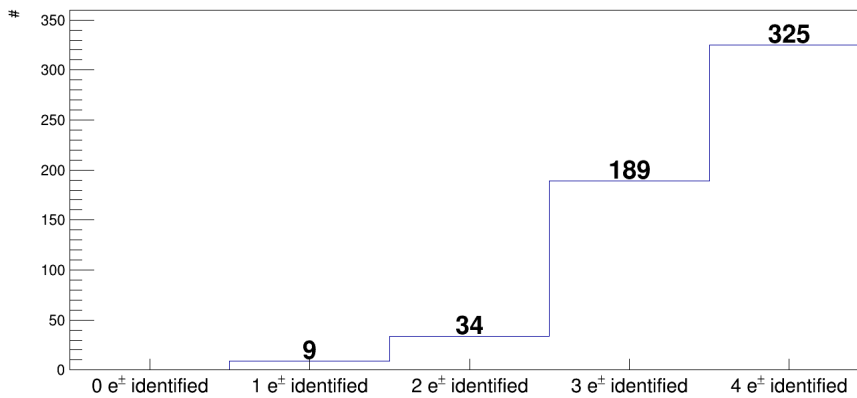


Figure 6.12. – Number of π^0 from which 0, 1, 2, 3, and all 4 electrons are identified based on the ANN and a cut-value of -0.8 . For most π^0 all four leptons are correctly identified with this cut (325). From the non-reconstructible π^0 (totally 232) mainly one of the four leptons was not correctly identified (189).

6.5.1. Conversion in detector

All studies presented here only include conversion within the target itself and not somewhere within the detector material, although the amount of reconstructed π^0 via conversion can be significantly increased when also considering those. Some estimations of this increase can be given with these combined studies of identification with the MC-true data and combination with the reconstructed momenta. Trying to reconstruct π^0 with conversion in the detector (i.e. at least one photon converted in the detector material; the other might also convert in the target) and the standard reconstruction of the momentum yields the invariant mass results from Figure 6.13. The red line represents the combination of the leptons with their MC-true momenta indicating that the selected combinations are real π^0 , whereas for the blue line the reconstructed momenta were used. This broad distribution of invariant masses, with just a small fraction of entries in the π^0 -mass region, clearly shows that for the detailed analyses of π^0 reconstruction with conversion inside the detector, a specific secondary-vertex fitter is necessary, as it is provided for example with the KFPparticle Finder package. But analysis of these reconstructions are not topic of this thesis.

What can additionally be extracted from this plot is, that a factor of around 6 more π^0 can be reconstructed (in comparison to considering only conversion within the target) when including

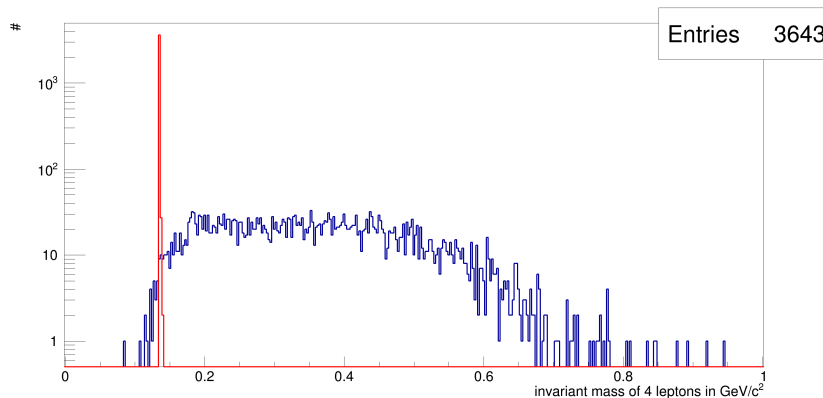


Figure 6.13. – Invariant mass of 4 leptons from the same π^0 calculated with MC-true (red line) and reconstructed (blue line) momenta. Included are only π^0 where at least one of the decay-photons converts in the detector material.

conversion within the MVD and the first layers of the STS detector, and thus shows the significant improvement of the reconstruction efficiency. From consideration of the radiation lengths of the target and the detectors an increase by a factor 3 – 4 was expected (see Section 6.1), which is less than is observed here. The difference is probably due to inaccurate numbers of the radiation lengths in comparison to the implemented detector geometries in the simulation.

A further illustration of this improvement is shown in Figure 6.14, where the origins in z -direction (from MC-true data) of all leptons are depicted, which were used for the above presented reconstruction of π^0 , including conversion only in the target and also conversion within the detector, separated by the two main decay-channels of π^0 . The structure resembles the geometry of the CBM detector, with four stations of the MVD at $z = 5$ cm, 10 cm, 15 cm, and 20 cm, a window shortly after, and several STS stations at $z = 20$ cm, 30 cm, 40 cm, 50 cm, and 60 cm. A very small amount of electrons also stem from photon-conversion within the air between the MVD or STS stations. Overall the largest amount of photon conversion happens in the detector material of the MVD and the STS.

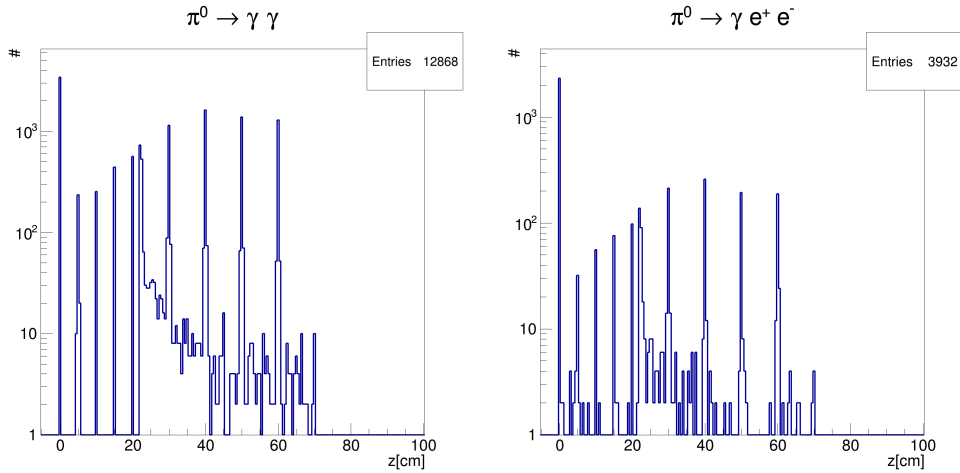


Figure 6.14. – Origins of electrons along the z -axis used for reconstruction of π^0 with the combined method, separated by the two main decay channels $\pi^0 \rightarrow \gamma \gamma \rightarrow e^+ e^- e^+ e^-$ (left) and $\pi^0 \rightarrow \gamma e^+ e^- \rightarrow e^+ e^- e^+ e^-$ (right). Included are conversion of the decay-photons only within the target (\rightarrow reconstruction of 557 π^0) and also within the detector material (\rightarrow reconstruction of 3643 π^0).

6.6 Estimation of cuts for the full reconstruction

When only relying on reconstructed data it is necessary to apply certain cuts to filter out background and consider only relevant candidates for further analyses. For the presented studies on reconstruction of π^0 with the conversion of the decay-photons only a few cuts are relevant:

- The exact cut for the ANN for the identification of electrons within the RICH detector.
- χ^2 -value of the momentum fit of the electrons and positrons. The fit assumes the target position at (0/0/0) as starting point for each track. Particles with their origin somewhere in the detector (e.g. electrons from photon conversion in one of the STS stations) then yield a bad fit result with a bad χ^2 -value. As for the presented analyses only conversion within the target is considered, this cut is necessary to exclude conversion in the detector (and especially exclude all particles with their origin somewhere else in the detector).
- Opening angle of the electron-positron pair from the converted photon. Following the physics of conversion this opening angle should be very small (ideally 0) and is therefore a very good selection criteria for the reconstruction of photons.
- Invariant mass of the electron-positron pair from the converted photon. The invariant mass is correlated to the opening angle, but due to reconstruction uncertainties still relevant to further enhance the selected sample for the combination of electron-positron pairs.

The reconstructed data together with the corresponding MC-true information is well suited to estimate exact cut values. This can be done by comparing e.g. the opening angle or invariant mass distributions (with the values gained from the reconstructed data) of true combinations of electron-positron pairs, identified via MC-true, with false combinations.

The different cuts will be presented in the same order as they are applied in the analysis. The first cut applied is the cut on the ANN output for each ring for the identification of electrons. Afterwards the χ^2 -cut to select electrons with an appropriate reconstructed momentum is applied. The opening angle cut and the invariant mass cut are applied afterwards when combining electrons and positrons to photons.

Cut on the output of the Artificial Neural Network (ANN)

In Section 6.5 the large influence of the electron identification onto the possible number of reconstructible π^0 could be seen. The identification method, which will be used for all analyses here, is the ANN. The ANN uses the properties of the reconstructed ring in the RICH (e.g. radius) and the refitted momentum in the STS of the assigned particle and generates an output value from that. The results of the ANN output for detected electrons (red) and all other detected particles (blue) in the RICH detector can be seen in Figure 6.15.

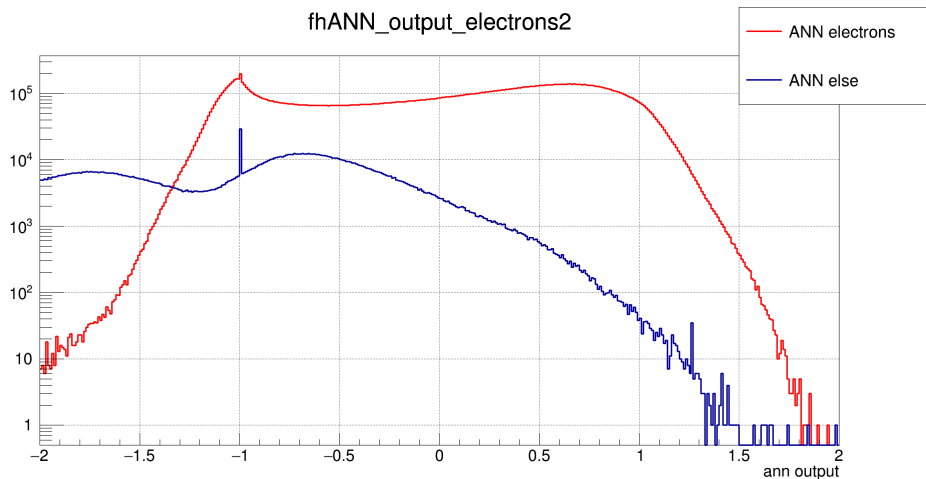


Figure 6.15. – Output from the ANN for electrons (red) and all other particles (blue), which make a signal in the RICH detector. The discrete spike at -1 is artificially generated and is a result from a not reconstructible ring.

The output from the ANN for non-electrons peaks at an output value of around -0.8 (the sharp peak at -1 stems from tracks, where no ring could be reconstructed, and is therefore artificial), whereas the output for electrons peak at -1 and also in the region of 1 with a broad peak. The standard cut for the ANN output used in the simulations is at 0.0 , meaning that one particle is identified as an electron if the output is > 0.0 .

From this result the extraction of an optimum cut value for the ANN is not directly possible. To keep a very pure sample of electrons within the analyses the standard cut of 0.0 can be used, cutting away a very large fraction of all non-electrons, but also of the real electrons, with a fraction of non-electrons of 0.7% remaining in the test-sample. But as the statistics will be very low in the reconstruction, and the background can be very good approximated with the Event Mixing Technique (see Section 7.2), an ANN cut value lower than the standard cut can be used.

Based on the method presented in Section 6.5 the dependency of the number of reconstructible π^0 on the ANN cut, ranging from -1.0 to 0.0 in steps of 0.1 is analysed, neglecting all further cuts.

The resulting numbers are shown in Figure 6.16

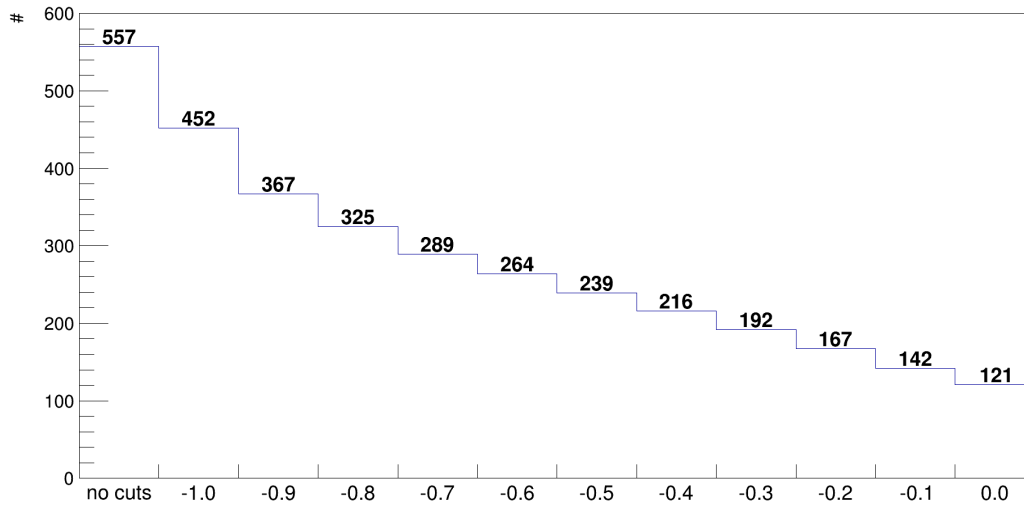


Figure 6.16. – Influence of the ANN-cut value for electron identification on the number of reconstructed π^0 (without application of further cuts). The π^0 were identified and reconstructed with the MC-matched data from the particles detected in the RICH.

The trend is as expected, decreasing nearly linearly towards higher cut-values. A cut-value of -1 is not recommended due to the extremely large amount of background and the small signal-to-background ratio, which both will be created in the data-only driven analysis in Chapter 7, resulting from this cut value. For any other cut-values the number of reconstructible π^0 drops to less than two thirds of the initial ≈ 560 π^0 .

The determination of an exact cut value for the ANN is mainly based on the results from the combined method in Section 6.5 and on the final results from Chapter 7, analysed for different assumed ANN cut values. From all those results an ANN-cut of -0.8 seems to be a good compromise between a good electron identification and a decent amount of background resulting from particles falsely identified as electrons (mainly pions). In the experiment later (when the available amount of event statistics is much larger than available for simulations), this cut will be optimised on the properties of the resulting π^0 -peak and the combinatorial background.

Cut on χ^2 of the particle momentum fit

The χ^2 -cut is important to exclude all tracks with a bad momentum fit as mentioned above. To estimate a reasonable cut the distribution of χ^2 values is studied for several selection criteria as a function of the transversal momentum p_t . These criteria include 1) all tracks detected, which have at least a signal in the STS and in the RICH detector, 2) all electrons stemming from a π^0 (identified via MC-true) via conversion, and 3) all electrons stemming from a π^0 via conversion which already converted in the target. These three distributions are shown in Figure 6.17.

These distributions allow for a rough cut-estimation. All of them are dominated by particles with a momentum fit χ^2 below approx. 5 and according p_t values up to around 1.5 GeV/c. Four

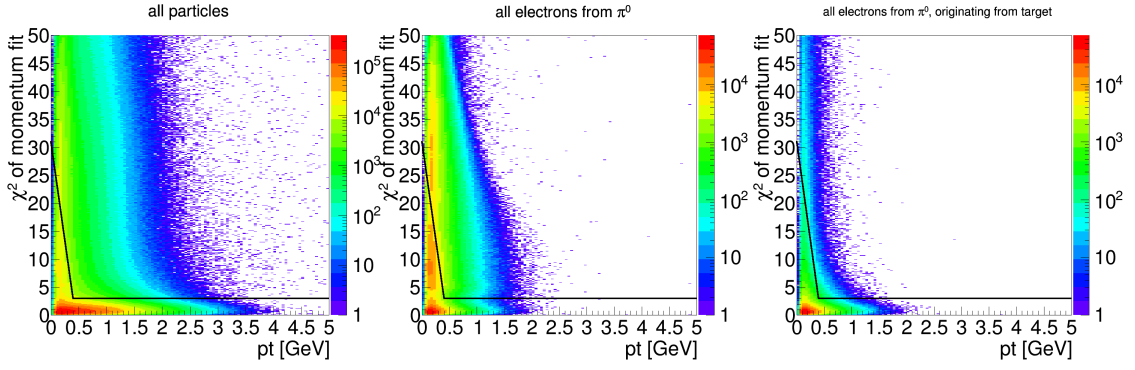


Figure 6.17. – Distribution of χ^2 -values of the momentum fit in dependence of the transversal momentum p_t . Left: distribution for all particles, middle: only for electrons stemming from π^0 via conversion, right: only electrons from π^0 with the conversion happening already in the target. For all three cases a signal in the STS and the RICH detector is required. Identification of electrons is done based on the matched MC-true data. The final cut value is indicated by the black line.

different possibilities for the cut on the χ^2 values of the momentum fit are derived and further investigated, based on the distributions from Figure 6.17:

- $\chi^2 \leq 3$ (i.e. most restrictive)
- $\chi^2 \leq (15 - 30 \cdot p_t)$ for $p_t < 0.4 \text{ GeV}/c$ and $\chi^2 \leq 3$ for $p_t \geq 0.4 \text{ GeV}/c$ (i.e. less restrictive in the low- p_t region than before)
- $\chi^2 \leq (31 - 70 \cdot p_t)$ for $p_t < 0.4 \text{ GeV}/c$ and $\chi^2 \leq 3$ for $p_t \geq 0.4 \text{ GeV}/c$ (i.e. even less restrictive than before) \rightarrow also indicated in Figure 6.17
- $\chi^2 \leq 4$

These further studies of the different cuts include the influence on the number of true and false combinations of e^+e^- -pairs to a photon, which are identified via the MC-true data. In the later analysis the first step is the combination of e^+e^- -pairs to a photon, which makes it important to keep as many true candidates in the sample as possible and at the same time to reduce the number of false combinations. The resulting numbers of true and false combinations for the different χ^2 -cuts together with the combinations without any χ^2 -cut are shown in Figure 6.18.

The results are as expected, with a constant $\chi^2 \leq 3$ cut having the least number of true and false combinations and the third, non-constant cut ($\chi^2 \leq (31 - 70 \cdot p_t)$) keeping most of the combinations. Although the ratio of true and false combinations is worst for this third cut-possibility, this one is chosen to be used in the analysis, as it by far keeps most of the true combinations of e^+e^- -pairs.

As will be shown later, the overall number of entries in the invariant mass spectrum (which can be assumed as π^0 candidates) for the full conversion π^0 analysis will be quite low (in the order of $4 \cdot 10^4$, see e.g. Figure 7.1). This makes it more important to include real signal tracks than to reduce the background. In addition, the background can very closely be approximated with the event mixing technique.

With this chosen χ^2 -cut the number of true combinations of e^+e^- -pairs in the sample gets reduced by $\sim 53\%$, whereas the number of false combinations gets reduced by $\sim 67\%$. One reason, this cut reduces the number of true combinations to this large amount, is that it excludes a lot of those

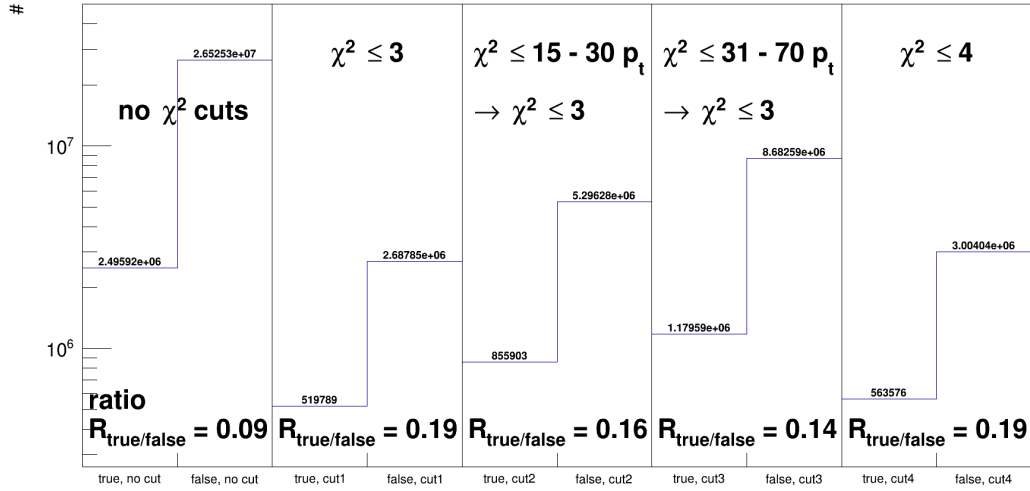


Figure 6.18. – Number of true and false combinations of e^+ and e^- to a photon (identified via MC-true). The numbers are given without any χ^2 -cut and for the 4 different χ^2 -cuts given in the text.

pairs, which have their origin somewhere in the detector material, which was also the goal of this cut.

Cut on the opening angle of e^+e^- -pairs

To derive specific values for the opening angle ϑ cut and the invariant mass cut, correct and false combinations of electron-positron pairs are compared. From the corresponding MC-true data the information can be derived, whether two selected leptons stem from the same photon and can therefore be easily selected.

The resulting distributions for correct (red), false (green), and all (blue) combinations of electron-positron pairs can be seen in Figure 6.19. Here the same requirements as for the χ^2 -cut are used, i.e. the track needs to have a signal in the STS and in the RICH detector, and in addition the derived χ^2 -cut was applied here to all tracks.

The different shape of correct and false combinations is clearly visible, with correct combinations following a sharp exponential behaviour with an additional peak on top (at around $\vartheta \approx 6^\circ$), in contrast to the broad, peak-like structure of the false combinations. The curves for correct and false combinations intersect at an opening angle of 1.5° , making this value a good starting point for further investigations of this cut.

In addition, the effect of the opening angle cut on the resulting transversal momentum p_t acceptance is studied to be taken into account for the exact cut-value. The distributions are shown in Figure 6.20, with the results for true combinations on the left side and for false combinations on the right side. The different behaviour is clearly visible again in these distributions, but also the dependence on p_t is observable. For p_t -values below $0.1 \text{ GeV}/c$ and opening angles below 8° there are no entries due to the minimum acceptance of the RICH detector (of 2.5° azimuthal).

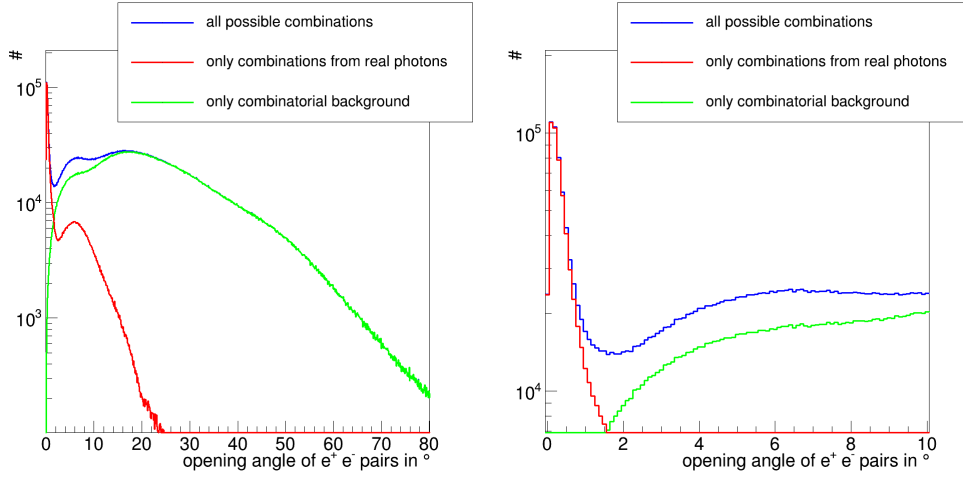


Figure 6.19. – Opening angle distributions of electron-positron pairs. Blue: all possible combinations of electrons and positrons, red: only combinations originating from the same photon, green: only false combinations. Left shows the opening angle range up to 80° , the right picture shows a shorter range up to 10° for better visibility.

Several different cuts on the opening angle were tested:

- $\vartheta \leq 1.8 - 0.6 \cdot p_t$ or $\vartheta \leq 1.5 - 0.5 \cdot p_t$
- constant $\vartheta \leq 1.8^\circ$ or $\vartheta \leq 1.5^\circ$
- $\vartheta \leq 1.5 - 0.5 \cdot p_t$ for $p_t \leq 1 \text{ GeV}/c$, and $\vartheta \leq 1^\circ$ for $p_t > 1 \text{ GeV}/c$
- $\vartheta \leq 1.0 + 1.0 \cdot p_t$ for $p_t \leq 1 \text{ GeV}/c$, and $\vartheta \leq 2^\circ$ for $p_t > 1 \text{ GeV}/c$

The number of true and false combinations of e^+e^- pairs with these different ϑ -cuts added can be seen in Figure 6.21. The most favourable cut is the first one, i.e. $\vartheta \leq 1.8 - 0.6 \cdot p_t$, because it has a relatively large number of true pairs with a very decent amount of false pairs.

The ϑ -cut further reduces the number of true combinations by $\approx 53\%$ and of false combinations by $\approx 99\%$, yielding around 550 000 true combinations in 5 million events, i.e. in average there is one reconstructed photon in every 10th event. Requiring two correct reconstructed photons within one event the presented numbers give a first hint, that only a very small fraction of π^0 might be reconstructed in the full analysis.

Cut on the invariant mass of e^+e^- -pairs

Another small improvement for the selection of true e^+e^- -pairs can be achieved with a cut on the invariant mass of the e^+e^- -pairs. The methods and requirements are the same as for the opening angle cut. The cut on the opening angle was not considered here for these estimations (to get a better impression of the distributions), resulting in the distributions of the invariant mass of e^+e^- -pairs of true and false combinations in Figure 6.22 (top). Remarkable for the distribution of true combinations are several peaks at invariant masses below $0.2 \text{ GeV}/c^2$. These peaks stem from electron-pairs from photon-conversion in the detector material (here: MVD and STS), as can be checked by selecting only electron-pairs originating from the target itself (see Figure 6.22, bottom),

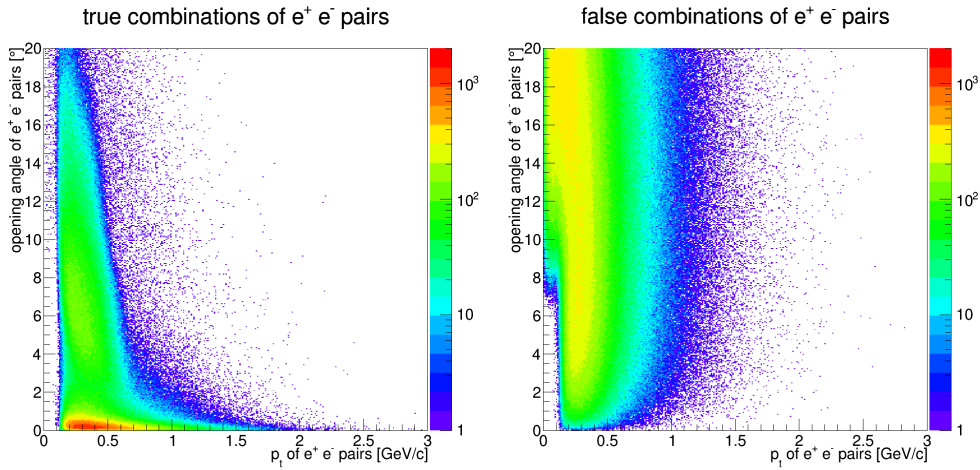


Figure 6.20. – Distribution of opening angle ϑ in dependence of the transversal momentum p_t for all true (left) and false (right) combinations of e^+e^- -pairs, identified via MC-true. For better visualization the z-axis was set to the same range.

causing these peaks to vanish. As the momentum fit assumes the target position as origin, this results in wrong calculated momenta and therefore wrong invariant masses.

From these invariant mass distribution a fixed and constant invariant mass cut of $m_{\text{inv}} \leq 0.03 \text{ GeV}/c^2$ is extracted for the full analysis.

Overview of all applied cuts

To sum up all the gained results for the specific cut-values, a short overview of all calculated cuts for the full analysis is given in Table 6.2.

Table 6.2. – Overview of all cuts applied to each single lepton (χ^2) and to e^+e^- -pairs (opening angle and invariant mass).

Applied cut variable	Value of cut
ANN-cut for electron identification	$\text{ANN} > -0.8$
χ^2 of momentum fit of leptons	$\chi^2 \leq 31 - 70 \cdot p_t$ ($p_t \leq 0.4 \text{ GeV}/c$) and $\chi^2 \leq 3$ ($p_t > 0.4 \text{ GeV}/c$)
Opening angle ϑ of e^+e^- -pairs	$\vartheta \leq 1.8^\circ - 0.6^\circ \cdot p_t$ (p_t in GeV/c)
Invariant mass m_{inv} of e^+e^- -pairs	$m_{\text{inv}} \leq 0.03 \text{ GeV}/c^2$

An additional cut for the combination of two photons is not used (e.g. opening angle between both photons), as this mainly influences the invariant mass region above the π^0 -peak region.

Using the reconstructed parameter p_t for some of the cuts might lead to some uncertainties, but judging from the good results these influences seem to be small or negligible.

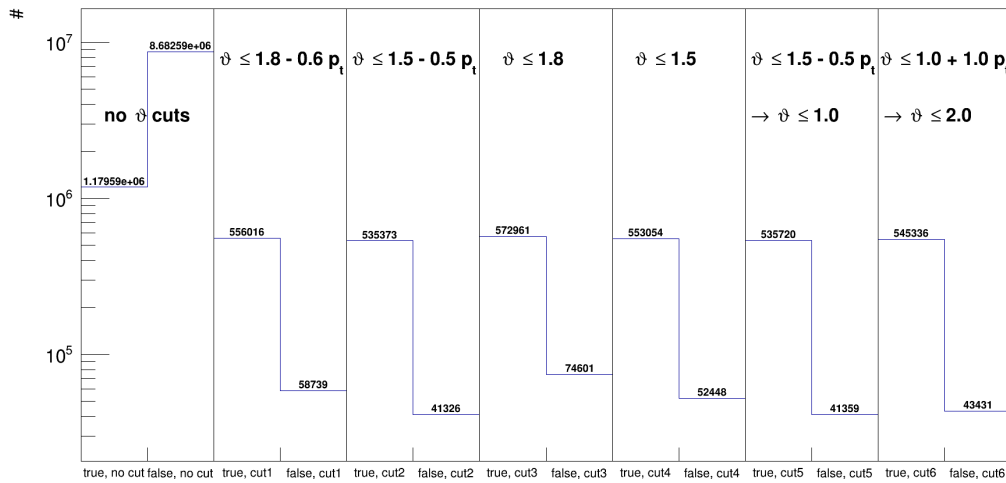


Figure 6.21. – Number of true and false combinations of e^+ and e^- to a photon (identified via MC-true). The numbers are given without any ϑ -cut and also for the 6 different ϑ -cuts given in the text. The above chosen χ^2 -cut was included for all cases here.

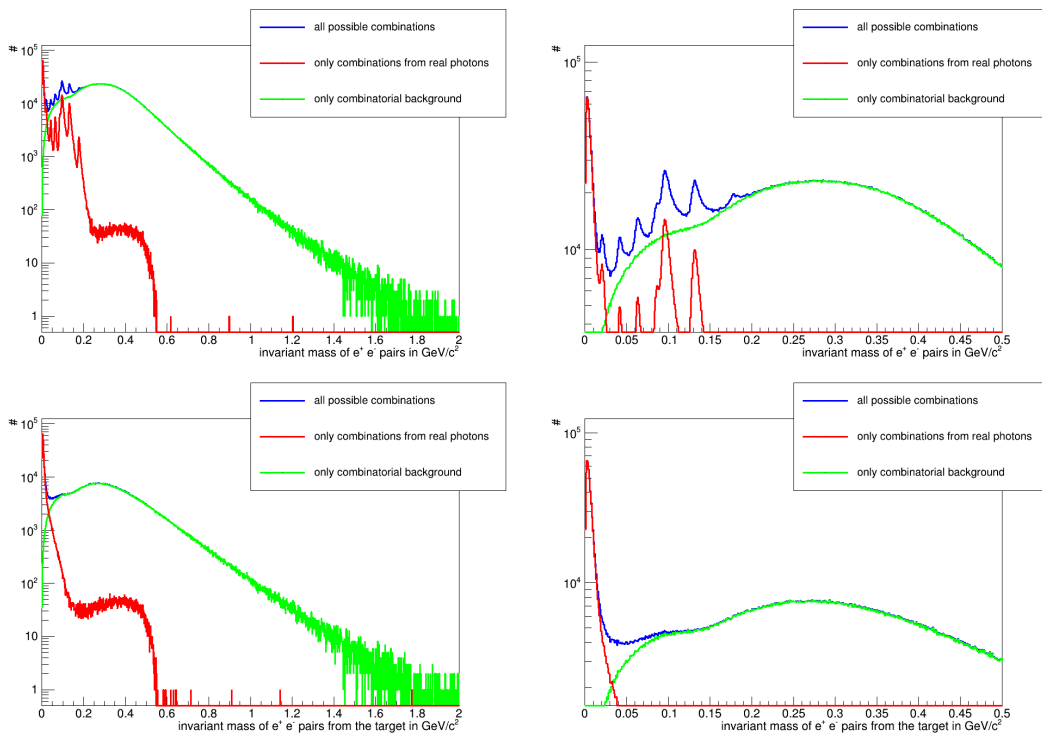


Figure 6.22. – Invariant mass distributions of electron-positron pairs. Blue: all possible combinations of electrons and positrons, red: only combinations originating from the same photon, green: only false combinations. Left shows the invariant mass range up to $2 \text{ GeV}/c^2$, the right picture shows a shorter range up to $0.5 \text{ GeV}/c^2$ for better visibility. Both top pictures show all results, both bottom pictures the results only for leptons originating from the target. The comparison shows that the peaks at low invariant masses stem from photons converting in the detector material.

Results on conversion analysis of dileptons

With the gained knowledge from the previous chapter, especially the derived cut-values, it is now possible to focus on reconstructed data only for the reconstruction of π^0 and η . These cuts are applied to identify and select only electrons and positrons, combine them to photons, and then combine two photons to a π^0 or η . For an estimation and subtraction of the background within the resulting invariant mass spectrum the Event Mixing Technique is used. With this background-subtracted spectrum and with the application of MC-true cuts afterwards several studies can be done, e.g. π^0 -peak quality or phase-space distribution of those π^0 .

The main method to combine electron-positron pairs to photons and photons to π^0 or η is discussed in detail in Section 7.1, and the estimation of the according background with the Event Mixing Technique is presented in Section 7.2. These calculation reveal limitations due to the detector acceptance and the magnetic field, which are shown in Section 7.3. To cope with these limitations it is possible to weaken the strong requirement of all four leptons from a π^0 or η being detected in the RICH detector to only three detected leptons. Results from according studies are presented in Section 7.4. All studies are done with input from UrQMD, which has a non-homogeneous distribution of generated particles within the phase-space. To create a homogeneous distribution the boxgenerator is used for input, and the resulting acceptance within the phase-space coverage is calculated in Section 7.5.

7.1 Studies only based on completely reconstructed data

After applying the cut values, it is possible to do the reconstruction without the use of MC-true data. This resembles the same procedure as under real circumstances in the future. The only cut, which has not been determined explicitly, is the cut applied to the ANN output for the

electron identification, as the influence on the background contributions can not be estimated and is therefore part of the following studies.

In Section 6.5 the reconstruction is based on MC-matched tracks of the global tracks, i.e. on tracks which make a signal in the detector, but the identification is done with the matched MC-true data. In this chapter the identification of electrons and photon-candidates is based only on information derived from the detector response, i.e. with the ANN for electron identification and the cuts applied to the reconstructed and refitted momenta shown in the previous chapter for a further selection of photon-candidates. The MC-true data is only used for a judgement of the reconstructed π^0 -candidates to separate the different sources of background.

The reconstruction of π^0 is divided into three main steps:

1. In the first step all particles identified as electrons with the RICH detector (TRD and TOF are not considered for these analyses) are selected from the GlobalTrack array. This is done with a predefined ANN, which uses the properties of the Cherenkov ring from the RICH detector and the refitted momentum to check whether it is an electron. Every track, for which the ANN output is above a certain cut value, is assumed to be an electron. The refit of the momentum can be done either only with the standard refit (which assumes the pion mass for each particle) or with an additional fit iteration, which assumes the mass of an electron. Additionally, the cut on the resulting χ^2 of the momentum fit is applied in this step.

To cover and investigate the influence of the additional fit-iteration and of the χ^2 -cut, a total of four different cases for all possibilities will be analysed, but with the main focus on the reconstruction with χ^2 -cut and with the additional fit-iteration.

2. After selection of all identified electrons, they are combined to photons by applying the cuts on the opening angle and the invariant mass of the e^+e^- -pair and also checking for opposite charges of both particles. These photons consist of real and false photons, i.e. the combined e^+ and e^- stem from the same photon (\rightarrow real) or from two different photons or other particles (\rightarrow false). A differentiation is not possible.
3. If at least two photons were reconstructed within one event, all possible combinations of photons are calculated, without any further cuts.

As η has partially the same decay-channels as π^0 , especially the main decay-channel into two photons, also η are reconstructed with the introduced method. Nevertheless, the amount of reconstructed η is expected to be very small due to the small number of generated η and the small branching ratio for $\eta \rightarrow \gamma\gamma \approx 39\%$.

For the first results four different cases were considered: with and without the additional fit iteration of the momentum, and with and without the χ^2 -cut on the fit-result of the momentum. The four resulting invariant mass spectra are shown in Figure 7.1.

Although the additional fit iteration and the χ^2 -cut have a minor influence on the reconstructed spectra, both will be used for the analyses, at least to include realistic assumptions and to improve the accuracy of the results, especially when the number of simulated events will be increased.

The final resulting invariant mass spectrum from four leptons with all applied cuts as derived above and with the additional fit iteration can be seen in large in Figure 7.2. The small number of approximately 42 000 entries already indicates a very small reconstruction efficiency for π^0 with

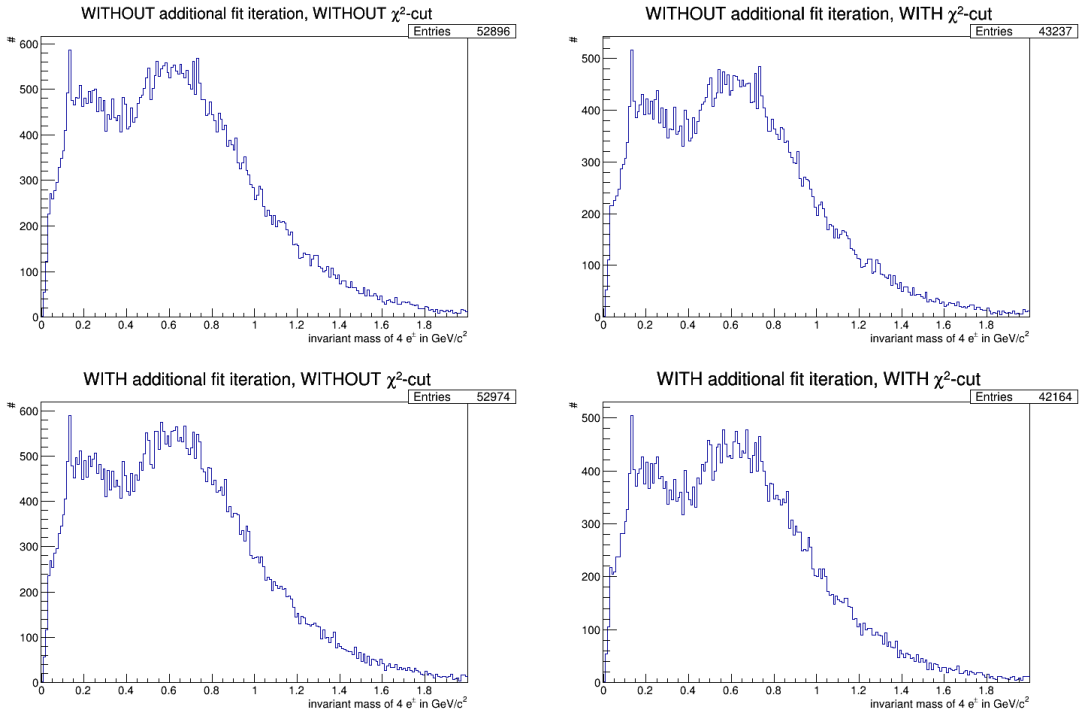


Figure 7.1. – Reconstructed invariant mass spectra for four different cases of applied cuts: without and with an additional fit iteration of the momentum fit (top/bottom), and without and with a cut on the χ^2 of the momentum fit (left/right). For better visibility the binwidth was set to $10 \text{ MeV}/c^2$.

the conversion method (for comparison the number of 10^8 generated π^0 during the simulation can be used). Nevertheless a peak at the π^0 invariant mass of $0.135 \text{ GeV}/c$ can be recognized despite the large variances of the spectrum and the large amount of background entries.

Counting the number of events in the complete simulation sample, in which at least one photon could be reconstructed, yields a value of roughly 450 000 events, but only in 45 000 events at least two photons could be reconstructed and could therefore be used for this analysis (i.e. in $4.5 \cdot 10^6$ events or 90 % of the data no photon was reconstructed with the combination of STS and RICH only). The main restriction here is the cut on the opening angle of the e^+e^- -pair. Neglecting the χ^2 -cut just increases the numbers of events to 515 000 and 55 000, respectively. The higher number of possible combinations of two photons, derived from the number of events with at least two reconstructed photons, in comparison to the number of entries in the spectrum is a result of multiple usage of a lepton for the reconstruction of photons. For the combination of two photons to a π^0 or η all these cases have to be excluded, where one of the leptons contributed to the reconstruction of both photons from the same mother particle.

There are several different contributions to the reconstructed spectrum, which can be separated by applying dedicated cuts to the MC-matched tracks of the leptons. These contributions are mainly:

1. Both e^+e^- -pairs were correctly matched together and both pairs stem from a photon. Also both photons stem from the same mother particle.
2. Both e^+e^- -pairs were correctly matched together and stem from a photon. But both photons

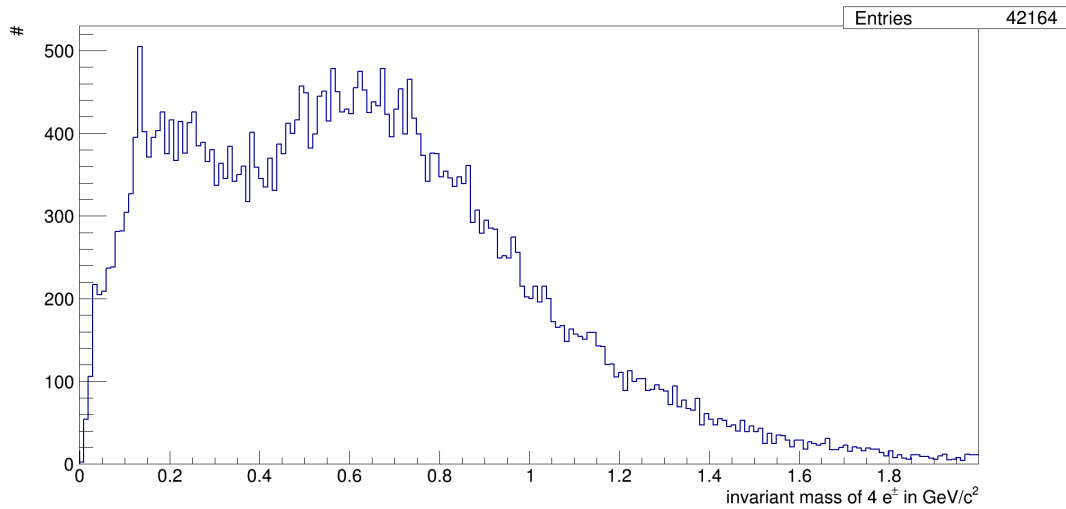


Figure 7.2. – Invariant mass spectrum for the combination of four leptons using only reconstructed data with the cuts derived in Section 6.6. A peak at the π^0 mass can clearly be recognized. The binwidth here is $10 \text{ MeV}/c^2$.

stem from different mother particles.

3. Both e^+e^- -pairs were correctly matched together, but one pair stems from a γ and one pair stems directly from a π^0 .
4. Both e^+e^- -pairs were correctly matched together, and both stem directly from a π^0 .
5. One e^+e^- -pair was correctly matched together and the other one was not.
6. Both e^+e^- -pairs were not correctly matched together.
7. (Same as case 3, but with the additional requirement, that the γ stems from from the π^0 , i.e. this should only contain Dalitz-decays of π^0 . This case is completely contained in case 3 and was just included to derive a π^0 -peak.)

The complete spectrum and all mentioned contributions (rebinned by a factor of 2 from Figure 7.2 for better visibility, resulting in a bin width of $20 \text{ MeV}/c^2$) are shown in Figure 7.3 and allow for a precise judgement of the different contributions to the background.

This picture clearly shows that the largest contribution to the background is from false combinations of two correctly reconstructed photons (i.e. the e^+e^- -pairs were correctly matched together, stemming from the same photon; will be mentioned as ‘real photons’) stemming from different mother particles, e.g. from two different π^0 (green line). One additional large contribution comes from the combination of one real photon and one ‘false’ photon, i.e. the combined e^+ and e^- stem from different mother particles (pink line). Of the same order of magnitude is the contribution from combinations, where one e^+e^- -pair is correctly matched stemming from a photon and another e^+e^- -pair being correctly matched and stemming directly from a π^0 (light blue line). This last case also contains π^0 from the Dalitz-decay. Further, but very small contributions come from the case where the combined e^+ and e^- stem from the same mother particle, which is in both pairs a π^0 (olive-green line). A last remarkable contributions stems from a false combination of both e^+e^- -pairs, forming mainly a narrow peak at low invariant masses (red line).

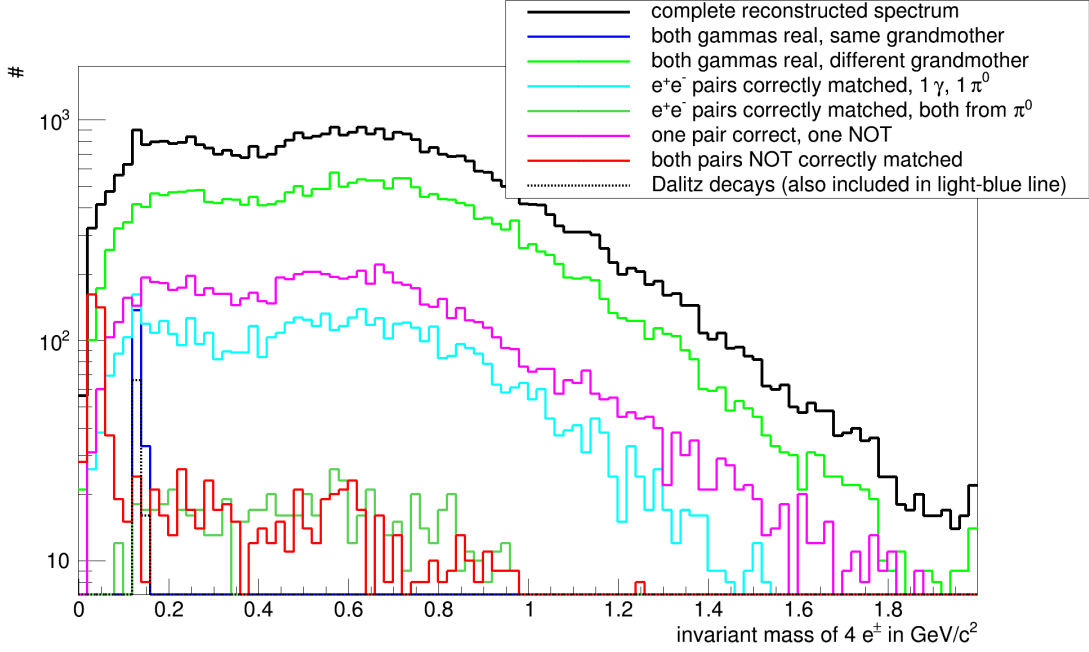


Figure 7.3. – Invariant mass spectrum for the combination of four leptons using only reconstructed data with the cuts derived in Section 6.6. In addition several MC-cuts based on the matched MC-true data were applied, which were specified before, depicted in different colours. Here the binwidth is $20 \text{ MeV}/c^2$ for better visibility.

The combination of two real photons, which stem from the same mother particle (blue line, only decay channel $\pi^0/\eta \rightarrow \gamma\gamma \rightarrow e^+e^-e^+e^-$), and therefore resemble signal and not background, results in the expected π^0 peak (178 entries) and also very few entries (7) at the η invariant mass. Fitting only this π^0 peak with a Gaussian (before rebinning, i.e. with a bin width of $2.5 \text{ MeV}/c^2$) yields a mean value of $(133.2 \pm 0.5) \text{ MeV}/c^2$ and a peak width of $(6.0 \pm 0.5) \text{ MeV}/c^2$, which already indicates a very good reconstruction quality. Fitting the π^0 -peak from Dalitz-decays (which has 87 entries) with a Gaussian yields slightly worse results with a mean value of $(133.1 \pm 1.1) \text{ MeV}/c^2$ and a peak width of $(8.4 \pm 1.3) \text{ MeV}/c^2$.

Comparing the ratio of reconstructed π^0 for both decay-channels ($\pi^0 \rightarrow \gamma\gamma$ and $\pi^0 \rightarrow \gamma e^+e^-$) with the ratio of the branching-ratios of both decay-channels (98.8% and 1.2%), this clearly shows a significant higher reconstruction probability of the Dalitz decay-channel than for the $\gamma\gamma$ decay-channel. The reason is that only one photon has to convert for the Dalitz decay, instead of two photons.

The total number of 265 reconstructed π^0 here perfectly matches the expected number derived in Section 6.5, indicating that the results are correct. In addition this shows, that the extraction of precise cut-values in Section 6.6 is sufficient to include only conversion within the target and not within the detector (because the combined studies only include conversion before $z_{\text{start}}(\text{electrons}) < 1 \text{ cm}$, i.e. in the target).

The large fraction, where both γ were correctly reconstructed but wrongly combined (green line, approx. 59% of all entries; in addition correctly reconstructed photons are also contained in other background contributions), indicate that the photon reconstruction works very reliable, and also

the assignment of two leptons to the same mother particle (mainly γ , but also π^0 , η or other, not investigated sources).

To be able to adequately judge on the quality of the π^0 peak without any MC-true cuts, the background is approximated with the Event Mixing Technique and afterwards subtracted from the spectrum, leaving in only real signal and the variations of the spectrum. This will be discussed in the next chapter. In addition the calculation and subtraction of the background opens up the possibility for further detailed studies of the result, e.g. peak position and peak width of the π^0 peak based on data only, signal-to-background ratio, or estimated number of reconstructed π^0 . Therefore most of the results will be discussed in the related chapter and not within this chapter.

7.2 Background forming with the Event Mixing Technique

The presented invariant-mass spectra consist to a large fraction of background, stemming for example from false combinations of e^+ and e^- to a photon and false combinations of two photons to a π^0 or η . This background can be successfully simulated with the Event Mixing Technique (see e.g. [64, 65]), which is a standard tool for background estimations. There is also a proposal for a similar technique, which only uses particles from within one event, claiming that the combination of particles from different events might be problematic ([66]). Due to the very low statistics of electrons or photons within one event this alternative approach is not sufficient to estimate the background here, but it might be interesting when going to higher beam-energies and therefore higher multiplicities per event.

The Event Mixing Technique (EMT) is based on the combination of particles (here: two photons) from different events and therefore only forming background events and no signal events. Usually the Event Mixing Technique is used for two-body decays, which also includes Dalitz-decays as the e^+e^- -pair can be treated as an imaginary photon. Afterwards the background invariant mass spectrum can be scaled to the reconstructed invariant mass spectrum and subtracted, leaving only entries in the signal peak(s) and variations of the spectrum. Statistical variations of the calculated background can be minimized by considering photons from a larger amount of events for combination. Important for an adequate description of the background with the Event Mixing Technique is the application of the exact same cuts as used for the signal reconstruction, i.e. χ^2 , opening angle and invariant mass of the e^+e^- -pairs. This is achieved by using the individual photons after reconstruction procedure, which already include all applied cuts.

The Event Mixing Technique was implemented the following way:

1. Accumulate all reconstructed photons from the standard reconstruction from e^+e^- -pairs from N events in a dedicated array. Here $N = 250$ events were used each time. (Taking only one electron from each event has also been evaluated, but this can not completely describe all processes contributing to the spectrum, e.g. two correctly reconstructed photons from different π^0 .)
2. After photons from these N events were stored, all possible combinations of two photons are calculated, with the restriction that the combined photons stem from two different events. After all possible 2-photon combinations are built, continue with step 1 for the next N events and repeat for the remaining event sample.

3. Afterwards the total background spectrum is scaled to the reconstructed spectrum based on a fit of the ratio between both spectra with a constant function (limited to the range of $0.2 \text{ GeV}/c^2 < m_{\text{inv}} < 1.0 \text{ GeV}/c^2$ to exclude regions which contain signal events or only a small number of entries).

Using this approach the same conditions are applied to the reconstruction of signal and background events. Nearly all possible contributions to the background in the reconstructed invariant mass spectrum are covered, e.g. false combinations of e^+ and e^- to a photon or false combinations of two (false and/or correct) photons to a π^0 or η . Only the cross-combination of leptons is not included, resulting in additional peaks in the background-subtracted spectrum, as discussed later. A slight different approach for event mixing was also tested by directly combining e^\pm from four different events, but could not reproduce the exact shape as this does not resemble the identical conditions (for example the use of correctly reconstructed photons).

The resulting spectrum from the event mixing (blue, already scaled) together with the reconstructed spectrum (red) can be seen in Figure 7.4 (left). The right side shows the background-subtracted spectrum with a double Gaussian fit of the π^0 peak and another peak located at very low invariant masses.

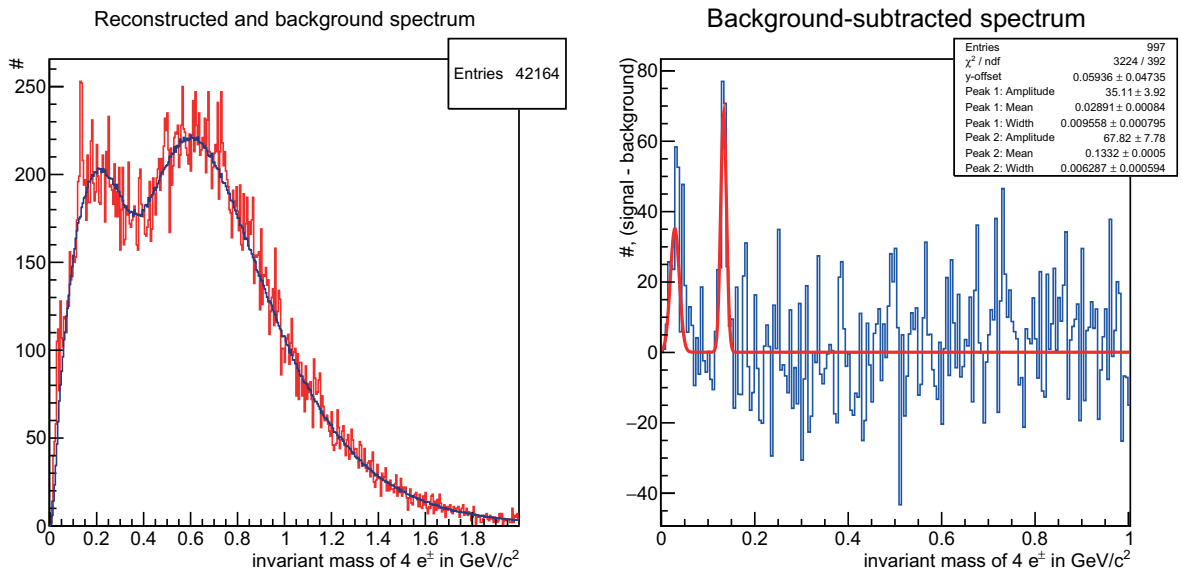


Figure 7.4. – Left: reconstructed invariant mass spectrum from the combination of 4 e^\pm (red) and the scaled background calculated with the event mixing technique (blue). Right: background-subtracted invariant mass spectrum (blue) with a double Gaussian fit for the π^0 -peak and the peak at very low invariant masses. The binwidth here is $5 \text{ MeV}/c^2$.

The fit result for the π^0 peak shows a mean value of $m_{\text{inv}} \approx (133.2 \pm 0.5) \text{ MeV}/c$ and a width of $\sigma \approx (6.3 \pm 0.6) \text{ MeV}/c$. The first peak at very low invariant masses of around $30 \text{ MeV}/c^2$ stems from cross-combination of electrons from two different π^0 , i.e. both (falsely reconstructed) photons consist of electrons from two different mother particles. In this case the resulting combination is then done with each time two electrons from two π^0 . This contribution is also visible in Figure 7.3 (red line).

Although the mean position of the π^0 peak does not precisely match the theoretical value, the

overall spectrum already shows very good reconstruction possibilities with the presented methods, as the peak is clearly identifiable above background.

The main problem here is the limited statistics of $5 \cdot 10^6$ simulated events given the very low reconstruction efficiency of π^0 , causing large statistical fluctuations of the resulting spectrum and just a few (< 300) entries in the π^0 -peak region.

With an adequate fit of the π^0 -peak it is possible to make some detailed studies, which include estimation of the signal-to-background ratio, estimations of the number of reconstructed π^0 , and also the distribution for various p_t -ranges.

The number of reconstructed π^0 within this peak is calculated within the 3σ -region around the mean of the peak (covering 99.7% of the peak area) based on the fitted curve, by taking the corresponding bins of $m_{inv, mean} \pm 3\sigma$ and then adding up the entries of all bins from the background-subtracted spectrum (compare Equation 7.1). For an estimation of the signal-to-background ratio the number of background events is needed, which is calculated by taking the same range and adding up all entries from the scaled background from EMT (compare Equation 7.2).

$$(\text{signal}) = \sum_{\text{bin}(m_{inv}-3\sigma)}^{\text{bin}(m_{inv}+3\sigma)} (\text{background-subtracted spectrum}) \quad (7.1)$$

$$(\text{background}) = \sum_{\text{bin}(m_{inv}-3\sigma)}^{\text{bin}(m_{inv}+3\sigma)} (\text{background spectrum from EMT}) \quad (7.2)$$

Estimating errors of the results is based on the variations of the background-subtracted spectrum above an invariant mass of $0.2 \text{ GeV}/c^2$, where no signal peak occurs and the spectrum is expected to be centered around 0. Therefore the relevant bins are projected onto the y-axis and the result is fitted with a Gaussian. The resulting σ -value of the Gaussian fit is then taken as the mean error per bin of the background-subtracted spectrum. The corresponding distribution of the projection together with the fit result is shown in Figure 7.5.

The resulting mean value of $x_0 \approx 0.75$ illustrates that the background-subtracted spectrum is centred around 0 and confirms that the calculated background from EMT describes the background very well. The width of $\sigma \approx 6.5$ is used as error for each bin of the background-subtracted spectrum.

Following the above description for the estimation of the number of reconstructed π^0 , which is depicted in Figure 7.6, results in 239 ± 52 reconstructed π^0 (with the overall error from 8 summed up bins being $8 \cdot 6.5 = 52$). For comparison the integral over the function fitted to the background-subtracted distribution is calculated within the same range, yielding about 212 ± 15 reconstructed π^0 , which is comparable to counting the entries in the histogram.

This number can now be compared to the number of 265 π^0 , which are contained in this spectrum and which were identified with MC-true data as shown in Section 7.1, being in good agreement, although the reconstructed numbers slightly underestimate the amount, but still within errors.

In order to estimate the signal-to-background ratio, the number of background events in the peak

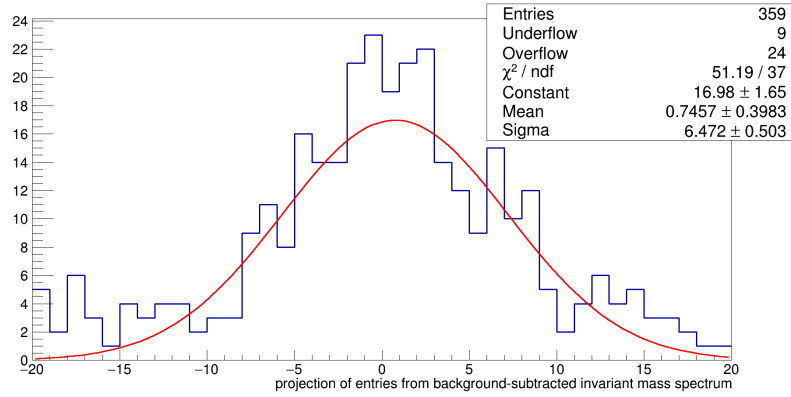


Figure 7.5. – Projection of all entries from the background-subtracted invariant mass spectrum between $0.2 \text{ GeV}/c^2$ and $2 \text{ GeV}/c^2$ onto the y-axis ('number of entries'). The resulting distribution is fitted with a Gaussian, yielding a mean value of $x_0 \approx 0.75$ and a width of $\sigma \approx 6.5$. The width is interpreted as error per bin in the background-subtracted invariant mass spectrum.

region must be determined. Summing up the entries from the EMT background, yielding 1429 entries, the signal-to-background ratio can be estimated to (error calculated by error propagation):

$$S/B\text{-ratio} = \frac{N_{\text{signal}}}{N_{\text{signal}} + N_{\text{background}}} = \frac{239 \pm 52}{1668} \approx (14.3 \pm 2.7) \% \quad (7.3)$$

Here, the error of the background was assumed to be negligible due to the higher statistics in the EMT sample.

The small number of 239 ± 52 reconstructed π^0 show the very small reconstruction probability (around $8.6 \cdot 10^8 \pi^0$ were generated within the target), but the signal-to-background ratio within the 3σ region of $(14.3 \pm 2.7) \%$ illustrates a good distinguishable π^0 -peak. One reason for the low probability is the conversion probability within the target of about 2.9% ([52]), which sums up to $8.4 \cdot 10^{-2} \%$ for both decay-photons converting in the target. In addition the different phase-space coverages of generated and reconstructed π^0 , as shown in Section 6.5, strongly contribute to the low reconstruction probability.

Separating the entries in the signal spectrum by the individual p_t -bins gives further details about the efficiency of this method. The invariant mass spectra (in blue) together with the calculated background from EMT (red) can be seen in Figure 7.7 for four different p_t -ranges between $p_t = 0 \text{ GeV}/c$ and $p_t = 2 \text{ GeV}/c$ in steps of $0.5 \text{ GeV}/c$.

The shape of all four spectra is very different, as is the individual statistics in each p_t -bin. Nevertheless, the calculated background from EMT always fits nicely to the reconstructed spectra in each p_t -range. Comparing the scaling factors of the EMT background for the complete spectrum and for the p_t -differentiated spectra (see Table 7.1) show nearly the exact same values, which illustrates that the EMT, as implemented here, works reliable.

The corresponding results for the background-subtracted invariant mass spectra are shown in Figure 7.8. Contributions to the π^0 -peak mainly occur within the range $0.5 \text{ GeV}/c < p_t < 1.5 \text{ GeV}/c$. The spectra for $p_t < 0.5 \text{ GeV}/c$ and $p_t > 1.5 \text{ GeV}/c$ are nearly flat with mean variations

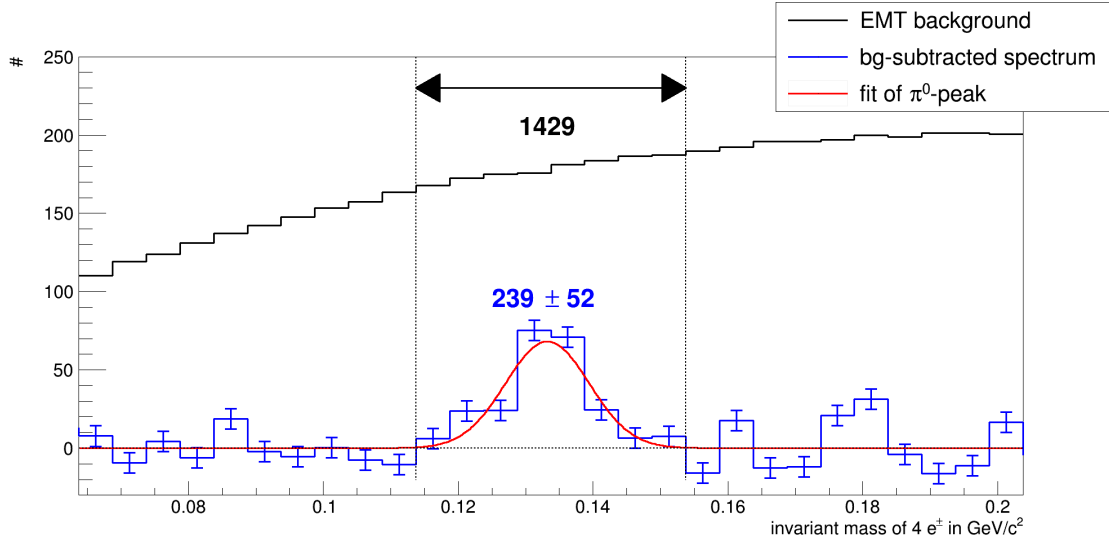


Figure 7.6. – Background from EMT (black) and background-subtracted invariant mass spectrum (blue) with a Gaussian fit of the π^0 peak (red). For counting the bins containing the 3σ -region of the fitted peak are used, marked by the vertical lines, resulting in 239 entries in the π^0 -peak and 1429 entries in the background spectrum.

Table 7.1. – Scaling factors for the background calculated with EMT to the reconstructed invariant mass spectrum. Factors are shown for the complete spectrum as also for p_t -separated spectra. The nearly identical numbers show very similar contributions to the reconstructed spectrum and to the background for different p_t -ranges.

	complete spectrum	p_t -bin 1	p_t -bin 2	p_t -bin 3	p_t -bin 4
scaling factor sf	0.00666	0.00679	0.00657	0.00641	0.00534
error Δsf_{RMS}	0.00004	0.00006	0.00006	0.00010	0.00020

in the order of 5.2 and 2.1 (derived as above by projecting all entries onto the y-axis and fitting with a Gaussian).

The spectra are fitted with different functions. For the first p_t -bin ($p_t < 0.5 \text{ GeV}/c$) and for the last bin ($p_t > 1.5 \text{ GeV}/c$) a constant function was used as no signal peak can be seen and the spectra are expected to be flat for that reason. The resulting mean values of the fits are nearly zero, confirming this expectation. Both spectra containing signal entries in the π^0 -mass region are fitted with a sum of a constant and a Gaussian, resulting in a good description of the spectra. The fitted π^0 -peak positions of $(132.5 \pm 0.1) \text{ MeV}/c^2$ and $(136.9 \pm 0.1) \text{ MeV}/c^2$ show slight deviations from the theoretical value of $134.98 \text{ MeV}/c^2$. Figure 7.9 shows the two relevant invariant mass spectra (blue), which include a π^0 -peak, together with the fit results (red) and vertical lines depicting the bins, which were used for the counting of π^0 .

Counting the number of π^0 in both relevant p_t -ranges yields around 165 ± 73 reconstructed π^0 for $0.5 \text{ GeV}/c < p_t < 1.0 \text{ GeV}/c$ and 72 ± 34 reconstructed π^0 for $1.0 \text{ GeV}/c < p_t < 1.5 \text{ GeV}/c$. The integral of the according fit functions yield nearly the exact same values with 159 ± 3 and 70 ± 2 (the errors of the integral of the fit functions are calculated based on the errors of the fit results).

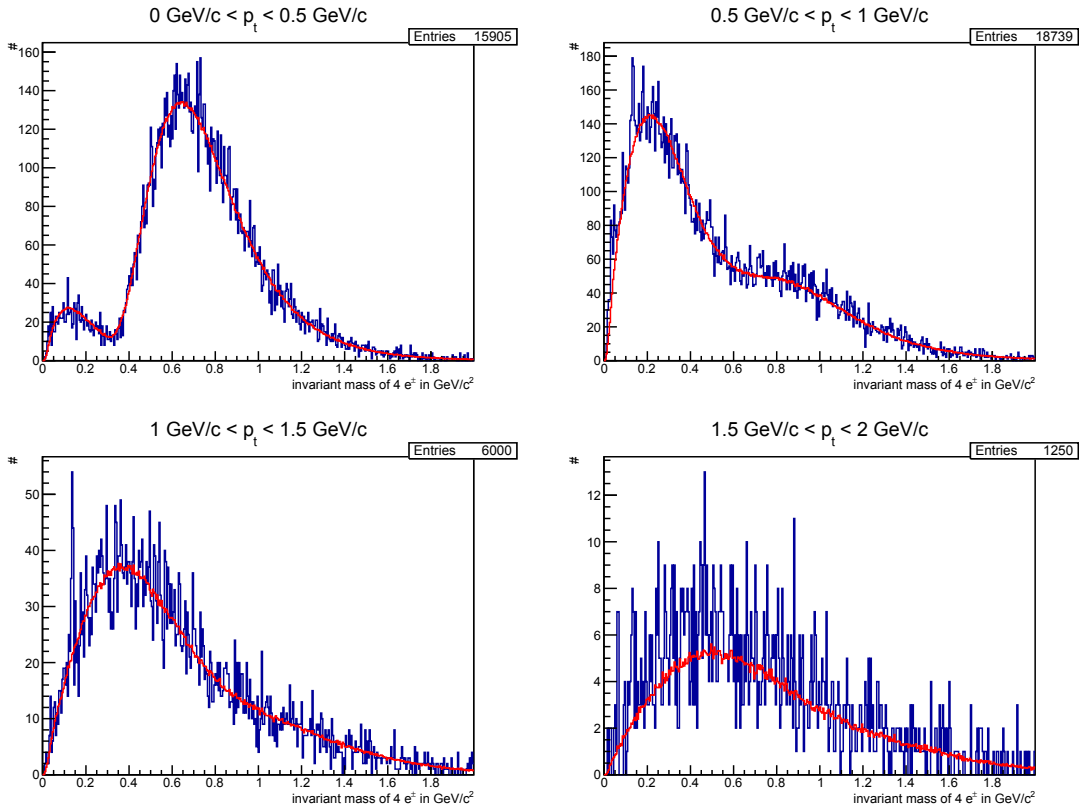


Figure 7.7. – Invariant mass spectra (blue) for different p_t -ranges between $p_t = 0 \text{ GeV}/c$ and $p_t = 2 \text{ GeV}/c$. In red the scaled background spectra as calculated with EMT are shown. In each case the background fits very good to the signal spectrum.

An partial improvement of the signal-to-background ratio can already be expected from Figure 7.7. For an exact calculation the number of entries in the background spectrum was counted to 1004 for the second p_t -range and 130 for the third p_t -range, again with negligible errors. From this the signal-to-background ratios are computed to $(14 \pm 5) \%$ and $(36 \pm 11) \%$, compared to 14.3% for the full p_t -range fit.

For all above discussed calculations an ANN cut of -0.8 for the electron identification was used. Dedicated studies show that a stronger ANN cut of -0.5 or even 0.0 might slightly improve the quality of the resulting π^0 -peak (in terms of peak position and peak width) but always on the cost of number of reconstructed π^0 . As the available amount of statistics ($5 \cdot 10^6$ events) is fairly low in this analysis (it compares to only a few minutes of later data taking), this very low cut of -0.8 is recommended. In case of the availability of a larger amount of statistics (at least around ten times more) a stronger cut can be helpful to decrease the amount of false identified electrons, reduce the background, and improve the π^0 -peak quality.

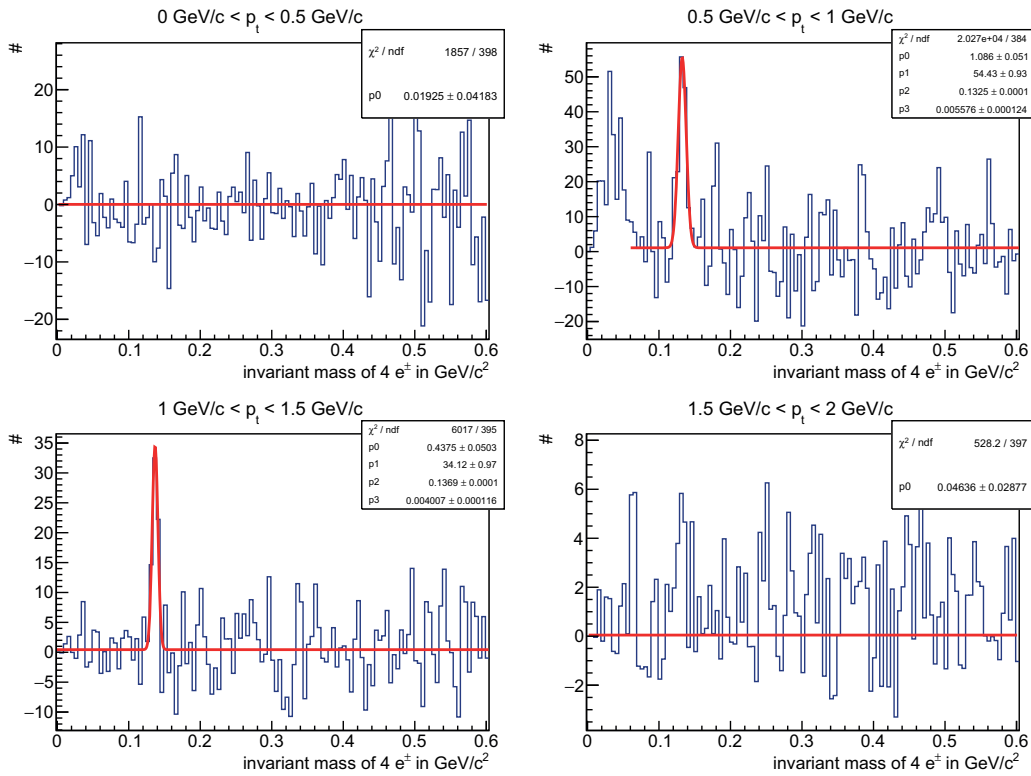


Figure 7.8. – Background-subtracted invariant mass spectra for different p_t -ranges (blue). In red fits of these spectra are shown. As fit function either a constant (first and fourth p_t -range) or a constant plus Gaussian (second and third p_t -ranges) were used.

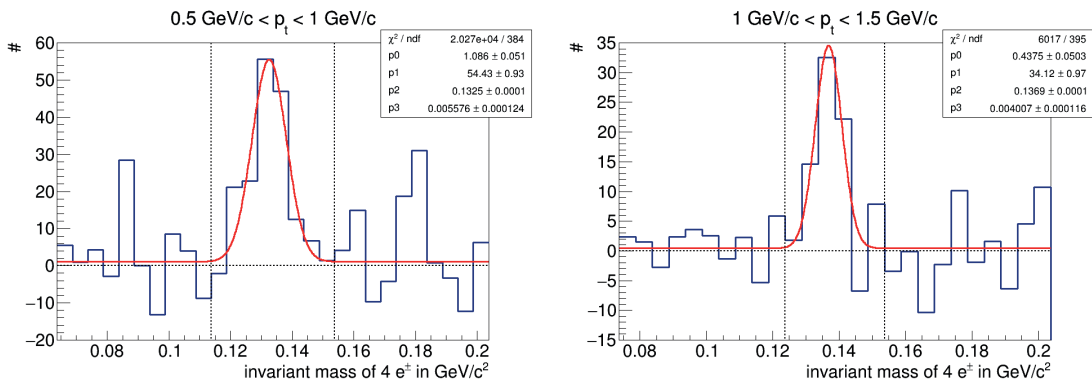


Figure 7.9. – Background-subtracted spectrum (blue) for $0.5 \text{ GeV}/c < p_t < 1.0 \text{ GeV}/c$ and $1.0 \text{ GeV}/c < p_t < 1.5 \text{ GeV}/c$. The according fit with a constant plus a Gaussian is shown in red. The black vertical lines depict the bins, which lie within the 3σ region of the peak and were used for counting the numbers of reconstructed π^0 . The horizontal black line remarks the x-axis with $y = 0$.

7.3 Limiting factors of the reconstruction efficiency

The reconstruction efficiency for π^0 as presented here is fairly low raising the question for the limiting factors. Two main effects are identified as affecting the reconstruction efficiency:

The magnetic field: The magnetic field bends all charged particles. As the mass of electrons is very low and most of them also have a very low momentum, their radius of gyration ($r_g \propto m_e \cdot v_{\perp}$, with m_e the mass of electrons and v_{\perp} their velocity perpendicular to the magnetic field) is also very small. Thus a lot of electrons can not reach the RICH detector but only cause a signal in the STS. Figure 7.10 shows the distribution of refitted momenta p and transversal momenta p_t for all electrons, which make at least a signal in the STS detector (left) and which make a signal in the STS and the RICH detector (RICH), clearly illustrating that most of the electrons have very low momenta below 1 GeV/c. The additional requirement of a signal in the RICH detector cuts away a large fraction of electrons with momenta below 0.5 GeV/c.

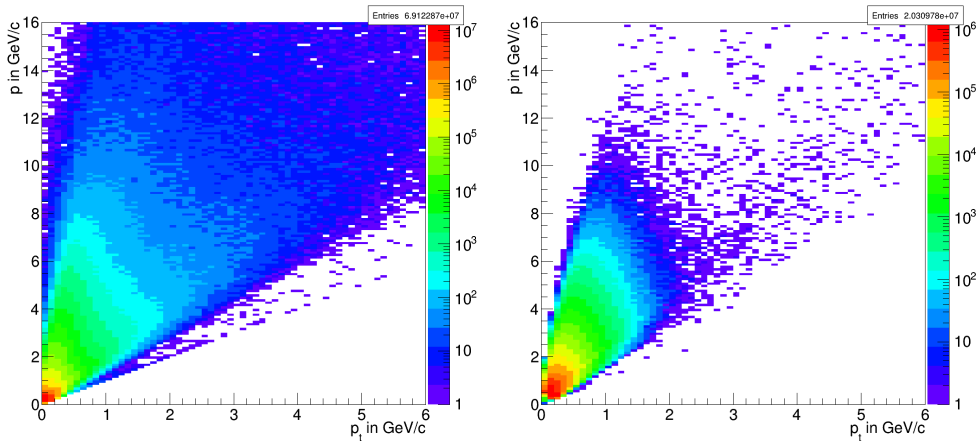


Figure 7.10. – Distributions of the momentum p versus the transversal momentum p_t of all electrons (identified with MC-true) with no signal in the RICH (left) and with a signal in the RICH (right).

By doing simulations with an even further reduced magnetic field of 30% of the nominal value (instead of 70%) it is possible to prove this assumption and estimate the influence of the magnetic field onto the reconstruction efficiency.

Detector acceptance: The detector acceptance covers a limited zenith angle of $2.5^\circ - 25^\circ$. Thus only a certain rapidity region for reconstructed particles can be covered, which was already shown in Section 6.5. There, the cut for π^0 below a rapidity of $y \approx 1.5$ could be seen in the reconstructed results.

The strongest limitation is due to the requirement of all four leptons from a π^0 being detected in the RICH detector. Therefore, it should be possible to extend the rapidity cut-off towards smaller values by only requiring three or even less of the leptons to be detected in the RICH. Nevertheless, the gain from this is expected to be only small, as the opening angle between the two photons from a π^0 and also between the conversion-leptons is quite small.

Studies regarding the possible gain in detection or reconstruction efficiency when requiring the identification of only 3 out of 4 leptons will be discussed in a separate section (Section 7.4). This section here covers results from simulations with a magnetic field of only 30 % of the nominal value. The studies include a reduced amount of simulated events of only $5 \cdot 10^5$ events, i.e. a factor of 10 less compared to all previous discussed results.

The number of expected π^0 is calculated with the combined method as presented in Section 6.5, by using MC-true data for particle identification, but reconstructed data for deriving the kinematic properties. Also here the different derived cuts (χ^2 , opening angle and invariant mass of e^+e^- -pairs) are applied to estimate their influence onto the resulting number of π^0 . Figure 7.11 shows the different numbers for all those corresponding cuts, separated by the three particle identification methods (ANN, 'normal', MC-true).

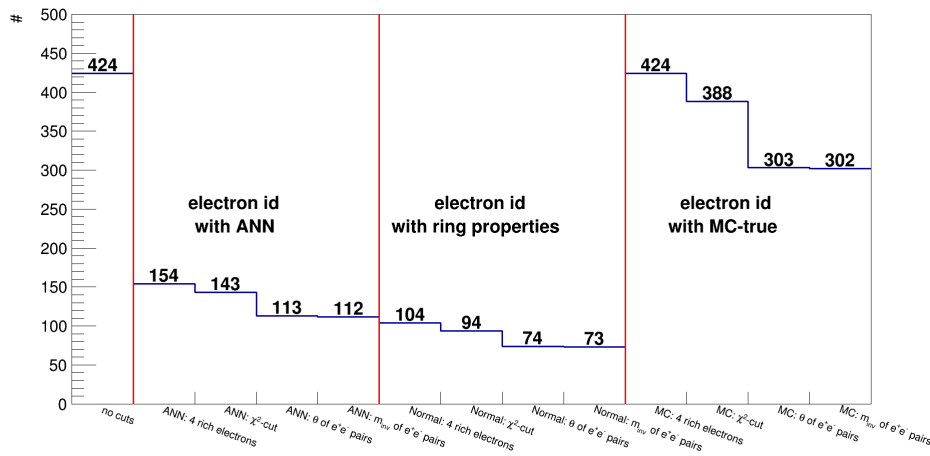


Figure 7.11. – Estimation of number of reconstructible π^0 for a testsample of $5 \cdot 10^5$ events with a reduced magnetic field of 30 % nominal value. The identification and reconstruction was done with MC-matched tracks to identified tracks in the RICH detector. All derived cuts (electron identification, χ^2 , opening angle and invariant mass of e^+e^- -pairs) were subsequently applied to estimate a realistic number of reconstructible π^0 . For the electron identification three different methods were used: the ANN, based on ring properties, and MC-true.

The number of 424 π^0 (without any cuts) already shows, that the reduced magnetic field increases the reconstruction probability significantly. Scaled to $5 \cdot 10^6$ events, as in the previous analyses, one would expect $10 \cdot 424 = 4240\pi^0$, which is an increase of roughly a factor of 7, compared to around 560 π^0 obtained in the standard analysis. As can be seen, the influence of the electron identification in case of 30 % magnetic field is much stronger as compared to 70 % magnetic field, preventing around 64 % of all π^0 to be reconstructed (compared to approx. 40 % in case of 70 % magnetic field). One reason for this might be the worse momentum reconstruction for reduced magnetic field, influencing the ANN output. Similar to before most of the unidentifiable π^0 are due to only one lepton not being correctly identified.

To judge on the efficiency, the phase-space coverage is investigated, shown in Figure 7.12 (left). The right plot shows the phase-space coverage in terms of transversal momentum p_t and rapidity y for 70 % of the magnetic field, as already shown in Figure 6.10. The direct comparison of both distributions reveal a shift of the maximum to lower p_t - and also rapidity-regions. Also the

complete distribution is shifted in a similar way, indicating the high influence of the magnetic field.

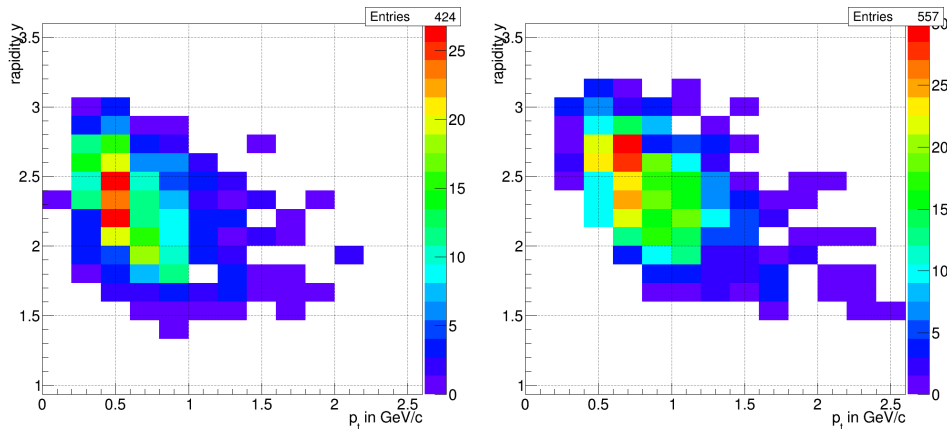


Figure 7.12. – Phase-space coverage for a magnetic field of 30 % (left) of the nominal value and 70 % (right). The π^0 were reconstructed with the combined method and no cuts were applied.

A reduction of the magnetic field does not only result in advantages but will also cause disadvantages, as the accuracy of the reconstructed momenta of all charged particles depends on the magnetic field, with a stronger field increasing the momentum resolution. This directly affects the precision of the invariant mass of the reconstructed π^0 , which can be seen in Figure 7.13 (blue histograms; left for $\pi^0 \rightarrow \gamma\gamma$ and right for $\pi^0 \rightarrow \gamma e^+ e^-$).

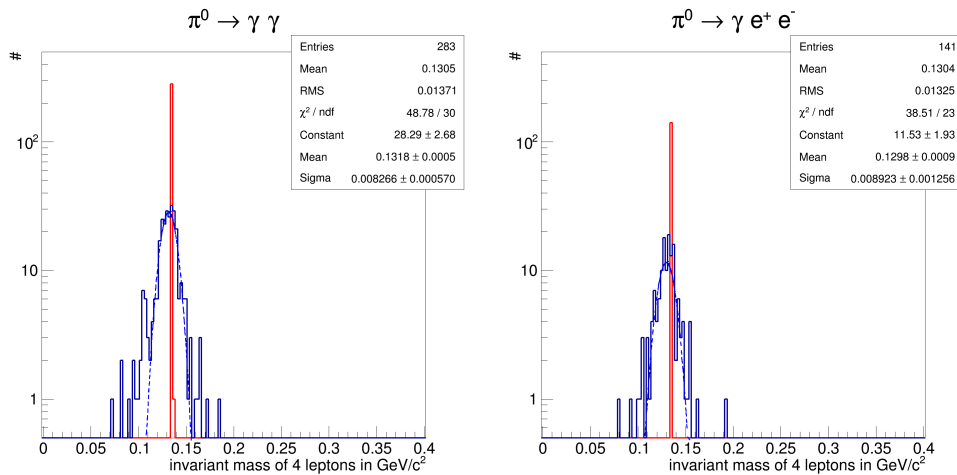


Figure 7.13. – Invariant mass spectra for π^0 reconstructed with the combined method and with a reduced magnetic field (being 30 % of the nominal value). Left: decay-channel $\pi^0 \rightarrow \gamma\gamma$, right: $\pi^0 \rightarrow \gamma e^+ e^-$. The blue lines show the invariant mass based on the reconstructed momenta of the leptons, for red the MC-true momenta were used.

Both relevant parameters, the peak positions of $(131.8 \pm 0.5) \text{ MeV}/c^2$ and $(129.8 \pm 0.9) \text{ MeV}/c^2$, and the peak width of $(8.3 \pm 0.6) \text{ MeV}/c^2$ and $(8.9 \pm 1.3) \text{ MeV}/c^2$, are worse compared to a magnetic field set to 70 % of the nominal value (compare with Figure 6.9).

7.4 Reconstructing events with less than 4 electrons

The standard reconstruction as shown in the previous sections requires the detection of all four electrons from a π^0 in the RICH-detector of CBM. The gained results in the previous sections show that this requirement strongly limits the reconstruction efficiency of π^0 , as it only rarely occurs that at least two photons could be reconstructed within one single event. The efficiency for π^0 reconstruction can be significantly increased, if only 3 or even 2 electrons are requested to reach the RICH-detector for electron identification. The remaining electrons only leave a track in the STS, allowing for track- and momentum reconstruction, but no particle identification can be applied here.

For a proper reconstruction of such cases the previously developed reconstruction scheme has to be slightly altered: instead of having just one reconstruction routine which uses all electrons with a signal in the RICH detector for a photon reconstruction, a second task is added to the reconstruction. This second part combines one electron with a signal only in the STS with one electron, which has a signal in the STS and in the RICH. Afterwards all possible combinations of these two tasks are calculated.

The ratio of the EMT background and the reconstructed spectrum which is used to estimate the necessary scaling factor for the background spectrum, shows a non-constant behaviour with a small slope over the whole range ($0 \text{ GeV}/c^2 < m_{\text{inv}} < 2 \text{ GeV}/c^2$), as can be seen in Figure 7.14. To extract a reasonable scaling factor for the region of the π^0 -peak and due to an additional background-peak underlying the π^0 -peak, a fitting range of $0.3 \text{ GeV}/c^2 - 0.6 \text{ GeV}/c^2$ was used for the fit with a constant function, resulting in a scaling factor of 0.006821 ± 0.000012 , compared to 0.0066 in the full reconstruction approach.

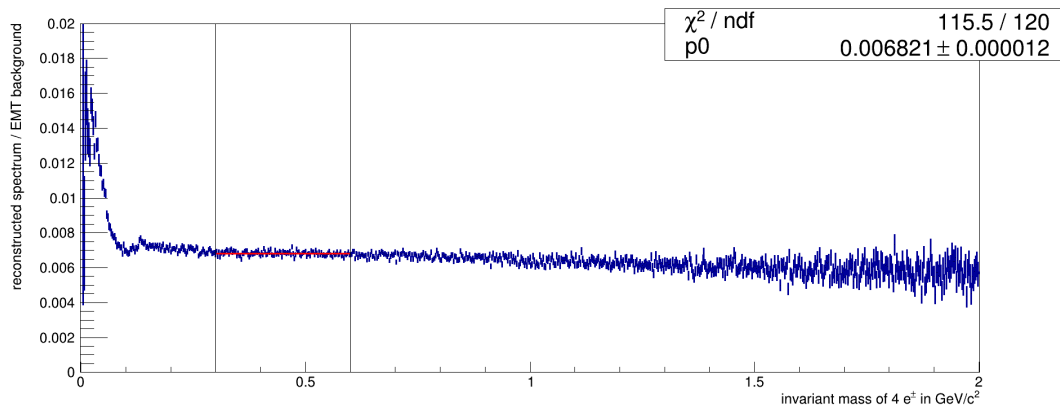


Figure 7.14. – Reconstructed invariant mass spectrum divided by the EMT background (blue). For an estimation of an appropriate scaling factor for the background a fit with a constant function was done in the range $0.3 \text{ GeV}/c^2 < m_{\text{inv}} < 0.6 \text{ GeV}/c^2$ (red).

The reconstructed invariant mass spectrum together with the calculated background from the EMT, scaled by the above extracted factor, and the background-subtracted spectrum are shown in Figure 7.15.

The reconstructed spectrum has a similar shape as for the reconstruction with all four electrons

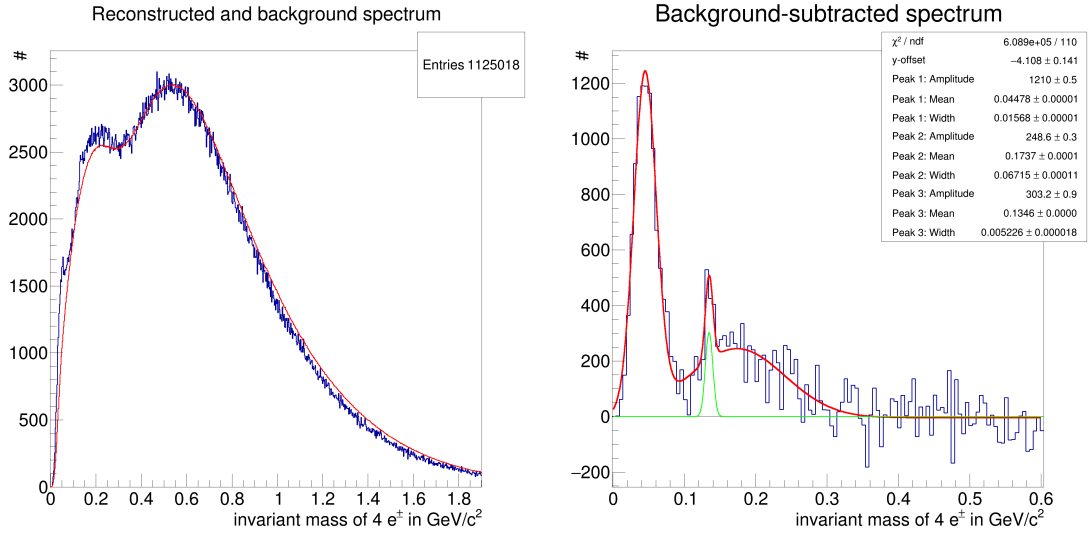


Figure 7.15. – Left: reconstructed invariant mass spectrum (blue) and scaled background from EMT (red) for the case of 3 leptons being detected in the RICH detector. Right: background-subtracted invariant mass spectrum (blue) with a fit consisting of 3 Gaussians (red). The green Gaussian peak illustrates the fitted part of the π^0 -peak.

having a signal in the RICH detector, showing two pronounced peaks below an invariant mass of $1 \text{ GeV}/c^2$. The calculated background also fits well to the reconstructed spectrum, although larger differences are visible towards higher invariant masses, and in the region of the π^0 -peak and below, explainable by the background stemming from correlated photons and only visible in the reconstructed spectrum.

For an adequate fit of the background-subtracted spectrum a function consisting of three Gaussians (one for the π^0 -peak and two for the two background peaks from correlated photons) plus a constant is used, resulting in a π^0 -peak position of $(134.6 \pm 0.1) \text{ MeV}/c^2$ and a peak width of $(5.2 \pm 0.1) \text{ MeV}/c^2$. The number of entries within this peak is much higher in comparison to full detection of the leptons, which can be recognized by the amplitude of the fit. For a better visibility of the fitted π^0 -peak, the fit-results were additionally drawn in a single Gaussian (green).

Due to the additional peak beneath the π^0 -peak counting of π^0 can only be done with the fit-function itself, but not by simply counting the number of entries within a certain range of the histogram. Limiting the range to the 3σ -region around the mean value of the peak and integrating yields a number of around 792 π^0 within the peak. This is roughly a factor of 3 more compared to the reconstruction with the requirement of four electron-signals in the RICH and clearly shows that a large gain can be expected from this type of reconstruction.

The peak at low invariant masses remains in the spectrum and becomes even more significant with a much higher amplitude than the π^0 -peak, which was not the case in the results for all electrons detected in the RICH. The reason is that the probability for the false reconstruction of a photon highly increases (without electron identification for the fourth lepton) and thus also the probability that both photons are false. This can clearly be seen in Figure 7.16 where all relevant contributions to the reconstructed invariant mass spectrum are shown, based on cuts on the MC-matched tracks.

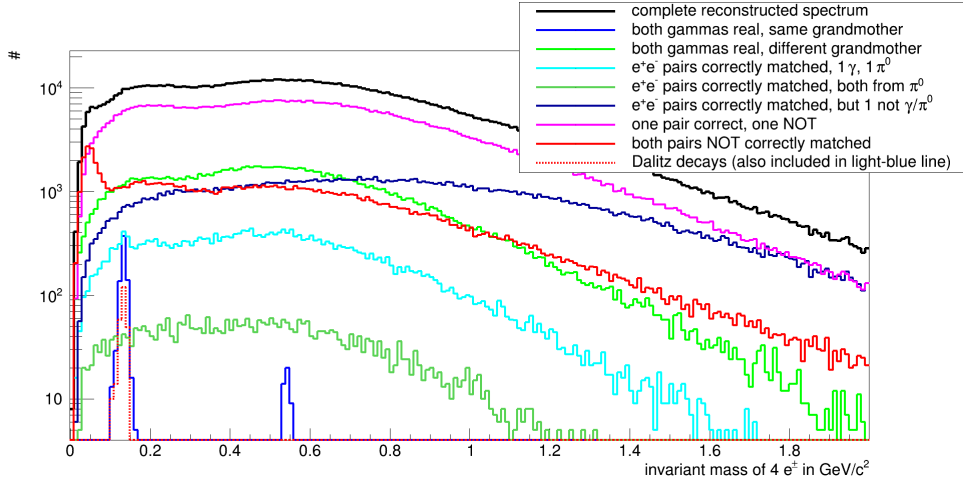


Figure 7.16. – Invariant mass spectrum for the combination of three identified leptons and one unidentified lepton using only reconstructed data with the cuts derived in Section 6.6. In addition several MC-cuts based on the matched MC-true data were applied, which were specified before, depicted in different colours. Here the binwidth is $20 \text{ MeV}/c^2$ for better visibility.

One of the most important results from this breakdown of contributions, especially in comparison to Figure 7.3, is the clearly dominating contribution, where the two electrons from one of the combined pairs do not stem from the same mother particle (purple), and also the large contributions, where this holds true for both combined pairs (red). This indicates that the photon reconstruction efficiency suffers from the missing electron identification possibilities for the fourth lepton.

Peaks at the invariant mass of π^0 (for both decay-channels $\gamma\gamma$ and $\gamma e^+ e^-$) and for η (from $\gamma\gamma$) are clearly visible with these cuts on the MC-matched tracks. Fitting the π^0 -peaks results in a mean value of $(133.6 \pm 0.3) \text{ MeV}/c^2$ ($\gamma\gamma$) and $(132.4 \pm 0.5) \text{ MeV}/c^2$ ($\gamma e^+ e^-$) with peak widths of $(7.1 \pm 0.3) \text{ MeV}/c^2$ ($\gamma\gamma$) and $(7.2 \pm 0.4) \text{ MeV}/c^2$ ($\gamma e^+ e^-$), which seem slightly worse in comparison to the previous fit results for the reconstructed data only. Nevertheless the results are in good agreement considering the small amount of statistics.

Counting the number of π^0 here in those two peaks yields values of 715 π^0 ($\gamma\gamma$) and 256 π^0 ($\gamma e^+ e^-$), again illustrating the higher reconstruction probability of the Dalitz-decay in comparison to the $\gamma\gamma$ decay-channel. This total number of π^0 in the sample is also well comparable to the above extracted number from the fit.

The η -peak is not visible in the background-subtracted spectrum due to the very small amount of statistics and lower geometrical acceptance (and also due to the optimization of all cuts towards the reconstruction of π^0), but only with the additional applied MC-true cuts. It consists of 60 entries, resulting in a fitted mean value of $(541.3 \pm 2.6) \text{ MeV}/c^2$ and a peak width of $(12.1 \pm 4.9) \text{ MeV}/c^2$, which roughly matches the expected mass of $547.9 \text{ MeV}/c^2$.

7.4.1. Additional momentum-cut

All applied cuts were optimised for the case of four identified electrons in the RICH detector. Thus they are not necessarily optimal for the reconstruction with three identified electrons. An improvement might be achievable by optimising existing cuts or adding new cuts. One possibility here is a momentum cut on the fourth electron. When using the reconstruction routines from Section 6.5 (i.e. reconstructing real π^0 based on the MC-matched tracks), but with the requirement of only three identified electrons in the RICH, and comparing the distributions of particle momentum p versus the emission angle θ for the three identified electrons and the one unidentified electron, clear differences become visible, as shown in Figure 7.17.

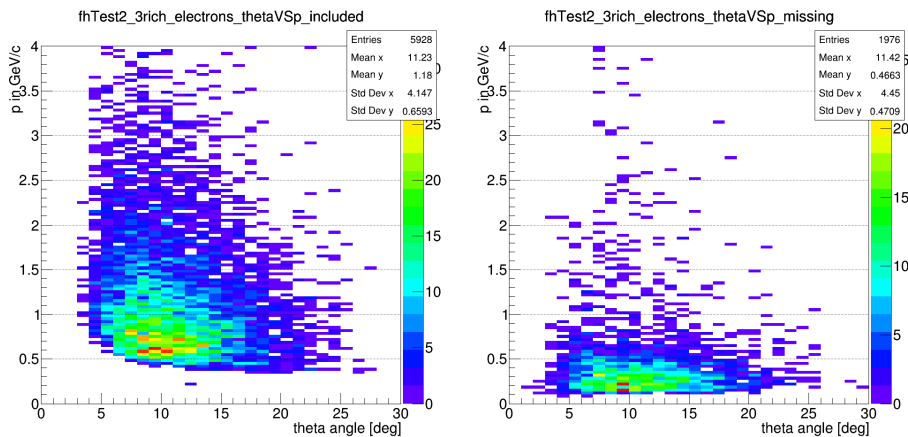


Figure 7.17. – Distribution of emission angles θ of an electron versus its momentum p . Left: results for the three identified electrons of a π^0 , right: results for the unidentified electron of a π^0 .

For the momenta of the three electrons with a signal in the RICH (left histogram) there is a clear cut towards low momenta in the region of 0.4 GeV/c visible, whereas most of the electrons without a signal in the RICH (right) have a reconstructed momentum below this cut. This is also an indication that these low-momentum electrons are bended out by the magnetic field and therefore cannot reach the RICH detector. Based on this comparison a momentum-cut for the fourth electron of $p_4 \leq 0.6$ GeV/c was derived and applied to the analysis. The resulting invariant mass spectrum together with the background from EMT and the background-subtracted spectrum is shown in Figure 7.18.

The spectra look very similar to the spectra without the momentum-cut on the fourth electron. Especially the background-subtracted spectrum shows the same structure, with a pronounced π^0 -peak and two additional peaks from the background. The fit results in a π^0 -peak position of $(136.2 \pm 0.3) \text{ MeV}/c^2$ with a peak width of $(6.4 \pm 0.4) \text{ MeV}/c^2$.

Integrating the π^0 -peak alone within the 3σ region yields a total of 795 π^0 , which is comparable to the results without this additional momentum cut. Comparing the reconstructed invariant mass spectra with and without the momentum cut reveals a large drop in background entries by a factor of 2. As an important result the signal-to-background ratio can be significantly improved with this momentum cut on the fourth electron.

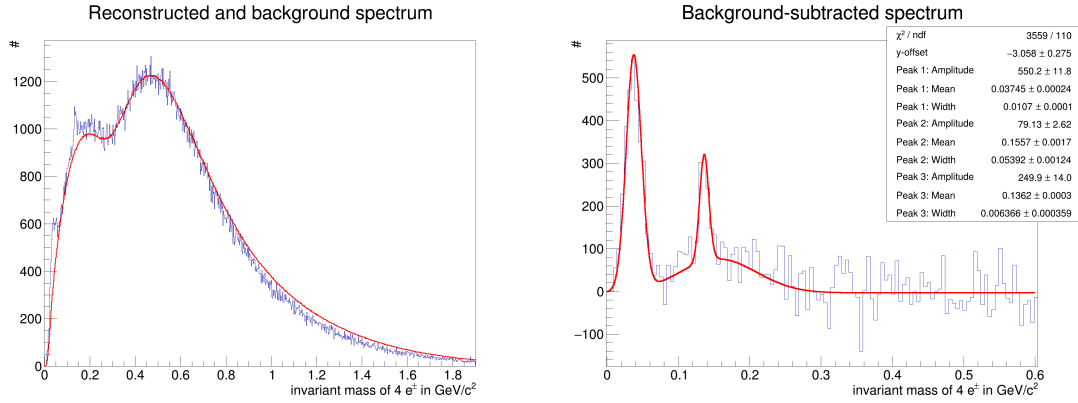


Figure 7.18. – Left: reconstructed invariant mass spectrum (blue) and scaled background from EMT (red) for the case of 3 electrons being detected in the RICH detector and an additional momentum-cut on the fourth (unidentified) electron of $p \leq 0.6 \text{ GeV}/c$. Right: background-subtracted invariant mass spectrum (blue) with a fit consisting of 3 Gaussians (red).

7.5 Absolute efficiency of this method

All previous shown results are based on simulated event samples generated with UrQMD. The phase-space coverage of those simulated π^0 are very inhomogeneous and only covers a certain fraction (see e.g. Figure 6.10). Therefore, it is not possible to adequately calculate the reconstruction efficiency of the presented method from these samples.

By simulating a sample with input from the boxgenerator only consisting of π^0 , which are homogeneously distributed within the phase-space, allows for a clear estimation of the geometrical acceptance of this method. The sample used here is based on 10^5 events, each containing 200 π^0 distributed within $p_t = 0 \text{ GeV}/c - 6 \text{ GeV}/c$ and rapidity $y = 0 - 6$. The calculations done are based on the combined method, i.e. reconstructed tracks were used for the calculation and the matched MC-true tracks of the reconstructed tracks were used for the identification.

The resulting distributions for the simulated and reconstructed distributions, together with the division of both to get the efficiency, can be seen in Figure 7.19.

The limitations in rapidity at $y \approx 1.5$ and $y \approx 3.5$ are clearly visible and confirm the results and estimations from the previous calculations. The limitation towards low transversal momenta seems to be slightly depending on the rapidity, with low rapidities being related to an increased transversal momentum cut-off. The results show that there is no limitation towards high transversal momentum within the simulated range of up to $p_t = 6 \text{ GeV}/c$.

The highest acceptances reached are in the order of $4 \cdot 10^{-4}$, going down to around 10^{-5} towards the limiting borders of the reconstructed phase-space.

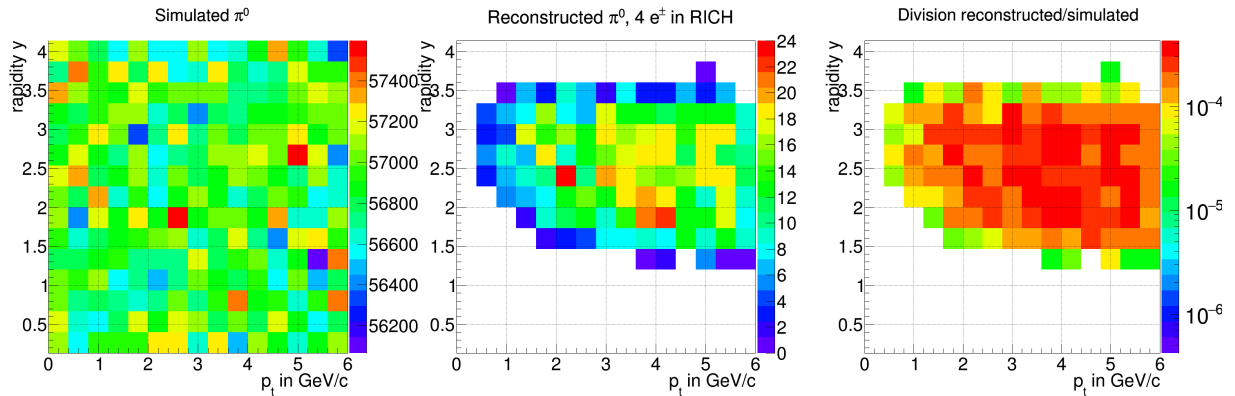


Figure 7.19. – Coverage of the phase-space in terms of transversal momentum p_t and rapidity y . Left: all simulated π^0 , mid: all reconstructed π^0 from the combined method, i.e. all four leptons identified in the RICH, right: ratio of reconstructed and simulated distribution.

7.6 Summary: reconstruction of π^0 via conversion

This chapter showed first detailed feasibility studies for the usage of the conversion method for the reconstruction of light mesons like π^0 or η , with a focus on the RICH detector for the identification of electrons and positrons.

By using the conversion method with pure MC-true data to generate tomography pictures of the CBM detector, it is possible to identify parts with a high amount of conversion within the complete detector, and thus revealing high-density regions, which might influence the electron background and the track reconstruction for subsequent sub-detectors.

Studies for the estimation of the π^0 -reconstruction quality (in terms of invariant mass peak position and width), using a method based on MC-true data for particle identification and reconstructed particle momenta for combination, reveal a good match of the invariant mass peak position with the expected theoretical value and a decent peak width of a few MeV. These studies also showed, that the reconstruction probability for π^0 is very low, as only several hundred π^0 out of 10^8 simulated π^0 can be reconstructed.

To resemble realistic conditions, studies completely relying on reconstructed data were done, i.e. also the particle identification is based on reconstructed data and not on MC-true information anymore. Using an ANN for the rings, which are reconstructed in the RICH detector, allows to identify a large fraction of electrons and positrons with a minor contamination of other particles. The calculated invariant mass spectra show a clearly distinguishable π^0 -peak on top of some background, which mainly stems from the false combination of two (correctly reconstructed) photons. By applying the Event Mixing Technique it is possible to adequately describe and subtract this background, revealing the π^0 -peak and allowing for detailed studies. A Gaussian fit of this peak results in a mean value of $(133.2 \pm 0.5) \text{ MeV}/c^2$, which is close to the expectation of $135 \text{ MeV}/c^2$, and a peak width of $(6.3 \pm 0.6) \text{ MeV}/c^2$. Counting all entries in the background-subtracted spectrum within the 3σ -region of this fitted peak results in 239 ± 52 reconstructed π^0 , with a signal-to-background ratio of $(14.3 \pm 2.7) \%$.

The investigation of the phase-space coverage (in terms of transversal momentum p_t and rapidity

y) shows a cut-off at $y \approx 1.5$ and $y \approx 3$ due to the geometrical detector acceptance, and also at very small p_t mainly due to the magnetic field and opening angle of the two decay photons. An improvement, i.e. a wider coverage, can be achieved by reducing the nominal magnetic field down to 30 % from the initial 70 %.

Most of the results are gained by requiring all four electrons from a π^0 to be detected and identified in the RICH detector. This strong condition results in a low reconstruction probability. The probability can be increased by requiring only three out of four leptons being detected in the RICH detector for the analysis. This results in a highly increased number of approx. 792 reconstructed π^0 . Unfortunately the according background can not completely be described with the Event Mixing Technique, leading to an additional broad peak beneath the π^0 -peak. Using MC-true cuts afterwards on these results reveals the clear existence of an η -peak, which vanishes in the invariant mass spectrum due to the variations. Also this η -peak is not visible for the results with all four leptons being detected.

For an estimation of the efficiency of this method simulations only containing π^0 are used, homogeneously distributed in p_t and y . The resulting reconstructed phase-space coverage in comparison to the simulated distribution show an acceptance in the region of 10^{-5} up to 10^{-4} .

As a final conclusion it can be stated, that these studies showed a successful application of the conversion method within realistic UrQMD simulations for the CBM SIS100 setup.

Summary and Outlook

The analyses and results presented in this thesis cover two important aspects, both strongly tied together by the involved RICH detector. The first part was the investigation of several photon detectors foreseen for the CBM-RICH camera based on data from a beamtest to be able to detect Cherenkov light with high efficiency. The second part includes simulations and analyses regarding the reconstruction of π^0 by using the conversion of decay-photons and detection of the electrons and positrons with the RICH detector.

Comparison of photon sensors

For the CBM-RICH photon detector three different models were considered: the Hamamatsu H8500 MAPMT, the Hamamatsu R11265 MAPMT, and the Photonis XP85012 MCP. The different electron multiplication mechanisms of MAPMTs and MCPs have different advantages and disadvantages, which could be shown to some extent.

During a beamtest in 2012 at CERN, all three sensor types could be compared under the same conditions and in a realistic environment. The analyses of the data revealed that the Hamamatsu R11265 performs best in terms of detected photons per electron Cherenkov ring, as well as in terms of produced crosstalk. The performance of the Hamamatsu H8500 was similar to the Photonis XP85012 with respect to number of detected photons per ring, both being worse than the R11265. In addition, the Photonis XP85012 produces the highest amount of crosstalk.

The single-photon spectra show an advantage of the R11265 type, as the single-photon peak is clearly pronounced (partially also a second peak, stemming from electrons directly hitting the second dynode, is visible) with a negligible low-amplitude peak, allowing to find and set a hardware threshold (which is required in the data taking to reduce the amount of data to a reasonable level) at a low level, without influencing the efficiency. The H8500 type shows a decent low-amplitude peak in the single-photon spectrum but also a pronounced single-photon peak.

The spectra of the XP85012 MCPs are dominated by the low-amplitude peak, making it hard to set the threshold at a reasonable level without affecting the efficiency.

The low-amplitude peak in the single-photon spectra can be (strongly) reduced by applying a cut, such that only hits without any additional hit in the neighbouring pixel, are considered. Thus the entries (at least a large fraction) in the low-amplitude peak are judged as being crosstalk hits and not real hits.

Feasibility studies of conversion analysis with the CBM-RICH

The studies showed that it is possible to reconstruct π^0 with reconstructed information from the MVD/STS and the RICH alone, via the decays of $\pi^0 \rightarrow \gamma\gamma$ or $\pi^0 \rightarrow \gamma e^+ e^-$, conversion of the photons, and detection of the electrons and positrons in the RICH detector. The probability for the reconstruction is quite low, in the order of around 0.02% due to the small conversion probability of the photons. For the presented analyses, only conversion within the target has been considered.

The efficiency of reconstruction can be increased by either decreasing the magnetic field (which is not suitable in the final experiment), or by requiring just three out of four leptons being detected in the RICH detector. As a consequence a dedicated electron identification of the one remaining electron (without RICH signal) is not possible, thus increasing the background.

The background in the invariant mass spectra can be adequately described with the Event Mixing Technique, thus revealing a clear π^0 peak with just statistical fluctuations remaining in the spectrum.

Outlook

The comparison of the three photon detector models showed that the Hamamatsu R11265 performs best, mainly focussed on the number of the detected photons per ring, being a result of high detection efficiency and least crosstalk fraction.

As a combination of the good detection properties of the R11265 and the geometrical coverage of the H8500, Hamamatsu developed the H12700 MAPMT, which shares its outer dimensions with the H8500 and the single-photon optimized dynode system with the R11265. Successive lab measurements and a beamtest in 2014 revealed the overall better performance of the H12700 in comparison to both Hamamatsu models tested previously, which was the reason to go for the H12700 model to be used in the final CBM-RICH detector. At present, several units are delivered by Hamamatsu on a monthly basis and are series tested in Wuppertal with ongoing exchange of the results with Hamamatsu to able to even further enhance the production process.

The conversion analysis proved that the reconstruction of π^0 from the conversion of decay-photons via the detection of electrons and positrons in the CBM-RICH is feasible. The presented analyses only focussed on conversion within the target itself. A gain in statistics of around a factor of 6 is expected when also considering conversion in the detector material, thus requiring appropriate second vertex fitting.

A weakened requirement of the identification of only 3 out of all 4 leptons in the RICH detector leads to a large gain in statistics, although no electron identification for the fourth particle is possible and the used cuts are not optimized for this case. Further optimization of the cuts and

consideration of additional cuts should help reducing the background, e.g. using a momentum-cut as presented or using the information about the fitted track and its bending radius to broadly distinguish between particles with low and high mass.

Beamtime Overview 2012 - Run

Table A.1. – Positions and serial numbers of the PMTs used during the beamtime. In addition the gain as given by the manufacturer is included. During the HV-scan the high-voltage of PMTs #7, #8, #11, #12 (position A) was always kept at 1000 V as a reference value. Arrows (↓) mark the same value as above, up to ●.

HV-Scan:					
Run No.	Ring Position	Beam Energy	HV, PMT	HV, MCP	additional info
97	A	3	1100	1900	
100	G	↓	↓	↓	
101	I	↓	↓	↓	
102	E	↓	●	●	
103	A	↓	1050	1900	
104	I	↓	↓	↓	
105	G	↓	↓	↓	
106	E	↓	●	●	
107	A	↓	1000	1800	
108	I	↓	↓	↓	
109	I	↓	↓	↓	
110	G	↓	↓	↓	
111	E	↓	●	●	
112	A	↓	950	1700	

Run No.	Ring Position	Beam Energy	HV, PMT	HV, MCP	additional info
113	I	↓	↓	↓	
114	I	↓	↓	↓	
115	G	↓	↓	↓	
116	E	↓	•	•	
117	A	↓	900	1600	
118	I	↓	↓	↓	
119	G	↓	↓	↓	
120	E	↓	•	•	
121	A	↓	1100	1650	
122	D	↓	1100	↓	
123	D	•	1050	•	

Table A.2. – Positions and serial numbers of the PMTs used during the beamtime. In addition the gain as given by the manufacturer is included. Arrows (↓) mark the same value as above, up to •.

Threshold-Scan 1:					
Run No.	Ring Position	Beam Energy	threshold	additional info	
126	A	8	25		
127	I	↓	↓		
128	G	↓	↓		
129	E	↓	↓		
130	D	↓	•		
131	A	↓	28		
132-133	I	↓	↓		
134	G	↓	↓		
135	E	↓	↓		
136	D	↓	↓		
137	B	↓	•		
138	A	↓	35		
139	I	↓	↓		
140	G	↓	↓		
141	E	↓	↓		
142	D	↓	•		

Run No.	Ring Position	Beam Energy	threshold	addtional info
143	D	↓	50	
144-145	A	↓	↓	
146-147	I	•	↓	
148	G	6	↓	
149-150	E	↓	•	
151	E	↓	70	
152	A	↓	↓	
153	I	↓	↓	
154	G	↓	↓	
155	D	•	•	
Threshold-Scan 1:				
170	A	4	28	
171	A	↓	25	
172	I	↓	↓	
173	G	↓	↓	
174	E	↓	↓	
175	D	↓	•	
176	A	↓	28	
177	I	↓	↓	
178	G	↓	↓	
179	E	↓	↓	
180	D	↓	↓	
181	B	↓	•	
182	A	↓	35	
183	I	↓	↓	
184	G	↓	↓	
185	E	↓	↓	
186	D	↓	•	
187	A	↓	50	
188	I	↓	↓	
189	G	↓	↓	
190	E	↓	↓	
191	D	↓	•	

Run No.	Ring Position	Beam Energy	threshold	additional info
192	A	↓	70	
193	I	↓	↓	
194	G	↓	↓	
195	E	↓	↓	
196	D	↓	•	
197	A	•	28	

Table A.3. – Overview of the LED runs, i.e. beam was switched off. Given are the different used LEDs and the high-voltage setting of the sensors (compare Table 5.1).

Run No.	LED	HV	Threshold
201	470 nm	new	28
202	470 nm	old	↓
203	275 nm	old	↓
204	275 nm	new	↓
205	245 nm	new	↓
206	245 nm	old	↓
207	470 nm	new	•

Beamtime 2012 - Crosstalk Results

B.1 Exemplary distributions for Hamamatsu H8500

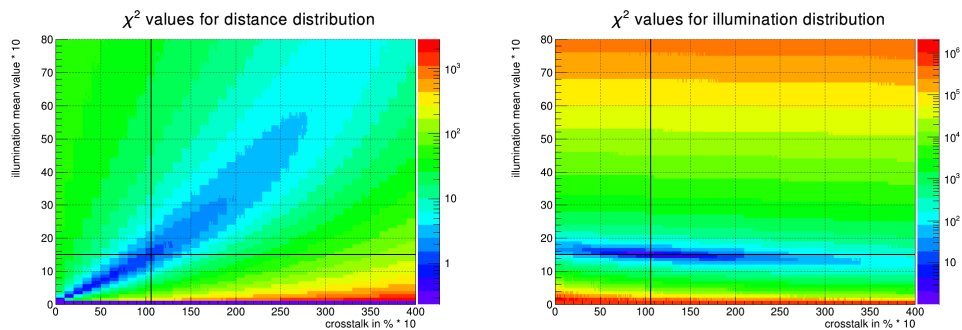


Figure B.1. – PMT #1: χ^2 -distributions for the distance distribution (left) and for the illumination distribution (right). Resulting minima are indicated with black lines.

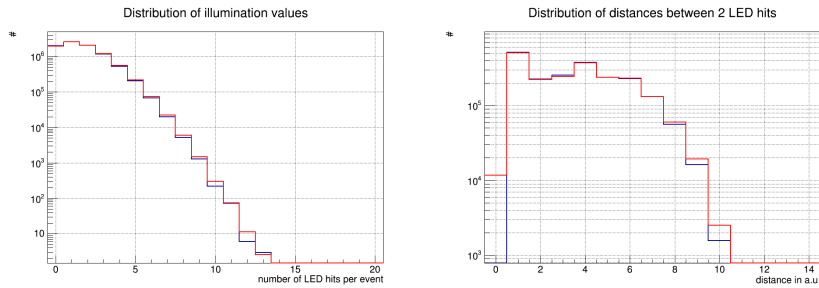


Figure B.2. – PMT #1: distribution from data (blue) and best fitting simulation (red) for the illumination distribution (left) and for the distance distribution (right).

B.2 Exemplary distributions for Photonis XP85012

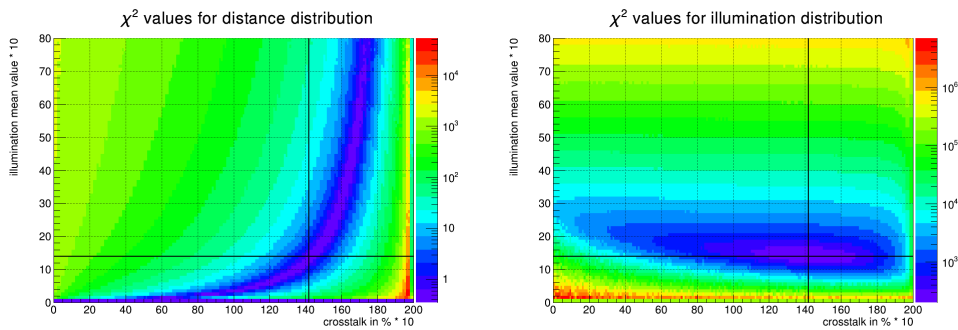


Figure B.3. – PMT #13: χ^2 -distributions for the distance distribution (left) and for the illumination distribution (right). Resulting minima are indicated with black lines.

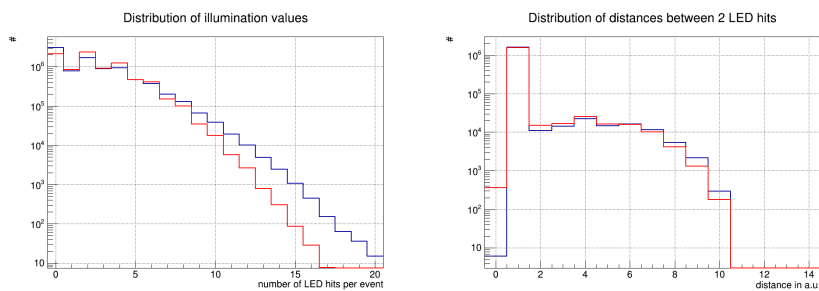


Figure B.4. – PMT #13: distribution from data (blue) and best fitting simulation (red) for the illumination distribution (left) and for the distance distribution (right).

B.3 Exemplary distributions for Hamamatsu R11265

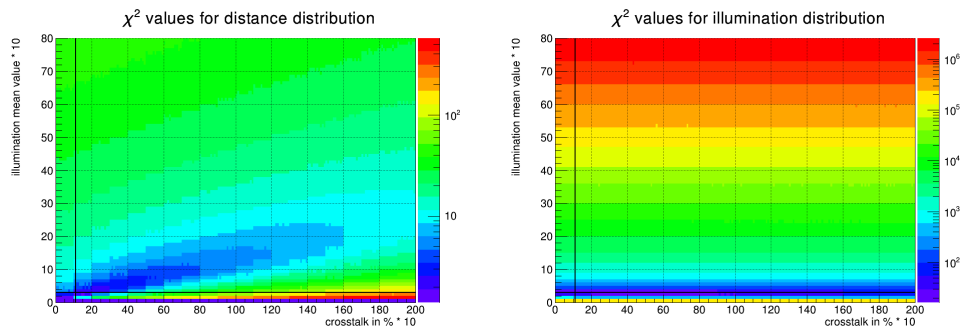


Figure B.5. – PMT #17: χ^2 -distributions for the distance distribution (left) and for the illumination distribution (right). Resulting minima are indicated with black lines.

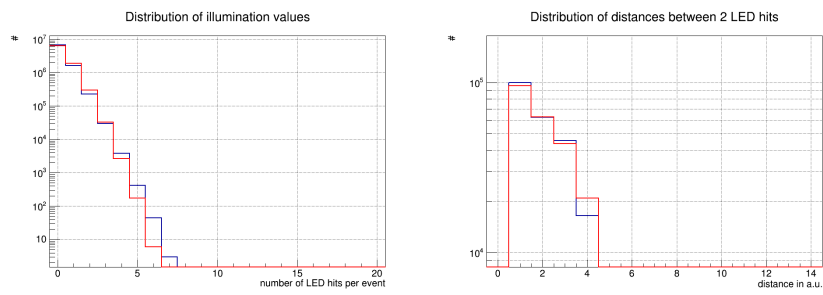


Figure B.6. – PMT #17: distribution from data (blue) and best fitting simulation (red) for the illumination distribution (left) and for the distance distribution (right).



References

References for chapter 2

- [2] Bengt Friman et al. *The CBM physics book: Compressed baryonic matter in laboratory experiments*. Lect. Notes Phys. Vol. 814. 2011, pp. 980. doi: 10.1007/978-3-642-13293-3.
- [3] S. Chattopadhyay and others (for the CBM collaboration). 'Challenges in QCD matter physics - The Compressed Baryonic Matter experiment at FAIR'. In: *arXiv* (2016). arXiv: 1607.01487.
- [4] Contemporary Physics Education Project. *Phases of Nuclear Matter diagram*. URL: <http://www2.lbl.gov/abc/chartimages/Nuclear%20Phase%20Diagram.jpg>.
- [5] H. Stöcker. 'Collapse of Flow: Probing the Order of the Phase Transition'. In: *arXiv* (2007). arXiv: 0710.5089.
- [6] J. Heuser for the CBM collaboration. 'Status of the CBM experiment'. In: *EPJ Web Conf. 95 01006 (Proceedings of ICNFP 2014)* (2015).
- [7] G. Akakishiev et al. 'Dielectron production in Ar+KCl collisions at 1.76 AGeV'. In: *Phys. Rev. C* 84 (2011), p. 014902. doi: 10.1103/PhysRevC.84.014902.
- [8] R. Vogt. *Ultrarelativistic Heavy-Ion Collisions*. Elsevier, 2007.
- [9] Sourav Sarkar, Helmut Satz, and Bikash Sinha. *The Physics of the Quark-Gluon Plasma*. 2010. doi: 10.1007/978-3-642-02286-9.
- [10] P. Hohler and R. Rapp. 'Is ρ -meson melting compatible with chiral restoration?' In: *Phys. Lett. B* 731 (2014), pp. 103–109.
- [11] R. Rapp and H. van Hees. 'Thermal dileptons as fireball thermometer and chronometer'. In: *Phys. Lett. B* 753 (2016), pp. 586–590.

- [12] Y.C. Pachmayer (for the HADES Collaboration). 'Dielectron production in $^{12}\text{C} + ^{12}\text{C}$ collisions at 1 GeV/u and the solution to the DLS puzzle'. In: *Journal of Physics G: Nuclear and Particle Physics* 35 (2008), p. 104159.
- [13] A.A. Grigorian and P. Sonderegger. 'Physics of low mass dileptons produced in heavy ion collisions'. In: *Technical Note NA50-Up 97/1* ().
- [14] E.V. Shuryak. 'Quark-gluon plasma and hadronic production of leptons, photons and psions'. In: *Physics Letters B* 78 (1978), pp. 150–153.
- [15] E.V. Shuryak. 'Quantum chromodynamics and the theory of superdense matter'. In: *Physics Reports* 61 (1980), pp. 71–158.
- [16] L.D. McLerran and T. Toimela. 'Photon and dilepton emission from the quark-gluon plasma: Some general considerations'. In: *Phys. Rev. D* 31 (1985), pp. 545–563.
- [17] G. Agakichiev et al. (HADES collaboration). 'The high-acceptance dielectron spectrometer HADES'. In: *Eur. Phys. J. A* 41 (2009), pp. 243–277.
- [18] *Technical Design Report for the CBM Ring Imaging Cherenkov Detector*. Tech. rep. 2013, 215 p. URL: <http://repository.gsi.de/record/65526>.
- [19] C. Pauly. *Recent update on readout developments*. Talk from the 26th CBM collaboration meeting in Prague, Czech Republic. 2015.
- [20] C. Pauly. *Status electronics development*. Talk from the 27th CBM collaboration meeting in Darmstadt, Germany. 2016.
- [21] T. Mahmoud. *Optimisation of the CBM-RICH geometry*. Talk from the 27th CBM collaboration meeting in Darmstadt, Germany. 2016.
- [22] I. Kres. *Deriving the effective focal plane for the CBM-RICH detector*. Talk from the 27th CBM collaboration meeting in Darmstadt, Germany. 2016.
- [23] Yuri Ryabov. *CBM RICH mechanical design*. Talk given on the 27th CBM collaboration meeting in Darmstadt. 2016.

References for chapter 3

- [18] *Technical Design Report for the CBM Ring Imaging Cherenkov Detector*. Tech. rep. 2013, 215 p. URL: <http://repository.gsi.de/record/65526>.
- [24] Hamamatsu Photonics. *Photomultiplier Tubes - Basics and Application*. 2007.
- [25] J. Adamczewski-Musch et al. 'The CBM RICH project'. In: *Nucl. Instrum. Methods A* (2016). VCI2016 Proceedings of the 14th Vienna Conference on Instrumentation, Vienna, Austria, February 15 – 19, 2016. DOI: 10.1016/j.nima.2016.05.102.
- [26] C. Pauly. private communication.
- [27] Jan Kopfer. 'Development of a prototype camera and Monte Carlo studies for the optimisation of the CBM-RICH detector'. PhD thesis. 2014.

References for chapter 4

- [18] *Technical Design Report for the CBM Ring Imaging Cherenkov Detector*. Tech. rep. 2013, 215 p. URL: <http://repository.gsi.de/record/65526>.
- [27] Jan Kopfer. 'Development of a prototype camera and Monte Carlo studies for the optimisation of the CBM-RICH detector'. PhD thesis. 2014.
- [28] J. Adamczewski-Musch et al. 'Wavelength shifting films on multianode PMTs with UV-extended windows for the CBM RICH detector'. In: *Nucl. Instrum. Methods A* 766 (2014). RICH2013 Proceedings of the Eighth International Workshop on Ring Imaging Cherenkov Detectors, Shonan, Kanagawa, Japan, December 2 – 6, 2013, pp. 180–182. DOI: 10.1016/j.nima.2014.05.011.
- [29] J. Adamczewski-Musch et al. 'Influence of wavelength-shifting films on multianode PMTs with UV-extended windows'. In: *Nucl. Instrum. Methods A* 783 (2015), pp. 43–50. DOI: 10.1016/j.nima.2015.02.014.
- [30] J. Adamczewski-Musch et al. 'Determination of tolerances of mirror displacement and radiator gas impurity for the CBM RICH detector'. In: *Nucl. Instrum. Methods A* 766 (2014). RICH2013 Proceedings of the Eighth International Workshop on Ring Imaging Cherenkov Detectors, Shonan, Kanagawa, Japan, December 2 – 6, 2013, pp. 221–224. DOI: 10.1016/j.nima.2014.04.074.
- [31] L. Kotchenda et al. 'STAR TPC gas system'. In: *Nucl. Instrum. Methods A* 499 (2003), pp. 703–712.
- [32] L. Kotchenda et al. 'PHENIX Muon Tracking Detector Gas System'. In: *Nucl. Instrum. Methods A* 578 (2007), pp. 172–179.
- [33] L. Kotchenda et al. 'A gas system for the CBM-RICH prototype'. In: *CBM Progress Report 2012* (2013).
- [34] P. Kravtsov et al. 'A slow-control system for the CBM-RICH gas system'. In: *CBM Progress Report 2012* (2013).
- [35] L. Kochenda et al. 'Results of the RICH prototype gas system during the 2012 beam test'. In: *CBM Progress Report 2012* (2013).
- [36] S. Reinecke. 'Charakterisierung von Spiegeln für den RICH-Detektor von CBM'. Diploma thesis. 2011.
- [37] J. Song and I.-K. Yoo. 'Slow control system for the CBM-RICH prototype'. In: *CBM Progress Report 2012* (2013).
- [38] K.-H. Becker, C. Pauly, and K.-H. Kampert. 'Development of an ARDUINO-based slow-control monitoring system with EPICS integration'. In: *CBM Progress Report 2012* (2013).
- [39] A.S. Brogna et al. 'N-XYTER, a CMOS read-out ASIC for high resolution time and amplitude measurements on high rate multi-channel counting mode neutron detectors'. In: *Nucl. Instrum. Methods A* 568 (2006), pp. 301–308.
- [40] *CBM Wiki*. Internal, not publicly accessible. URL: <https://cbm-wiki.gsi.de/foswiki/bin/view/NXYTER/WebHome>.

- [41] N. Abel et al. 'Development of the Read Out Controller for the nXYTER Front End Board'. In: *GSI Progress Report 2007* (2008).
- [42] S. Manz et al. 'An universal read-out controller'. In: *Journal of Instrumentation* 5.11 (2010), p. C11017.

References for chapter 5

- [18] *Technical Design Report for the CBM Ring Imaging Cherenkov Detector*. Tech. rep. 2013, 215 p. URL: <http://repository.gsi.de/record/65526>.
- [24] Hamamatsu Photonics. *Photomultiplier Tubes - Basics and Application*. 2007.
- [27] Jan Kopfer. 'Development of a prototype camera and Monte Carlo studies for the optimisation of the CBM-RICH detector'. PhD thesis. 2014.
- [43] J. Eschke and F. Meyer. 'Investigation of crosstalk in multi-anode photomultipliers for the CBM-RICH photodetector'. In: *CBM Progress Report 2010* (2011).
- [44] Hamamatsu. *H8500 series/H10966 series datasheet*. URL: https://www.hamamatsu.com/resources/pdf/etd/H8500_H10966_TPMH1327E.pdf.
- [45] J. Seguinot and T. Ypsilantis. 'Photo-ionization and Cherenkov Ring Imaging'. In: *Nucl. Instrum. Methods A* 142 (1977), pp. 377–391.
- [46] ROOT online documentation HowTo. *Numerical Minimization*. URL: <https://d35c7d8c.web.cern.ch/numerical-minimization> (visited on 01/06/2016).
- [47] C. Pauly. *New H12700 PMTs: Status and further measurements*. Talk from the 24th CBM collaboration meeting in Krakow, Poland. 2014.
- [48] J. Adamczewski-Musch et al. 'The CBM RICH project'. In: *Nucl. Instrum. Methods A* 766 (2014). RICH2013 Proceedings of the Eighth International Workshop on Ring Imaging Cherenkov Detectors, Shonan, Kanagawa, Japan, December 2 – 6, 2013, pp. 101–106. doi: 10.1016/j.nima.2014.05.071.
- [49] A. Lehman et al. 'Systematic studies of micro-channel plate PMTs'. In: *Nucl. Instrum. Methods A* 639 (2011), pp. 144–147.
- [50] S. Korpar et al. 'Timing and cross-talk properties of BURLE multi-channel MCP PMTs'. In: *Nucl. Instrum. Methods A* 595 (2008), pp. 169–172.
- [51] S. Reinecke. *Tests and comparison of various photon detection devices for the CBM-RICH*. Talk for the DIRC2013 conference. 2013.

References for chapter 6

- [52] Melanie Klein-Bösing. 'Development of a Transition Radiation Detector and Reconstruction of Photon Conversions in the CBM Experiment'. PhD thesis. 2009.

- [53] T. Dahms et al. (PHENIX Collaboration). ‘Measurement of photons via conversion pairs in $\sqrt{s_{NN}} = 200$ GeV Au+Au collisions with the PHENIX experiment at RHIC’. In: *Eur. Phys. J. C* 49 (2007), pp. 249–253.
- [54] K. Koch et al. (ALICE Collaboration). ‘ π^0 and η measurement with photon conversions in ALICE in proton-proton collisions at $\sqrt{s} = 7$ TeV’. In: *Nucl. Phys. A* 855 (2011), pp. 281–284.
- [55] G. Agakishiev et al. (HADES collaboration). ‘Inclusive pion and eta production in p+Nb collisions at 3.5 GeV beam energy’. In: *Phys.Rev. C* 88 (2013), p. 024904. DOI: 10.1103/PhysRevC.88.024904. arXiv: 1305.3118v2.
- [56] M. Zyzak et al. ‘The KF Particle Finder package for short-lived particles reconstruction for CBM’. In: *GSI Scientific Report 2012* (2013). URL: <http://repository.gsi.de/record/51983>.
- [57] *FairRoot official homepage*. URL: <https://fairroot.gsi.de/>.
- [58] Rene Bruns and Fons Rademakers. ‘ROOT - An Object Oriented Data Analysis Framework’. In: *Nucl. Inst. & Meth. in Phys. Res. A* 389 (1997), pp. 81–86. URL: <http://root.cern.ch>.
- [59] J. Adamczewski-Musch et al. ‘Event reconstruction in the RICH detector of the CBM experiment at FAIR’. In: *Nucl. Instrum. Methods A* 766 (2014). RICH2013 Proceedings of the Eighth International Workshop on Ring Imaging Cherenkov Detectors, Shonan, Kanagawa, Japan, December 2 – 6, 2013, pp. 250–254. DOI: 10.1016/j.nima.2014.04.082.
- [60] S.A. Bass et al. ‘Microscopic models for ultrarelativistic heavy ion collisions’. In: *Progress in Particle and Nuclear Physics* 41 (1998), pp. 255–369.
- [61] K.A. Olive et al. ‘Review of Particle Physics’. In: *Chin. Phys. C* 38 (2014), p. 090001.
- [62] S. M. Kiselev. ‘Reconstruction of π^0 and η with ECAL’. In: *CBM Progress Report 2009* (2010).
- [63] Jerzy Bartke. *Introduction to Relativistic Heavy Ion Physics*. 2009.

References for chapter 7

- [52] Melanie Klein-Bösing. ‘Development of a Transition Radiation Detector and Reconstruction of Photon Conversions in the CBM Experiment’. PhD thesis. 2009.
- [64] D. Drijard, H.G. Fischer, and T. Nakada. ‘Study of event mixing and its application to the extraction of resonance signals’. In: *Nucl. Instrum. and Methods* 225 (1984), pp. 367–377.
- [65] C. Blume. ‘Produktion neutraler Mesonen in heißer hadronischer Materie’. PhD thesis. 1998.
- [66] Nick van Eijndhoven and Wouter Wetzels. ‘In-event background and signal reconstruction for two-photon invariant-mass analyses’. In: *Nucl. Instrum. Methods A* 482 (2002), pp. 513–519. DOI: 10.1016/S0168-9002(01)01558-3.



Acknowledgement

The creation of this thesis would not been possible without the help and support of many people. My utmost gratitude goes to Prof. Dr. Karl-Heinz Kampert for giving me the possibility to be part of his working group and the CBM-RICH project. I am very appreciative for his supervision and for allowing me to study very interesting aspects, both in practice (with the prototype) as also within simulations (conversion analysis).

A special thanks goes also to Prof. Dr. Claudia Höhne for her help and support during my years in the CBM-RICH group. Her useful hints and questions in multiple meetings and discussions lead to an improvement and a better understanding of my results. Thus, I am very thankful for reviewing this thesis.

I would like to thank Dr. Christian Pauly for his outstanding support during all the years since I came to the Wuppertal group in 2010. His ideas, when I faced new or unexpected results, always allowed me to further enhance my results and my understanding of them. I am also very thankful for his proof-reading of this thesis and the corrections, which he suggested.

My big gratitude goes to my office colleagues Dr. Jan Kopfer, Jörg Förtsch, Ievgenii Kres, and Vivek Patel for all the interesting discussions, whether related or not related to physics or computer problems.

It was always a pleasure to work within the CBM collaboration, and especially in the CBM-RICH group. I'm grateful to everybody in CBM and at GSI/FAIR, whom I worked with, and in particular I would like to thank Dr. Tariq Mahmoud for all the interesting discussions, Dr. Semen Lebedev for his help with the Cbmroot software, Dr. Maksym Zyzak for his explanations of the KFParticle Finder Package, and Prof. Dr. Tetyana Galatyuk for her support with dilepton physics and the conversion method.

Thanks to Prof. Dr. Zoltán Fodor for being part in my PhD committee.

I am also very thankful to all my former and current colleagues from the astroparticle physics group in Wuppertal for the highly enjoyable working atmosphere, which was a pleasure to work

in every day. I am a little bit sad to leave this group now, although I am happy to finish my thesis. A big thanks goes also to Ingrid Schaarwächter for helping me with all administrative issues.

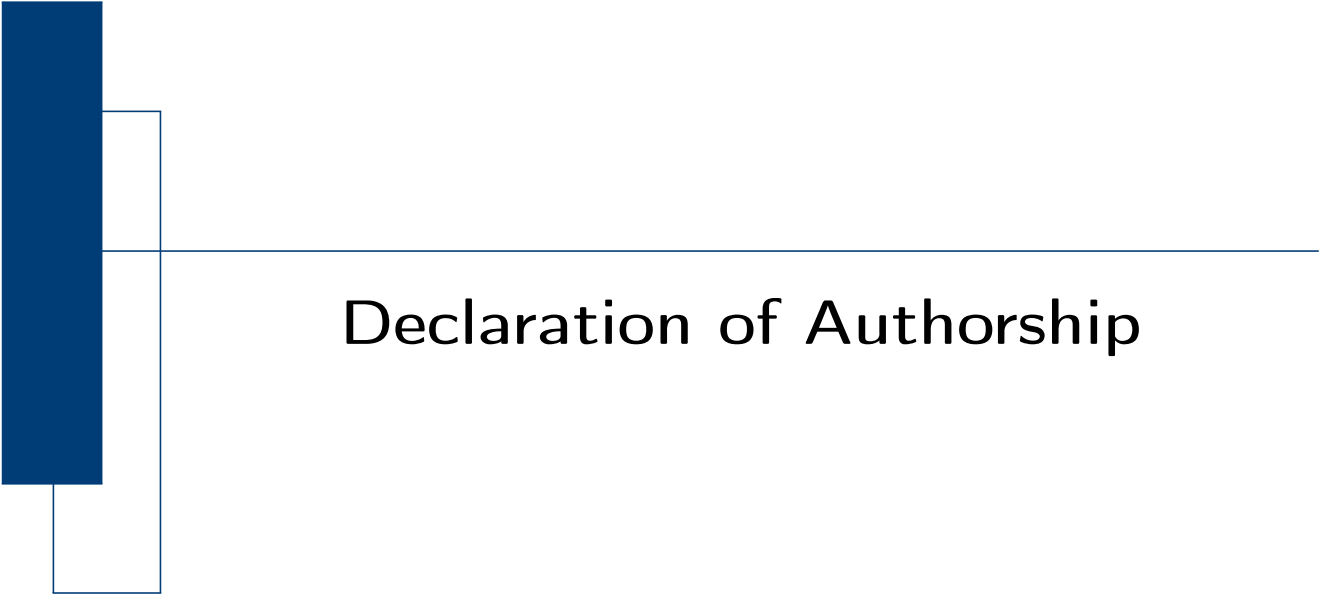
I am very grateful for my fellow students and friends Andreas Behrendt, Sebastian Mathys, Tobias Neumann, and Simon Schlesinger for creating such a fruitful environment during our academic studies and for all those discussions we had (not only) during lunch time.

Finally, I would like to thank all my friends and my family for their continuous support in all the years and their understanding every time, when I couldn't afford enough time to spend with them.

I might have forgotten to mention someone (I hope not), but this doesn't change my deep gratitude to everyone, who helped me during all the years, even when it was just answering one simple question.

Last but not least I'd like to thank my Windows-computers for always being reliable and never crashing, though heavy stress was put on them from my side ;-)

So long, and thanks for all the fish!



Declaration of Authorship

English

I hereby declare that the thesis submitted is my own unaided work. All direct or indirect sources used are acknowledged as references.

This thesis was not previously presented to another examination board and has not been published.

Deutsch

Hiermit versichere ich, die vorliegende Arbeit selbstständig und unter ausschließlicher Verwendung der angegebenen Literatur und Hilfsmittel erstellt zu haben.

Die Arbeit wurde bisher in gleicher oder ähnlicher Form keiner anderen Prüfungsbehörde vorgelegt und auch nicht veröffentlicht.

Wuppertal, den _____

(Sascha Reinecke)